Oxidation of solid carbon materials : Structural and Thermochemical Analysis

Doctoral Thesis in

Industrial Product and Process Engineering

Università degli Studi di Napoli Federico II
XXX Cycle

Cerciello Francesca

Scientific Committee:

Prof. Mauro Causà
Prof. Piero Salatino
Dr. Ing. Osvalda Senneca
Prof. Viktor Scherer

2014-2017

Abstract

This Thesis project aimed at giving a contribution to further unravel selected aspects of the chemistry and physics of carbon combustion and gasification relevant to implementation of novel clean coal technologies for **C**arbon **C**apture and **S**torage (CCS)-ready conversion. Aspects that have been specifically scrutinized are: a) surface oxides as intermediates of carbon combustion and gasification; b) Chemico-physical characterization of chars generated under oxyfiring conditions.

The chemical nature of carbon oxides that populate the char surface and their evolution throughout thermochemical processing has been clarified combining *C1s* and *O1s* core-level XPS Spectra acquired at high-resolution using Synchrotron radiation and thermoanalytical analysis. Results are consistent with the hypothesis represented by a semi-lumped kinetic model based on four steps: formation of 'metastable' surface oxides by oxygen chemisorption, rearrangement of metastable oxides into stable complexes either by thermally activated rearrangement/isomerization or by complex-switch-over driven by molecular oxygen, desorption of surface oxides with release of CO and CO_2. The "metastable" oxides may prevailingly consist of epoxy functionalities, whereas the more stable oxides would be composed by ether and carbonyl moieties. Results are helpful not only in view of applications to stationary combustion or gasification of carbons, but also to shed light on the dynamical patterns of carbon chemisorption/desorption under alternating oxidizing conditions, relevant to "looping combustion" of carbon, as in the "Carboloop" concept proposed by the Naples group.

Along a different path, it is recognized that coal combustion is significantly changed in CO_2-rich atmospleres as oxyfiring. In an international collaboration between three institutions from Aachen, Bochum and Naples, pyrolysis experiments have been carried out to investigate the influence of inert (N_2) vs reactive (CO_2) gas atmospheres as well as reactor type (and associated test conditions) on properties of gas, tar and char. At low heating rates/ temperature or high heating rates /temperature, the differences between N_2 and CO_2 pyrolysis products were marginal. A CO_2 rich atmosphere, instead, impacted severely the properties of pyrolysis products under the fast heating-short residence time conditions in drop tube reactor. In particular, in the course of pyrolysis experiments in drop tube reactor in CO_2, the appearance on the wall of the ceramic filter of a fluffy carbonaceous solid material was noticed. What emerged is that such fine carbon particulate is mostly ash-free, suggesting that its

formation occurs in the gas phase. In order to investigate chemical and structural effects on char reactivity, DTR chars prepared in N_2 and CO_2 were subjected to combustion and oxy-combustion experiments in TGA. The CO_2 chars resulted to be less reactive than the N_2 chars by one order of magnitude in combustion, oxy combustion and gasification TGA experiments. The difference in reactivity between the two chars seems to correlate well with differences in the C-O functionalities which reside on their surface, as detected by XPS. Finally, in order to investigate the effect of substituting N_2 with CO_2 under 'realistic' combustion conditions, combustion and oxy-combustion experiments of coal have been carried out in a drop tube reactor. Chemico-physical analysis suggests an enhanced degree of char burn out and graphitization in CO_2 rich atmospheres. XPS analysis supports the hypothesis that CO_2 could be involved in some cross-linking reactions enhanced by the formation of carboxyl and lacton surface oxide complexes.

.

Outlook of the Thesis

The study gives a contribution to selected aspects of the chemistry and physics of carbon combustion and gasification relevant to implementation of novel clean coal technologies for Carbon Capture and Storage (CCS)-ready conversion. In particular two aspects have been specifically analyzed:

a) deeper understanding of the interaction between solid carbon and oxygen, with a focus on the role, chemical nature and transformations of surface oxides as intermediates of carbon combustion and gasification;
b) characterization of the chemical and physical nature of chars generated upon devolatilization of coal under oxyfiring conditions (i.e. atmospheres with excess oxygen and large CO_2 partial pressures) and its impact on reactivity in heterogeneous gasification reactions.

Chapter 1 provides a literature survey of mechanisms, rates and the role of surface oxides in char oxidation and a survey of CCS-ready coal conversion technologies. The recognition of the role of surface oxides as reaction intermediates in the combustion of coals has been extensively addressed since the early studies on oxidation of solid carbon, but their chemical nature and mechanistic reaction pathways are still open to debate. Studies in this field are helpful not only in view of applications to stationary combustion or gasification of carbons, but also to shed light on the dynamical patterns of carbon chemisorption/desorption under alternating oxidizing conditions, relevant to "looping combustion" of carbon, as in the "Carboloop" concept proposed by the Naples group. In the Carboloop process, looping of the carbon fuel between the oxidizer and the desorber reactor, enables stepwise conversion of carbon over multiple cycles yielding an almost pure stream of CO_2, ready for sequestration, at the exhaust of the desorber reactor. Along a different path, it is recognized that coal combustion is significantly changed in CO_2-rich atmospleres as oxyfiring. In oxy-combustion the amount of O_2 in the oxidizing gas stream is typically raised from 21 to 30 vol% to attain adiabatic flame temperatures similar to those of traditional combustion systems. Moreover, coal particles undergo devolatilization in CO_2 enriched atmospheres. Pyrolysis can be considered as the first chemical step, and, for this reason, has a significant influence on the overall solid fuel thermochemical process.

Chapter 2 provides a description of spectroscopic techniques, including XPS, TGA, XRD, FTIR Raman and Surface area measurement, that have been applied for the chemico-physical characterization of char carbon structure.

To characterize the thermal stability of functional groups which are formed upon oxidation at different temperatures, char samples have been oxidized in thermobalance and analyzed using Temperature Programmed Desorption Technique. The chemical nature of carbon-oxygen functionalities has been clarified by analysis of *C1s* and *O1s* core-level XPS Spectra acquired at high-resolution using Synchrotron radiation. The exact nature of surface oxides formed at low/moderate temperature, their rearrangements and desorption as carbon is heated up, are the very key points of the Carboloop Process, and, for this reason, an experimental campaign of XPS measures has been purposely designed to characterize the nature of surface oxides of char upon alternated cycles of oxidation and desorption. Results are presented and discussed in ***Chapter 3***.

In order to isolate the effects of CO_2 on the pyrolysis stage, in an international collaboration between three institutions from Aachen, Bochum and Naples, pyrolysis experiments have been carried out to investigate the influence of inert (N_2) vs reactive (CO_2) gas atmospheres as well as reactor type (and associated test conditions) on properties of gas, tar and char soot-like from pyrolysis of a high volatile bituminous coal. Pyrolysis products were analyzed by several techniques to highlight differences in structure, reactivity and chemical composition. Moreover, in order to to investigate the fate of coal in atmospheres typical of air and oxy-fuel combustion (*regime II*), when pyrolysis, the early stage of combustion and gasification potentially overlap, chars produced in DTR in oxidizing environments (air (21 vol% O_2/N_2), oxy21 (21 vol% O_2/CO_2) and oxy30 (30 vol% O_2/CO_2)), have been analyzed by several techniques to highlight differences in structure and chemical composition. Results are presented and discussed in ***Chapter 4***. The location of the experimental set ups is specified in section 4.2. ***Chapter 5*** provides the general conclusions of the Doctoral Thesis.

Index

Chapter 1

Introduction and literature survey

1.1 Coal as a material and as a fuel

1.1.1 Survey of basic chemical and physical properties of coal

Coal is an organic, combustible, sedimentary rock, formed anciently from layered plant, consolidated under superimposed strata, and thus not degraded to CO_2 [1]. Coal was formed from lignin, the highly aromatic, complex polymer that constitutes part of the cell walls of plants. The process of coal formation explains also oxygen build-up in the atmosphere [2]. During prolonged periods of time, water and carbon dioxide still trapped in the deposit were released and, under the action of elevated temperature and pressure, the organic matter underwent further polymerization to give a carbon rich solid product, namely coal. Apart from carbon, hydrogen and oxygen, coals may contain other elements, mainly nitrogen and sulphur in variable proportions, as well as inorganics [1,3].

The aromatic carbon content increases in the course of the metamorphic process, so that the final structure of coal can be regarded as a cross-linked macromolecular network of aromatic clusters, plus a portion of relatively smaller molecules [3-4]. The bridges that link the aromatic clusters together are mainly aliphatic in nature. The aliphatic chains, the small molecules, together with moieties containing various heteroatoms, constitute the 'amorphous' fraction of organic matter in coal. The aromatic domains are actually real crystalline particles (crystallites), usually of the order of nanometers in diameter, composed of graphite-like layers arranged turbostratically [5], with an interlayer distance of about 0.35 nm [3]. In spite of the two-dimensional long-range order in the directions of the graphite-like layers, materials with a turbostratic structure are called non-graphitic carbons because there is no measurable crystallographic order in the third direction. This kind of structure is common also to other carbonaceous solid materials such as char-coals and cokes [3-4].

The extent of coalification over geological ages or upon heat treatments modifies the disordered structure of coals towards that of graphite. Indeed, the directed pressure of sedimentary rocks in the course of regional metamorphism determines further supramolecular ordering, that is, a preferred orientation (texture) of crystallites relative to the stacking plane [3]. This in turn determines the physical structure of coals, in terms of porosity, internal and external surface area. Larger pores arise from voids between clusters of ordered polyaromatic domains, while smaller pores account for the space between parallel layers [3,4].

The discrete organic component of coals is called maceral. Macerals possess distinctively specific chemical, physical and performance characteristics, depending on the plant type, climate, ecological conditions, acidity and redox potential of the coal-forming environment [1]. There are three main maceral groups: vitrinite, inertinite, and liptinite. Roughly speaking, vitrinite and inertinite are rich in aromatic structures, while liptinite is mainly aliphatic in nature [1]. Minerals are also present in coals. Broadly, they fall into three main groups: silicates (quartz and clays), sulphides, and carbonates [1]. Organic mineral matter may occur in the form of sulphur, calcium, phosphorus, iron, magnesium, potassium and trace elements. Inorganic mineral matter includes clays (illite, kaolinite and rarely montmorollinite), salts, sulphur and silicates (quartz) [1]. Generally, the ash yield of a coal is taken as indicative of the inorganic component [1].

Depending on the maturation stage reached in the coalification process coals can be classified as peat, lignite, sub-bituminous, bituminous and anthracite. Peat represents the first step in the geological formation of coal and is rich in hydrogen and oxygen. Anthracite represents the highest metamorphic rank in coal. Typically, anthracite contains 5-9% volatile matter (measured as ‘dry mass mineral matter free’(dmmf)), carbon content of 92-98% (dmmf), hydrogen 2.9-3.8% (dmmf), low ash and moisture contents [1]. Commercially and analytically, coal is characterized by its chemical properties (particularly volatile matter contents, ash yield and calorific value), its rank (degree of maturity), type (organic composition as determined petrographically), mineral content and the arrangement of the organic and inorganic components [1]. There is a monotonic relationship between rank and carbon content. Furthermore, coals with a higher content of carbon exhibit higher calorific values [2].

The composite structure of coals greatly determines their consumers’ value and technological and physicochemical properties, but it also imposes some limitations on the investigation and description of coal structures at a molecular level [3].

1.1.2 Thermochemical processing of coal

The story of a single coal particle throughout its lifetime in a combustor is the result of a complex interaction of phenomena, which affect its chemical, morphological and structural properties [6].

When a coal particle is injected in a hot reactor, it heats up and rapidly dries (at temperatures of 300–400 K). Drying is energy intensive and may be accompanied by substantial particle shrinkage [7]. Devolatilization starts at 600-900 K and consists in the (slightly endothermic) removal of hydrogen- and oxygen-rich volatile matter from the solid fuel matrix, and may be accompanied by particle swelling/shrinkage and/or fragmentation [8]. The volatiles evolved from the fuel particle may rapidly ignite and burn homogeneously, if they come in contact with oxygen. Location of volatiles release and combustion is of great importance for the design and operation of combustors/gasifiers [6]. Heating coal particles in the absence of oxygen induces changes in coal structure that resemble those involved in the coalification process. Carbonization of coal occurs in two stages [9]. Firstly, coal is pyrolysed. Depolymerization and changes in carbon hybridization is observed at this stage. Thermal annealing, which represents *stage II* of the carbonization process, leads to stacking and condensation of polyaromatic domains with hydrogen release. During pyrolysis in the absence of oxygen, tar and light gases (volatiles) are driven out of the particles and a solid residue known as char remains. Tar is generally defined as those volatiles, namely small molecular weight fragments, that are released from the coal and condense at room temperature. Light gases comprise mainly oxides (CO_2, CO, H_2O) and small hydrocarbons, made up from one to four carbon atoms. Coal structure evolves, at this stage of carbonization, in the sense of an enlargement of the aromatic domains and a loss of structural defects (edges of the graphenic clusters, in-plane vacancies). Molecular orientational order develops during thermal annealing that modifies the disordered structure of coal towards that of graphite. Actually, the distinction between pyrolysis and thermal annealing, somewhat arbitrary, is more operational than conceptual; it actually refers to a continuous spectrum of transformations involving the raw fuel and its char [9].

Combustion occurs (as a heterogeneous gas solid reaction generally does) in three different regimes controlled by the interchange of transport processes and chemical reaction. External dimensions of the particles, volume, size and distribution of pores within the particles, total internal surface area of the char available for reaction and the intrinsic reactivity are import parameters in the different regimes [10]:

- Regime I: low temperatures/fine particles, oxygen will fully penetrate the porous char so that reactivity increases with total internal surface area [10].
- Regime II: moderate temperatures/coarse particles, reactivity of char will depend on internal burning and the rate of gaseous diffusion through the char walls and within the pores [10].
- Regime III: high temperatures/coarse particles, reactivity may be strongly controlled by diffusion of oxygen through the boundary layer to the particle surface. The rate of diffusion of reactant gas towards a particle is determined by its external dimensions, so reactivity of char may be strongly influenced by particle size [10].

1.1.3 Char oxidation: mechanisms, rates and the role of surface oxides

The carbon-oxygen reaction has been described as "*arguably the most important reaction known*" [11], and indeed it plays an important role in key industrial technologies that include the combustion and gasification of coal, but also of biomass, and solid waste. Computer models are frequently used in the design and retrofit of these processes. Development of simple combustion models is made difficult by the complexity of the carbon-oxygen reaction mechanism, in fact kinetics are known to be influenced by transient buildup of surface oxides [12].

Oxygen binds preferentially to defective sites in the carbonaceous organic matter, such as in-plane vacancy defects, edges of the aromatic domains, aliphatic residues. Edge carbon atoms and inorganic catalytic sites should lie preferentially on the surface of meso- and macropores, which, should be more reactive than micropores [13]. In fact, char gasification has been reported to increase char mesoporosity at the expense of micropores during char conversion [13].

In an attempt to rationalize the vast body of data on oxidation of carbon materials Du et al. [14] assumed the existence of two types of sites: *type A* sites are very reactive in terms of oxygen adsorption and are rapidly saturated in the early stages of reaction; *type B* sites are instead involved in the subsequent steps of reaction. The concept of a two-site mechanism was expanded by assuming that there exist populations of active sites characterized by continuous distributions of chemisorption activation energies. Moreover, according to Du et al., oxygenated intermediates are formed at a carbon surface by adsorption of O_2, which are not directly involved in the desorption process [14].

The idea of the formation of unstable (intermediate) carbon-oxygen functional groups in the first stage of oxidation of coal has been also suggested by Wang et al. [15], who examined the mechanism of the oxidation of a bituminous coal at low temperatures (below 100 °C) by employing gas

chromatography to monitor the rates of production of CO_2 and CO during desorption and oxidation experiments. They assumed, based on previous experimental evidences [16-17], these unstable intermediates to be peroxygen, hydroperoxide and hydroxyl species. Moreover, they observed a progressive decrease in the rates of formation of carbon oxides in the early stages of oxidation, which was ascribed to 'unreactive' oxygenated complexes being formed during oxidation and permanently deactivating the reaction sites for further oxygen adsorption at low temperatures. As a result, they found that a period of oxidation eventually results in a reduction in the concentration of those species responsible for the production of CO/CO_2. They identified this stable 'unreactive' species as being mostly anhydrides, ethers, and esters [15]. Indeed, many experimental studies, most of which are based on FTIR, TPD, and XPS experiments [18-21], point out that formation of stable carbonyl-containing species and ethers takes place on the surface of solid carbons for prolonged exposure to oxygen at moderate temperatures. The deactivation of reaction sites responsible for the oxygen adsorption as a consequence of the accumulation of stable oxygenated functionalities has been also postulated by Salatino et al. [13].

The recognition of the role of surface oxides as reaction intermediates in the combustion of coals has been extensively addressed since the early studies on oxidation of solid carbon, but their chemical nature and mechanistic pathways are still open to debate [15, 22-23].

Various reaction mechanisms have been proposed to explain the characteristics of consumption of O_2, and formation of oxidation products in the gas and solid phases [22]. Kinetic models (i.e. *Global power-law, Langmuir–Hinshelwood, Three-step semi-global, Enhanced three-step*) have also been developed to describe the rate of oxygen consumption and the rates of formation of gaseous oxidation products in terms of the rate parameters of the relevant reactions, oxidation time, temperature, and initial concentration of oxygen in the oxidising medium [12,22,24].

Haynes and co-workers further expanded the consideration of the multiplicity of sites and proposed a semi-lumped reaction network (eq.1.1) embodying two types of sites [24,25]:

$$C_f^* + O_2 \xrightarrow{1} C(O)^{\#}$$

$$C(O)^{\#} + O_2 \xrightarrow{2} C(O) + CO, CO_2$$

$$C(O)^{\#} \xrightarrow{3} C(O) + CO, CO_2$$

$$C(O) \xrightarrow{4} C_f^* + CO, CO_2 \qquad (1.1)$$

According to mechanism (eq.1.1), chemisorption on an active carbon site (C_f^*) results in non-dissociative chemisorption of oxygen, with formation of a "metastable" ($C(O)^{\#}$) surface oxide (*reaction 1*). The metastable oxide may further undergo complex switch-over in the presence of oxygen, as a consequence of the increasing degree of surface carbon oxidation, according to *reaction 2*. Alternatively, metastable oxides can be rearranged or isomerized into more energetically favourable forms according to *reaction 3*. At higher temperatures, the stable oxides can desorb, mainly as CO and CO_2, in a strongly endothermic step (*reaction 4*) [24-25].

In ***Chapter 3*** of the Doctoral Thesis, the thermochemistry and the reaction mechanisms of char oxidation and desorption have been investigated in more detailed, with a special interest to the novel clean coal technology of Carboloop Process, described in section *1.2.2.2*

1.1.4 Early oxidation and the formation of metastable oxides

Considerable progress towards a better understanding of the fundamental mechanisms of carbon-oxygen interaction has been recently provided by the theoretical work of material scientists, which used modern ab initio methods of quantum chemistry to model oxygen chemisorption and desorption on aromatic clusters and graphene [26-29]. This research field has been deeply studied in order to investigate the gradual increase of the electronic mobility resulting from the progressive elimination of oxygen from graphene oxide [27].

However, virtually all studies in the literature, which used a variety of reduction techniques, report the presence of residual oxygen in reduced graphene oxide (rGO) despite aggressive chemical and thermal treatments [26-29].

Hence, the mechanisms of char combustion and of graphene oxidation hypothesized in different contests and with different perspectives, share very similar concepts and can to a good extent be reconciled in a comprehensive description of oxidation of different solid carbons.

Recently, Larciprete et al. [27,28], investigating oxidation of the highly oriented pyrolytic graphite (HOPG) by means of XPS experiments and DFT modelling, have further strengthened the kinetic mechanism proposed in eq.1.1. They found that oxygen atoms bind to the basal plane of graphite in bridge position over the C−C bonds, forming epoxy groups. At high oxidation levels lattice damage was proven by the appearance of C=O bonds which accompanies the enhancement of the ether concentration. Calculations showed that in the three-member epoxy ring the length of the C−C bond located below the O atom increases from 1.42 to 1.51−1.58 Å which is close to the sp^3 bond length in diamond [28]. It was found that the interaction between epoxy groups is attractive up to a coverage of 50%, and epoxy clustering is energetically favoured with respect to a random surface distribution [27]. Moreover, due to the cumulative cleaving force exercised on the underlying C−C bonds, the aligned epoxy groups tend to unzip into ethers being definitely incorporated into the C basal plane. Unzipping of aligned epoxy groups has been proposed as responsible for initiating the fault lines observed in GO [27,28].

Radovic [26] performed DFT calculations at the B3LYP/6-31G level of theory on model polyaromatics with carbene-type zigzag carbon atoms and carbyne-type armchair pairs. The results showed that O_2 chemisorbs dissociatively at the edges of the aromatic planes forming epoxy groups.

Plausible evolution pathways for the evolution of the epoxy functionalities towards more stable species are analogous to the well-known O-insertion mechanism of oxepin/benzene oxide tautomerism. Below, in Fig.1.1, taken by [26], are reported two of the aromatic structures optimized by Radovic [26] that could be involved in a possible route to desorption of CO_2:

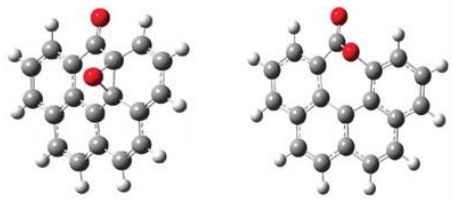

Fig.1.1. Optimized geometries of carbon clusters involved in an indirect path to CO_2 formation. Unzipping of the epoxy oxygen in the plane of the molecule is likely to occur through an insertion mechanism similar to the formation of oxepin from benzene oxide. Fig. taken by [26].

The process of formation of an epoxide-type oxygen at the edges and on the basal plane of polycyclic aromatic hydrocarbons (PAHs) is still an unsolved issue, but circumstantial evidence for its presence is compelling [26].

Sànchez and Mondragòn [30] showed possible route for the epoxy group formation. A schematic representation is presented in Fig.1.2, taken by [30]. In the hypothetic case studied by [30], there is an isolated active site which is susceptible to follow further oxidation:

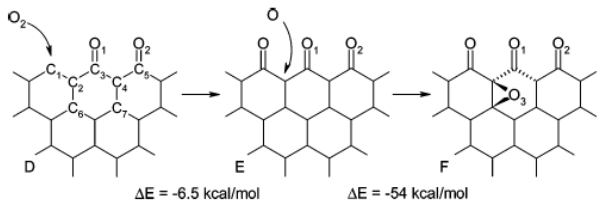

Fig.1.2. Possible route for an epoxy group formation by atomic oxygen on oxidized graphene layer. Fig. taken by [30].

In this case proposed by Sànchez and Mondragòn [30], the O_2 molecule approached the graphene edge in a perpendicular manner to form the peroxy radical which later dissociated to form a carbonyl group and an oxygen radical. This reaction has been shown to have an exothermicity of -6.5 kcal/ mol [30]. Due to its high reactivity, the radical oxygen atom may readily react with the carbon atoms in the basal plane near the edge of the graphene layer forming an epoxy complex as has been suggested by different authors [30,35].

Sànchez and Mondragòn showed that the formation of the epoxy group deforms the planarity of the graphene layer due to the transformation of the carbon hybridization from sp^2 to sp^3 which, at the same time, disrupts the aromaticity of the graphene layer. In spite of the change in the geometry, they found that the new reaction is thermodynamically favorable as can be seen from the calculated exothermicity of the reaction (-54 kcal/mol, Fig.1.2) [30].

1.1.5 Structural evolution of surface oxides

Larciprete et al. [27,28] shown that the epoxy groups are the functionalities with the lowest thermal stability and are dominant group at the low oxidation stage, while long graphene exposures to atomic O increase the probability for the adsorption of oxygen atom as first neighbors of other epoxy groups already residing on graphene, thus forming stable ether-epoxy pairs. In their study, these ether-epoxy pairs are shown to attract the diffusing epoxides (Fig.1.3A taken by [27]) and can convert via a two-step reaction mechanism into the lactone-ether pairs, which are more than 3 eV lower in energy than the initial surface structure (epoxy-ether and a diffusing epoxy) [27].

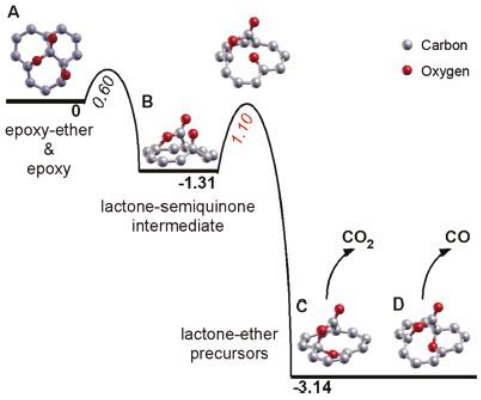

Fig.1.3. Formation of surface precursors for GO decomposition. Calculated minimum energy path for the formation of the lactone-ether surface precursors from the epoxy-ether pairs assisted by a diffusing neighbouring epoxide. Fig. taken by [27].

They suggested that, once the consumption of the graphene lattice has started, diffusing epoxy groups can bind at vacancies forming additional ethers. The relative position of the ether with respect to the lactone in the lactone-ether pairs (Fig.1.3 C-D taken by [27]) determines the CO or CO_2 products [27]. Moreover, the thermal decomposition of the lactone- ether pairs leaves C vacancies saturated by ether groups. Both processes, which were used to explain the slightly increasing ether fraction observed during annealing, favor the formation of additional ether-epoxy pairs [27].

Based on their simulations, Larciprete et al. [27,28] concluded that the thermal reduction of graphene oxidized by a low density of epoxy groups proceeds by releasing solely molecular oxygen via a cycloaddition reaction from epoxy-epoxy pairs. The formation of ether-epoxy pairs at high O coverage promotes the elimination of CO/CO_2 mixtures, thus determining surface defects and C loss. They found that the competing surface reactions, leading to O_2 and CO/CO_2 evolution, are always assisted by epoxide diffusion and have comparable energy barriers [27].

Bagri et al. [29] performed MD simulations on GO sheets with variable oxygen increasing the ratio of hydroxyl to epoxy functional groups in the basal plane (1/1, 3/2 and 2/3). They took into account the experimental observation of Cai et al. [36], who found that a hydroxyl group bonded to a carbon atom was accompanied by an epoxy group bonded to a neighbouring carbon atom. Results revealed that reduction by thermal treatment leads to the formation of carbonyl and ether groups. Calculations confirmed that both groups are stable thermodynamically and cannot be removed without destroying the parent graphene sheet (with evolution of CO and CO_2) [29].

Calculations showed that on the structures of the sheets, after annealing at 1500 K, significant atomic rearrangement took place. Specifically, carbonyls, ether rings (such as furans, pyrans and pyrones), quinones, and phenols, along with increased sheet roughness, were found [29].

Analysis of their MD simulations revealed that the hydroxyl functional groups require lower temperatures for desorption than the epoxy groups, as indicated by the release of H_2O below 1000 K. Above this temperature, evolution of a small amount of CO, CO_2 and O_2 was observed. O_2 evolution was attributed to desorption of some isolated epoxy groups and the release of CO/CO_2 was observed when hydroxyl and epoxy sites are in close proximity. The desorption of epoxy groups in close proximity to other saturated sp^3 carbon bonds leads to the creation of vacancies within the basal plane as a result of the evolution of CO_2 and CO molecules above 1500 K [29].

Bagri et al. [29] showed that the formation mechanisms of groups such as carbonyls and ether rings have different origins [29]. Overall, carbonyls are created by rearrangement of epoxy groups and hydroxyls closely surrounded, but the formation of substitutional oxygen (C–O–C ether rings) is favoured at high temperatures [29]. Their simulations showed that the carbonyls' concentration progressively increases whereas epoxy concentration decreases after annealing. The effect was most prominent for GO with a higher hydroxyl/epoxy ratio [29]. The formation of carbonyls was linked to the interplay between hydroxyl and epoxy groups or to two epoxy groups bonded with two

neighbouring carbon atoms and facing the opposite side of the sheet. The generation of carbonyls was favoured thermodynamically, as shown by the reduction in the total energy of the system on formation of these functional groups [29].

Bagri et al. [29] concluded that simulations clearly reveal the formation of carbonyl and ether groups through transformation of the initial hydroxyl and epoxy groups during thermal annealing.

Also, an increase in the annealing temperature did not lead to an enhancement in the rate of oxygen release. On the contrary, at high annealing temperatures the probability of oxygen incorporation, as stable carbonyl groups and ether rings, was found to be higher [29].

MD simulations clearly pointed to the highly strained epoxy groups as the primary cause for the evolution of CO and CO_2. [29].

1.1.6 Decomposition of surface oxides and product desorption

In order to get an insight into the reactions that produce CO or CO_2, it is important to investigate the chemical nature of the complexes formed in the initial steps and their transformation during the process [30]. Recently, to determine the nature of carbon surface complexes several experimental studies have been carried out employing techniques such as IR, NMR, X-ray photoelectron spectroscopy (XPS), scanning electron microscopy, transmission electron microscopy, temperature programmed desorption (TPD), and transient kinetics (TK), among others [30,37-50]. One of the most common techniques in complexes characterization still remains TPD since it allows to characterize the thermal stability of functional groups through their decomposition products. For example, the carboxilate groups generally decompose as CO_2, while ether, phenol, or carbonyl functionalities decompose as CO [29].

Marchon et al. [51] used TPD to calculate desorption activation energies of CO and CO_2 and compared the determined values with those reported for bond energies of lactones, carbonyls, and semiquinones on reference compounds. A good correlation was obtained suggesting the presence of these functionalities on the carbonaceous materials during combustion or gasification processes [51].

TPD may be used simultaneously with other techniques to obtain more detailed information of the functional groups giving rise to the CO or CO_2 thus formed [30]. Kelemen and Freund [44] employed TPD and XPS to evaluate the decrease of the XPS signal of different complexes correlating them with the desorbed gases. This procedure allowed the researchers to observe that during CO_2 desorption the 288.8 eV *C1s* XPS signal diminishes. This signal corresponded to carbon atoms

bonded to oxygen atoms by means of three bonds, suggesting the presence of carboxilate or carbonate groups [44]. Haydar et al. [46] suggested the presence of carboxylic acids, anhydrides, and lactones for the first steps of CO_2 desorption. CO desorption was associated with aldehydes or ketones decomposition.

In 1988, Hall et al. [37], performing linear TPD on various oxidized coal char samples at variable heating rates from 20 to 300 K/min, noted that the total integrated amount of CO_2 evolved is a function of the heating rate and exhibits a broad maximum in the vicinity of about 100 K/min.
This behavior was attributed, by Hall and Calo [37], to secondary reaction via (eq.1.2):

$$CO_{(g)} + C(O) \leftrightarrow C_f + CO_{2(g)} \quad (1.2)$$

where *CO* represents "free" carbon monoxide resulting from the desorption of a surface oxygen complex, *C(O)* is a surface oxygen complex, and C_f is an unoccupied surface-active site. In view of the high carrier gas flow rates used in their work, they suggested that it was quite certain that these reactions do not involve external bulk gas-phase species, but rather they must occur within the char pore structure (most probably in micropores) between desorbed oxides of carbon during transport out to the bulk phase and on both occupied and unoccupied active surface sites [37]. Menster and Ergun [52] determined $\mathbf{\Delta G^\circ}$ = -71 kJ/mol for eq.1.2 as written; i.e., it is exoergic and, therefore, favoured at lower temperatures [37,52].

It is well established that desorption of surface oxides yields mostly CO_2 at low-to-moderate temperature, whereas the CO/CO_2 ratio increases with the desorption temperature, according to the Boudouard reaction, eq.1.3:

$$2CO_{(g)} \leftrightarrow C_f + CO_{2(g)} \quad (1.3)$$

On the other hand, eq.1.2 gives rise to a consistent $CO\text{-}CO_2$ shift, more efficiently than the homogeneous CO disproportionation [53]. Obviously, this phenomenon complicates the interpretation of TPD spectra and indicates that considerable care must be taken to ensure that resultant energetics are truly reflective of the original state of oxygen complexes on carbon surfaces [37].
Recently, these phenomena have been studied by Montoya at al. [54], who investigated the effect of neighbouring surface oxygen groups *C(O)* on the desorption of the CO molecule from the carbonyl

model using DTF Theory. They found that the presence of the neighbouring surface oxygen group decreases the CO desorption energy. In particular, the neighbouring carbonyl group decreases the desorption energy by 46%, while the semiquinone group decreases by 19.3%. The largest effect was seen from the epoxy oxygen group: it decreases the CO desorption energy by 80.0%. It has been shown that the presence of an epoxy group near an oxidized carbon surface complex debilitates the edge adjacent to the epoxy group facilitating the gasification of the graphene layers in the form of CO [54]. The same research group investigated [55] the adsorption of CO on unsaturated edges of carbonaceous materials, to characterize surface oxygen complexes, and to elucidate pathways for CO_2 desorption [55]. They found two different possible and energetically feasible CO_2 desorption pathways after CO adsorption reported in Fig.1.4, taken by [55].

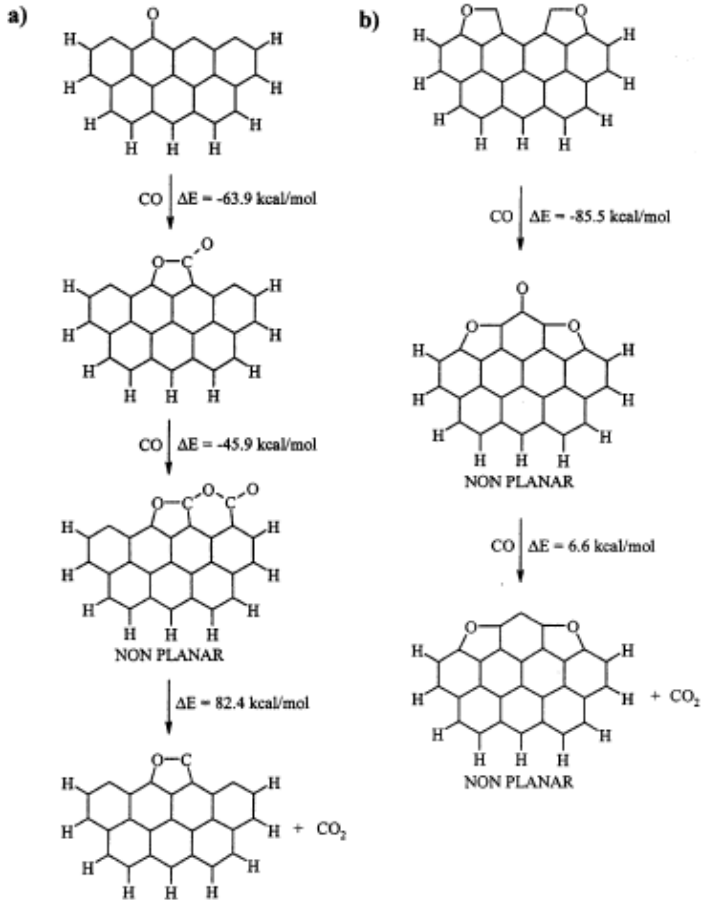

Fig.1.4. CO consecutive adsorption that favour (a) CO_2 desorption and (b) six-member rings formation. Fig. taken by [55].

The resulted complex was nonplanar due to the presence of a five-member ring next to a six-member ring [55]. The interaction energies calculated for this process is -63.9 kcal/ mol for the first CO adsorption and -45.9 kcal/mol for the second one. This yields the total interaction energy of -109.8 kcal/mol. The CO_2 desorption energy from this structure is 82.4 kcal/mol. Thus, their calculation showed that desorption of CO_2 after consecutive adsorption of CO is an exothermic process with the overall reaction energy of -27.4 kcal/mol. CO adsorption on a two nearby cyclic ether groups was found as another CO_2 desorption pathway as shown in Fig.1.4b, taken by [55]. Adsorption of the first CO formed an additional semiquinone group with the interaction energy of -85.5 kcal/mol. Adsorption of the second CO and subsequently desorbing CO_2 required only 6.6 kcal/mol. [55].

Hall and Calo [37], concluded that secondary interactions can significantly affect TPD spectra of oxidized carbonaceous solids and that such spectra may not necessarily be reflective of the true original state of surface oxygen complexes. They suggested that thermally stable *C(O)* complexes did not participate in secondary reactions at temperatures significantly below their desorption temperature. This means that, at the temperatures required to activate (i.e., thermally decompose) the surface complexes, the forward step of eq.1.2 (ie., CO_2 formation) is favoured [37].

At high temperature, the reverse Boudouard reaction takes place, favouring the high CO/CO_2 ratio. According to Hall and Calo [37], the degree to which secondary interactions affects resultant TPD spectra is a complex function of the carbon pore structure, extent of surface coverage, and the integrated time-temperature history of the various species involved and, possibly, even the levels and types of impurities [37]. For instance, if a CO molecule is released in a narrow pore of char from any surface complex, it is possible that the CO molecule can interact with surface oxygen complexes favouring the CO_2 desorption [55].

1.2 Coal exploitation and the climate challenge

1.2.1 Survey of Carbon Capture and Storage (CCS)-ready coal conversion technologies

Rising concerns about climate change have become prime drivers of scientific and technological development in the field of solid fuel combustion and gasification [56,57,58]. Studies in this field are targeted either to the reduction of carbon dioxide emissions per unit energy generated or to the development of novel combustion concepts that make CO_2 capture and sequestration inherently more economical and feasible. The first goal is mainly pursued through the improvement of power plant efficiency [56]. The second goal is pursued by rethinking combustion technologies in such a way that carbon dioxide is highly concentrated at the exhaust, possibly free of contaminants, so that it can be more easily compressed and disposed of through the sequestration path [57].

Technologies proposed for reducing CO_2 emission from coal-fired power generation, can be divided in [74]:

- Pre-combustion capture: fuel is either gasified or reformed to syngas, a mixture of carbon monoxide and hydrogen, which is then shifted via steam reforming. CO_2 is separated from the syngas by shifting carbon monoxide with steam, yielding pure hydrogen (water gas shift reaction). An example of pre-combustion capture system is the Integrated Gasification Combined Cycles (IGCC) [74].
- Post-combustion capture: CO_2 is separated from the flue gases using chemical solvents [59], sorbents (such as calcium oxide [60] or carbon fibres [61]) and membranes [62] without changing the combustion process [74].
- Oxy-fuel combustion: instead of using air as oxidizer, pure oxygen (O_2) or a mixture of O_2 and recycled flue gas is used to generate high CO_2 concentration product gas; therefore, the combustion process is significantly changed [74].
- Chemical-Looping Combustion (CLC): is another combustion in which pure oxygen rather than air is supplied by metal oxides for combustion, such that the mixing between CO_2 and N_2 is inherently avoided [74].

Two CCS-ready coal conversion technologies have been specifically considered in the context of the present study. Chemical-Looping-Combustion has been examined with a specific focus on the "Carboloop" concept, a looping combustion process based on the idea that carbon may act as fuel and

oxygen carrier at the same time. Oxy-fuel combustion has also been considered, with a specific focus on the role of oxyfiring environment on the nature and reactivity of chars generated upon coal devolatilization.

1.2.2 Chemical looping combustion and gasification of coal

Chemical looping combustion (CLC) of gaseous fuels (light hydrocarbons, syngas from gasification of coal and heavy residues) has been demonstrated at the laboratory scale, and is approaching pilot-scale demonstration [63-66]. Chemical looping combustion is based on the combined operation of two interconnected reactors: a fuel reactor and an air reactor [53,63-66]. A solid oxygen carrier (most typically a metal oxide) is transferred in the fluidized state from the fuel reactor to the air reactor and vice versa. Fuel oxidation is accomplished in the fuel reactor by the solid carrier, M_yO_x, which enters the reactor in the oxidized form and is reduced therein [53,63-66]:

$$C_nH_{2n}+(2n+m)M_yO_x \rightarrow nCO_2+mH_2O+(2n+m)M_yO_{x-1} \quad (1.4)$$

The reduced form of the carrier, M_yO_{x-1}, is transferred to the air reactor where it is subject to oxidation by contact with air:

$$(2n+m)M_yO_{x-1}+(n+\frac{m}{2})O_2 \rightarrow (2n+m)M_yO_x \quad (1.5)$$

Proper recirculation of the carrier can be established between the two reactors and gas leakage from each reactor to the other can be prevented [67]. This operation makes possible to produce a stream of nearly pure carbon dioxide issuing from the fuel reactor, completely separated from the air stream leaving the air reactor [63].

CLC based on the use of oxygen carriers is inherently suitable for gaseous fuels. Effective contact between the solid carrier and the fuel can be easily achieved in this case. Application of the same process to solid fuels is more problematic [53]. Direct fuel oxidation by the oxygen carrier implies an inherently inefficient reaction between two solid phases:

$$C_{(s)}+2M_yO_{x(s)} \rightarrow CO_{2(g)}+2M_yO_{x-1(s)} \quad (1.6)$$

To overcome this limitation and to extend the CLC concept to capture-ready combustion of solid fuels, recent efforts have been based on the idea that solid fuels can be in situ or ex situ gasified in the fuel reactor by steam or carbon dioxide, yielding a syngas that eventually acts as the reducing agent of the oxygen carrier [68-71].

1.2.2.2 The "Carboloop" process

A new concept of chemical looping combustion of solid carbons has been developed by Salatino and Senneca [53,72], and patented under the name of Carboloop [72].

In the Carboloop process the carbon itself acts as the oxygen carrier between two reactors: an oxidizer, where carbon is oxidized by air at a temperature and for holding times that prevent the parallel course of carbon gasification, and a desorber, where rapid desorption of oxidation products, mainly as CO_2 and CO, takes place in an oxygen-free atmosphere at higher temperatures [53,72]. Looping of the carbon fuel between the two reactors, corresponding to temperature cycling between the oxidizer and the desorber, enables stepwise conversion of carbon over multiple cycles yielding an almost pure stream of CO_2, ready for sequestration, at the exhaust of the desorber [53]. Fig.1.5, taken by [53], depicts the operational scheme on which Carboloop is based.

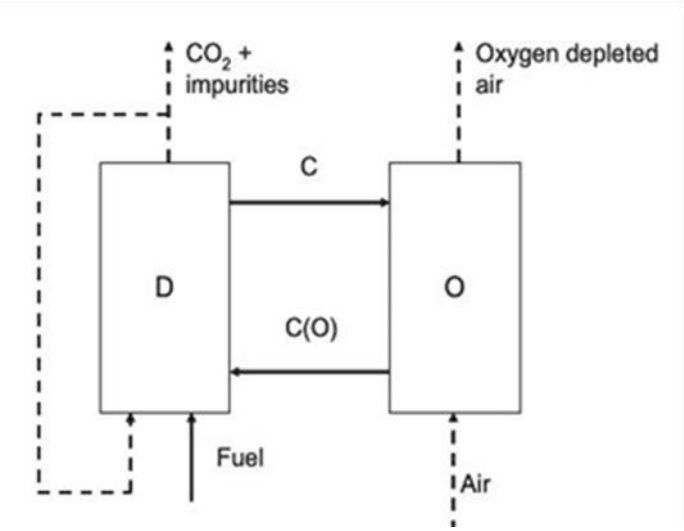

Fig.1.5. Outline of the Carboloop process based on a dual interconnected fluidized bed reactor. O is the oxidizer where oxidation by air of the solid fuel (C) takes place. D is the Desorber where inert conditions and higher temperature favour the desorption of carbon oxides from the surface of the pre-oxidized fuel (C(O)). Dashed lines indicate gas streams, while solid lines show the transfer of the solid carbon between the two interconnected reactors. The desorber can be operated with partial recycle of gaseous effluents (CO_2 + impurities). Fig. taken by [53].

The Carboloop concept exploits the differences in the reaction rates of the individual steps in the semi-lumped reaction mechanism proposed by Haynes (section 1.1.3 eq.1.1[24-25]) as a function of temperature [53]

The simplified approach is represented by:

$$C_f^* + O_2 \xrightarrow{1} C(O)^{\#}$$

$$C(O) + O_2 \xrightarrow{2} CO, CO_2 + C(O)$$

$$C(O) \xrightarrow{3} CO + C_f \qquad (1.7)$$

No distinction is made, in this semi-lumped model, as regards the nature of the active sites and the stability of the oxygen complexes, nor is the co-existence of carbon sites of different activity and of surface oxides of different stability considered [53].

Fig.1.6, taken by [72], reports the values of R_i, i.e., the rates of individual steps i =1, 2, 3, calculated by Senneca and Salatino [72]:

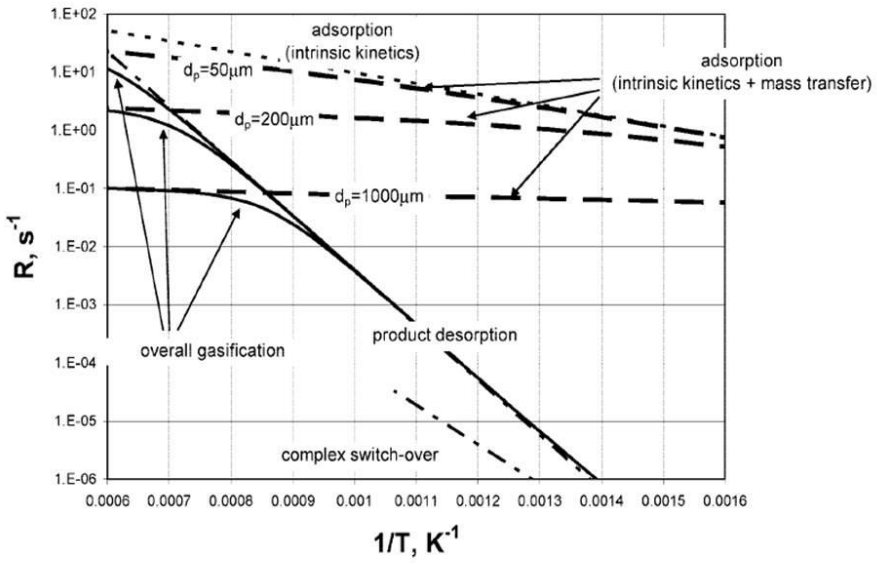

Fig.1.6. Mechanistic basis of the Carboloop concept. Fig. taken by [72].

Computations have been based on an oxygen partial pressure of 0.1 bar and on a value of 1×10^7 s^{-1} bar^{-1} of the pre-exponential factor of the kinetic constant k_3. The other kinetic parameters were taken after Hurt and Calo [12]. Fig.1.6 reports also the rates of oxygen chemisorption and the overall combustion rates computed by considering the effect of intraparticle and external diffusional restrictions [72].

Salatino and Senneca suggested [72] that the rate of complex switchover (*step 2*) plays a minor role in the range of temperatures 500-700 K. Product desorption (*step 3*) dominates the rate of carbon gasification in the intermediate range. At high combustion temperatures, oxygen chemisorption overtakes product desorption as the rate-controlling step. Chemisorption rates and overall combustion rates are both affected by diffusional limitations to an extent that depends on particle size. Moreover, the difference between the rates of *step 1* and *3* makes possible to perform looping combustion of carbon through cyclic steps of carbon oxidation [72].

Desorption of surface oxides yields mostly CO_2 at low-to-moderate temperature, whereas the CO/CO_2 ratio as primary desorption products increases as the desorption temperature is increased [72]. On the other hand, secondary reaction between CO and surface oxides [37], and the reverse Boudouard reaction, whose turning temperature is =960 K, give rise to a consistent $CO\text{-}CO_2$ shift. A desorption stage ending at or below 960 K temperature, possibly associated with countercurrent flow pattern between the solids and the gas, was suggested to complete CO oxidation over freshly oxidized carbon particles and ensure large CO_2 yields [53,72].

The feasibility of the Carboloop concept was verified by Salatino and Senneca [53] by means of purposely designed experiments carried out with a thermogravimetric analyzer. Looping of the carbon fuel between the oxidizer and the desorber were simulated in discontinuous experiments in TGA, in which a batch of carbon was periodically subjected to temperature or oxygen concentration cycling [53]. The results of the thermogravimetric experiments were used to assess the operating conditions of the oxidizer and of the desorber. Carboloop combustion was carried out by periodically exposing char to air (O-phase) and nitrogen (D-phase) atmospheres. Oxidation temperature varied between 570 and 770 K, while desorption temperature between 870 and 970 K. Each subcycle lasted between 15 and 60 min. It was found, experimentally, that at moderate oxidation temperatures (570-770 K) oxygen chemisorption (*step 1*) progresses at an appreciable rate, whilst the switch-over reaction and surface oxides desorption are modest, being kinetically limited. These results suggested that at these temperatures it is possible to uptake oxygen on carbon surface, with negligible release of $CO_{(g)}$ and

$CO_{2(g)}$ [53,72]. At higher temperatures, in the order of 970 K, in the absence of oxygen reactions 1 and 2 are suppressed and carbon oxides can be released as $CO_{2(g)}$ and, to a much lesser extent, as $CO_{(g)}$, according to *step 3*. The authors [53,72] suggested that a carbon loading of ≈ 500 Kg would be required per 1 MW_{th} of thermal throughput of the looping combustor. This figure is comparable with typical loadings of oxygen carrier used in typical metal oxide-based chemical looping combustion [72].

1.2.3 Coal oxyfiring

Oxy-fuel combustion has generated significant interest since it was proposed as a CCS-ready technology for newly built and retrofitted coal-fired power plants [73].

In oxy-fuel combustion nitrogen is removed from the oxidant, and recycled flue gases are used to replace it and control the combustion temperature. High CO_2 concentration stream is generated at the end of the combustion process [58]. The idea of applying oxyfuel processes with flue gas recirculation in coal-fired plants to control the CO_2 emission [74] and/or produce high concentration CO_2 for enhanced oil recovery (EOR) was first proposed in 1982 [74-76].

The main purpose of oxy-fuel combustion applications in coal-fired plants is the recovery of concentrated carbon dioxide in an air-like combustion environment [58]. Following these proposals, Argonne National Laboratory (ANL) pioneered the investigation of this process in the mid and late 1980s, focusing on the system and its combustion characteristics [77-79]. Oxy-fuel combustion consists of three main components: the air separation unit (ASU) that provides oxygen for combustion, the furnace and heat exchangers where combustion and heat exchange take place, and the CO_2 capture and compression unit. Due to the large quantity of high-purity oxygen required, cryogenic air separation is currently used for oxygen production in oxy-fuel combustion. A large portion of the flue gas must be recycled back to the furnace for combustion temperature moderation and gas volume reconstitution to ensure proper heat transfer [58].

A basic process flow diagram of the oxy combustion technology can be seen in Fig.1.7, taken by [73].

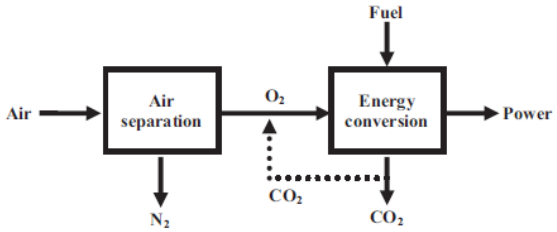

Fig.1.7. Simplified block diagram of an oxy fuel combustion system. Fig. taken by [73].

One of the most noticeable advantages of oxy-fuel combustion is the low NO_x emission, thanks both to the use of oxygen for combustion which eliminates nitrogen from air and to the NO_x re burning mechanism with flue gas recycling. More interestingly, recent research has shown that integrated emissions control of SO_x, NO_x, and mercury (Hg) may be possible as part of the oxy-fuel flue gas CO_2 capture process [58,73]. This alone could significantly reduce the cost of oxy-fuel combustion technology.

Pilot-scale oxy-fuel demonstrations have so far confirmed that plant operations can be effectively switched from air-firing to oxy-fuel firing, air infiltration can be effectively limited, a highly enriched CO_2 flue gas can be produced for transportation and storage [73].
There are four major oxy-combustion demonstration plants in operation [73]:
1. *Lacq, France* (operation started in 2009): a retrofit demonstration to a 30 MW natural gas plant developed by Total. Transported captured CO_2 over 30 km of pipe for storage in a depleted oil reservoir. First integrated and industrial natural gas fired oxy-combustion plant [73].
2. *Alstom Power Plant Laboratory*: a retrofit demonstration to a 15 MW lignite and bituminous coal plant. Major finding was that the NO_x emissions created during oxy-combustion were 50% lower than with standard air combustion [73].
3. *Callide Oxy Fuel Project* (operation started in 2011): first full chain retrofit demonstration performed on a coal fired power plant [73].
4. *Endesa/CIUDEN CFB* (operation started in 2011): largest pilot scale demonstration of the oxy-combustion technology on a coal fired boiler (320 MW) [73].
Pilot-scale as well as computational studies have clearly shown that substituting nitrogen with carbon dioxide as diluent is not trivial. Oxycombustion differs from air combustion in several ways,

including reduced flame temperature and delayed flame ignition [80-81]. These effects have been attributed to differences in heat transfer properties between CO_2, N_2 (density, heat capacity, thermal conductivity and emissivity, lower O_2 diffusivity of CO_2 compared to N_2). In fact, in oxy-combustion the amount of O_2 in the oxidizing gas stream is typically raised from 21 to 30 vol% to attain adiabatic flame temperatures similar to those of traditional combustion systems [58]. Moreover, in oxy-combustion, coal particles undergo devolatilization in CO_2 enriched atmospheres. The composition of the gaseous atmosphere under which pyrolysis takes place have important effects also on the formation and properties of pyrolysis products [82].

In ***Chapter 4***, the influence of CO_2 enriched atmospheres on pyrolysis and oxy-combustion of a high volatile bituminous coal has been scrutinized. The experimental campaign has been carried out in collaboration with the Ruhr University of Bochum and RWTH of Aachen.

1.2.4 Char properties relevant to CCS-ready conversion

The usual approach for the analysis or prediction of the combustion or gasification of solid fuel particles is based on the assumption that fuel conversion takes place along a purely sequential path consisting of fuel pyrolysis succeeded by heterogeneous combustion/gasification of its char [6]. According to this framework, pyrolysis can be considered as the first chemical step in the overall solid fuel thermochemical process and has a significant influence on the subsequent stages [6].

The severity of heat treatment in the pyrolysis stage has great influence on thermal annealing and on the reactivity of the resulting char [9]. Recognition of the mutual interaction between thermally-induced structural modifications of carbon and the rate of heterogeneous reactions have also been documented by several investigators as early as in 1962 [83,84]. Senneca et al. [9] report that the effect of thermal annealing on the char-O_2 reaction is more severe than on the char-CO_2 reaction, to an extent that depends on the nature of the carbon material. They found that the different gasification reactivities of samples subjected to heat treatments of different severity (different heat treatment times, temperatures and/or rates) were larger in the early stage of gasification, levelling off at larger burn-off [9]. Experimental results were analyzed in the light of a phenomenological model according to char deactivation due to thermal annealing occurs in series-parallel to gasification [9]. Salatino et al. [85] compared the reactivity of fly ashes from a utility boiler with that of chars obtained in

laboratory from the same parent coal showing that fly ashes are less reactive than chars, and that the annealing mostly affects the pre-exponential factor rather than the activation energy.

Not only the severity of heat treatment, but also the presence of reactive species in the pyrolysis environment (e.g. O_2, CO_2, H_2O) are important for determining the properties of the char that is formed when coal is fed into a hot boiler and the following rate of burnout [6].

Senneca et al. [86], performing experiments in which heat treatment of the carbon sample was accompanied by exposure to oxygen, showed that char surface oxidation may effectively hinder thermal annealing. This was interpreted by assuming that stable surface oxides prevented the rearrangement of the turbostratic carbon structure by providing additional bonds and/or acting as "spacers" between graphene layers [86].

Several papers addressed the effect of CO_2-rich atmospheres from the early stages of coal particles heat up and pyrolysis in a boiler on the structure and reactivity of chars. Composition of the pyrolysis atmosphere may have important effects on the formation and properties of pyrolysis products, and controls also the characteristics of coal ignition, flame stability, fluidity, particle swelling, soot formation [87-93].

Pyrolysis of solid fuels has been studied for coal and biomass extensively. It is common knowledge, that several factors influence kinetics and product quality, with the most prominent being coal rank, process temperature, heating rate, pressure, particle size and gas atmosphere applied [94-96]. From an experimental point of view, the assessment of each of these parameters leads to a specific choice of reactor type.

When experiments under low heating rates are of interest, thermogravimetric analysis (TGA) is a suitable technique. Typical heating rates are below 100 K/min, which is orders of magnitude below the heating rates in pulverized fuel (PF) applications. Fixed beds have similar characteristics, but the sample mass is larger (grams or larger) compared to TGA, which is advantageous when a detailed analysis of the pyrolysis products is of interest [94-100]. Wire mesh reactors (WMR) (also known as heated grid reactors) are frequently used to investigate pyrolysis under fast heating conditions. WMR have in common with fixed beds and TGA that particles are in contact with the heating element. However, WMRs possess the advantage that heating rates from 100 K/s [101] to approx. 10^4 K/s [102-104] can be applied, which enables to cover a variety of process conditions.

Pyrolysis studies have also been carried out in fluidized bed reactors (FBR) [105,106]. The fluidization concept offers the advantage of higher heating rates compared to fixed beds and TGA,

while guaranteeing efficient mass transfer between particles and gas, which moves this technique closer to PF conditions with respect to the previously mentioned ones. Drop tube reactors (DTR) or entrained flow reactors (EFR) are the reactor types with highest heating rates (up to 10^6 K/s [107]) and process temperatures as well as shortest possible residence times. They fulfil all requirements to measure pyrolysis under PF conditions. As particle velocity and hence reaction time-scales can be well adjusted in the range of a few milliseconds, this reactor type can be used to derive pyrolysis kinetics under high heating rate and temperature conditions using fine particles [108-109]. However, these reactor types only provide a laminar co-flow as surrounding gas atmosphere, which makes a clear difference to real world PF conditions.

Some papers addressed the comparison of pyrolysis characteristics in different reactor types. Aylon et al. [110] studied the pyrolysis of waste tyre pieces in a fixed bed reactor and compared it to a moving bed, with the result that the moving bed provided better cracking of long chained pyrolysis products due to better heating and reactor specific differences resulting in longer gas residence times. Differences between TGA and fixed bed pyrolysis have been shown by Chen et al. [97], who found that the amount of non-condensable gases increases and the char yield is slightly reduced during fixed bed pyrolysis. Collot et al. [111] compared fixed and fluidized bed reactors for coal and biomass pyrolysis, where in a temperature range up to 1273 K and pressures up to 25 bar, little differences between both reactors were found, relative to the pyrolysis product yield. Trubetskaya et al. compared WMR and DTR pyrolysis of biomass samples with focus on char yield and properties [112] and found lower char yields from the DTR experiments. This was attributed to the higher heating rates (WMR: max. 5000 K/s). Guerrero et al. [113] studied eucalyptus chars from fixed bed (873–1173 K) and fluidized bed (1073–1173 K) pyrolysis experiments and found that volatile release increases along with both process temperature and heating rate. Accordingly, chemical composition, surface structure and porosity of the resulting chars were affected by temperature and heating rate.

Some studies investigated the differences between pyrolysis taking place in N_2- and CO_2-atmospheres, respectively. Wang et al. [114] studied coal and wood pyrolysis in non-isothermal TGA experiments and did not observe any influence of the gas atmosphere, which was confirmed in similar experiments of the same group [93]. In contrast, Su et al. [115] found that under fluidized bed conditions, i.e. 1173 K and heating rates in the range of 10^3–10^4 K/s, the amount of char resulting from pyrolysis decreased with increasing CO_2 concentration.

Coal particles of 4–5 mm diameter have been investigated by Bu et al. [116] in a fluidized bed and no difference in pyrolysis was found between the two atmospheres (in absence of oxygen). In EFR experiments at 1573 K and a residence time of 2.5 s, the apparent volatile release of different biomass samples was reported to be higher in CO_2 compared to N_2-atmospheres, which was attributed to the onset of gasification under these conditions [116]. Similar results were published by Rathnam et al. [117], who devolatilized different coals in a DTR at 1673 K.

A recent work from Heuer et al. investigated the influence of CO_2 in the very early stages of coal pyrolysis in a drop tube reactor at 1573 K [80]. The residence time was carefully chosen so as to assure the completion of pyrolysis while limiting the progress of char combustion and gasification. A remarkable effect was noticed on all reaction products. Substituting N_2 or Ar with CO_2 the concentration of acetylene increased, while most other hydrocarbon species were abated. Finally, in CO_2 a much larger abundance of fine carbon particulate, constituted by char and soot-like particles mixed together, was observed over Ar or N_2 conditions. [81].

The relevance of CO_2 rich atmosphere, typical of oxyfiring combustion, on the production of soot-like received attention in the literature only recently. It is well known that during the initial phases of coal combustion the volatiles typically burn in jets or more commonly in envelope flames which surround the individual particles and provide energy feedback to the char particles. However, under some circumstances, volatiles can evolve into submicronic (fine and ultrafine) carbon particles, often referred to as soot-like. Senneca et al. [119] reports a detailed experimental investigation of the sub-micrometric carbon particulate/soot-like formed upon the fast coal pyrolysis experiments in N_2 and CO_2 atmospheres described in Ref. [80]. Finally, Borrego et al. [120] who pyrolyzed a hv and a low volatile (lv) bit. coal in a DTR with 300 ms residence time found an even lower volatile release in CO_2 than in N_2 at 1573 K and suggested that CO_2 could be involved in some cross-linking reactions during incipient char formation which would also reduce particle swelling.

The rate of char conversion in an oxy-fuel environment has also been object of several research papers in recent literature with rather controversial results, so that to date it is not yet quite clear whether using CO_2 as diluent would increase or decrease the overall rate of combustion [117,118,121,122-127]. Some publications support the idea that the rate of char conversion is lower in oxy-fuel environments compared to air [124] due to the lower molecular diffusivity of O_2 in CO_2 compared to N_2. Other authors instead support the opposite idea that char conversion rate under oxy-fuel conditions is enhanced compared to traditional combustion due to the contribution of the Boudouard

reaction [127]. Some others, finally, report that the coal conversion rate may be either enhanced or lowered by the use of CO_2 as diluents, depending on the temperature, O_2 level and coal rank [118,125,126]. The discrepancy on the effect of CO_2 on char burning rate could be partly reconciled when differences in reaction conditions as well as in coal rank and char preparation methods used in the published experimental works are considered.

Under conditions typical of pulverized coal combustion, the char-O_2 reaction occurs typically under regime II conditions. Accurate assessment of the char oxy-combustion kinetics at high temperature is a prerequisite for the correct estimation of the performance of PF-combustors.

Notably, most studies reported in the literature on the kinetics of coal oxy-combustion are based on TGA experiments at relatively low temperature. Limited data have been obtained under conditions resembling or approaching suspension firing. Senneca et al. [126] compared the rate of char conversion on in O_2/CO_2 mixtures by means of thermogravimetric analysis and in an aerodynamic levitated particle reactor, in order to investigate a wide range of temperature within which kinetic measurements were significant. Arrhenius plots revealed the existence of multiple linearity regions which could not be fitted by traditional kinetic models. The authors [126] suggested that at high temperature, when both the reactions with oxygen and carbon dioxide occur, the two reactants may compete for the carbon active sites generating unexpected results in terms of the overall rate of reaction. Recently, Wang et al. [128] showed by means of atomistic simulation tools that evolution of char micro-structure and porosity in oxy-combustion can be different compared to air combustion. However, according to Senneca et al. [6], the development of reliable models and predictive tools for coal/char oxidation under "*extreme conditions*" require, at first instance, an extensive characterization of the properties of the resulting char, of the course of heterogeneous oxidation of char by competing oxidants (O_2, CO_2), and of the effect of heterogeneous oxidation on the modifications of microstructural properties of the solid fuel [6].

Chapter 2

Experimental methods for the characterization of carbon materials

Coal structure can have an influence on conversion processes such as combustion and gasification. An understanding of coal structure and thermal behaviour can assist with predicting and controlling these processes. Although many techniques, including XPS [129-153], TGA [145-171], XRD [172-178], FTIR [179-181], Raman spectroscopy [182-184] and BET [185-189], have been applied to determine coal structure, it has yet to be fully understood due to its complexity and heterogeneity. However, a reasonable understanding of coal structure is possible combining information obtained from different techniques.

2.1.1 X-ray Photoelectron Spectroscopy

XPS (X-ray photoelectron spectroscopy) refers to the process in which an electron is removed from a specimen after the atomic absorption of a photon. The first evidence of this phenomenon dates back to 1887 when Heinrich Hertz detected electrons emitted from a secondary arc due to irradiation of ultraviolet light [129]. It was not until 1905 that Einstein offered an explanation of this effect [130], which is now referred to as 'the photoelectric effect'. Einstein recognized that when light is incident on a sample, an electron can absorb a photon and escape from the material with a maximum kinetic energy [130]:

$$E_k = h\nu - K_b - \Phi \qquad (2.1)$$

where ν is the photon frequency, K_b electron binding energy and Φ work function, which gives the minimum energy required to remove a delocalised electron from the surface of the metal. By measuring the kinetic energy of the emitted electrons, it is possible to determine which elements are near a material's surface, their chemical states and the binding energy of the electron. The binding energy depends upon a number of factors, including the following [131]:

- ✓ the element from which the electron is emitted;
- ✓ the orbital from which the electron is ejected;
- ✓ the chemical environment of the atom from which the electron was emitted.

Concentration of elements (C_x) is correlated with the intensity of the XPS peaks (I_x) weighted by sensitivity factor S_x [131]:

$$I_x = C_x S_x \tag{2.2}$$

$$S_x = F\sigma_{x(hv,K_b)} D\lambda_{K_b} \tag{2.3}$$

where F the X-ray flux, σ the photoelectron cross-section (probability of a electron being emitted from its electronic state), D the detector efficiency and λ the inelastic electron mean free path (the distance that a photoemitted electron can travel through a thin film before losing its energy)[131].
XPS is among the most powerful analytical methods for probing the surface of carbon materials. Due to its high sensibility to the chemical nature and environment of atomic species, XPS has been extensively exploited as a mean to identify the nature of the carbon-oxygen functionalities forming at various temperatures on the surface of different types of carbon materials [28,132-139]. XPS is a localized probe and thus suitable for studying local structures. Moreover, the ionization cross sections for the XPS core-level spectra are exclusively dependent on atomic factors and independent on the chemical state of the atoms [137]. As a consequence, the intensities of the core-level peaks are directly proportional to the density of atoms, and can be used to estimate the relative abundance of chemical groups and atomic species.

In recent years, many detailed experimental studies [27,28,135,141-143] have focused on the use of XPS to characterize the surface of graphite and graphene oxides in order to gain a better understanding of the mechanical and electronic properties of these materials. Larciprete et al. [27,28] employed high energy resolution XPS spectroscopy (HR-XPS) with synchrotron radiation in conjunction with ab initio calculations to probe the species residing on highly oriented pyrolytic graphite (HOPG) surface oxidized at room-temperature with atomic oxygen, and those released in the gas phase during heating. From *C1s* and *O1s* core-level spectra and valence band analysis they found that, at low oxidation stage, epoxy is the dominant surface species, while, at high oxidation levels, ethers and C=O bonds arise as a result of O saturation of vacancies and dangling bonds at the edges. Their results are in

agreement with those of Barinov et al. [135] who also studied the initial oxidation stages of graphitic surfaces exposed to atomic oxygen by means of high-resolution XPS. They come to the conclusion that surface epoxide formation is accompanied by saturation of carbon vacancies leading to ether and carbonyl functional groups [135]. Finally, Kin et al. [143] investigated the structural and chemical stability of graphene oxide films by XPS and density functional theory (DFT). By analysis of *C1s* and *O1s* core-level spectra they proved that the epoxy groups formed initially on the surface tend to be reduced by C-H species to hydroxyl, with the latter eventually undergoing further reduction to release water molecule [143].

Various XPS studies on low and mild temperature oxidation of coals are found in the literature [133,137-139]. They mainly focus on the investigation of the detrimental changes in surface properties of coals during natural oxidation and weathering [137-138], and on the influence of the oxidation processes on sulphur speciation [139]. Each author agrees with the fact that, due to the complex structure and intrinsic heterogeneity of coal, an exact characterisation of surface oxygen species is difficult. Two conclusions are generally drawn from analysis of *C1s* XPS spectra of coals: sulphur contents and coal rank highly influence the rate and mechanism of the oxidation processes, the initial formation of hydroxyl groups and ether linkages on the coal surface is followed by the transformation of C-O groups to carbonyl and carboxyl groups ((H)O-C=O) [137-139]. However, in all these works, core-level peak assignments are not substantiated by theoretical calculations, nor any reference to calculated values of binding energies obtained from previous works is done. Assignment of the *C1s* and *O1s* core-level peaks of the spectra acquired in the Doctoral Thesis were made on the base of the procedure used by Levi et al. in [144,145].

The ***Chapter 3*** of the Doctoral Thesis, reports the results of e XPS experiments performed in the ultra high vacuum chamber (UHV) (base pressure 8×10^{-11} mbar) of the SuperESCA beamline at the Elettra synchrotron radiation facility (Trieste, Italy). Details about the parameters of the Elettra storage ring and a technical description of the SuperESCA beamline are provided in *Appendix I.*

Main purpose of the analysis was to identify and determine the relative abundance of the carbon-oxygen species forming on the surface of the coal samples after oxidation in air and thermal desorption. Moreover, analysis of the *C1s* allowed to monitor the structural evolution of the coals surface in terms of extension of the carbon sp^2 conjugation with respect to carbon sp^3, carbon vacancies and oxidized carbon. The use of synchrotron radiation, which combines high resolution

capabilities with the high flux of linearly polarised photons, was necessary to optimally resolve the components of the core-level spectra.

In ***Chapter 4*** core-level XPS measurements are reported carried out by an UHV set-up equipped with a *Gammadata-Scienta SES 2002* analyzer set in Ruhr University. The fitting procedure was based on the deconvolution proposed in ***Chapter 3***.

2.1.2 Core-level band assignment

Assignment of the *C1s* and *O1s* core-level peaks of the spectra acquired in the present study were based on the procedure developed by Levi et al. [144,145], using calculated values of chemical shifts taken from published studies [132,135,139,142,146,148].

Zhang et al. [142] calculated core chemical shifts of *C1s* orbital for possible oxidation species in graphene oxide using density functional theory, and compared them to experimental XPS spectra. They used a ΔSCF-ECP approach, performing the binding energy calculations at the BP (Becke correlation and Perdew exchange functionals) level of theory. The basis set employed is the polarized valence triple zeta basis IGLO III. Graphene oxide was simulated with cluster models with dangling bonds saturated with hydrogen and containing various carbon-oxygen functionalities in different configurations: single epoxy on the surface, two edge C=O carbonyl groups, carboxyl group at the edge, two OH hydroxyl groups on the surface, five- and six-ring lactol groups, hydroxy-epoxy pairs, ether groups saturating carbon vacancies in distinct configurations. As an example, two of the model cluster used by Zhang et al. [142] are reported in Fig.2.1, taken by [142]:

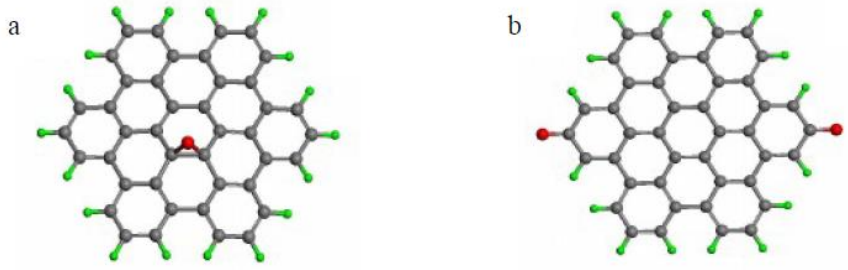

Fig.2.1. Two examples of Cluster models used by Zhang et al. [142] to calculate *C1s* binding energies. In grey carbon atoms, in green hydrogen, in red oxygen.
(a) A single epoxide group on the surface. (b) Two edge C=O carbonyl groups. Fig. taken by [142].

The calculated average binding energy of the epoxide group (287.2 eV) was set as a reference to calculate relative core chemical shifts. Table 2.1, taken by [142], reports the absolute *C1s* binding energies of different carbon-oxygen species deduced from the corresponding relative core chemical shifts as calculated by Zhang et al. [142].

Table 2.1. Absolute *C1s* binding energies (BE) in electronvolts (eV) of various oxidation species calculated by Zhang et al. [142]by DFT at the BP-IGLO III level. Table taken by [142].

Chemical group	***BE (eV)***
C-H	285.4
C sp^2	285.5
C-O-C ether	286.5-286.7
C-OH	287.3
C-O epoxy	287.2
C=O	286.5
O=C-O(H)	288.5-289.1

The work by Barinov et al. [135] was also considered as a reference. Barinov et al. performed DFT calculations to interpret high-resolution XPS spectra of perfect and defective graphitic surfaces exposed to atomic oxygen. Their DFT calculations were based on the PBE-GGA formalism, which makes use of the Perdew-Burke-Ernzerhof exchange and correlation energy functionals, and were implemented in the plane-waves pseudopotential framework. The oxidized surface of perfect and defective graphite was modelled with atomic oxygen adatoms on (7 × 7) and (5 × 5) periodic supercell three-layer thick slabs separated by 14 Å of vacuum. The *O1s* and *C1s* core level shifts were calculated using the final state theory, which allows to take into account differences in the screening of the photon-induced holes. Thus, binding energy (BE) shifts were approximated by differences in the total energies calculated in models containing an excited atom at different positions. The overall accuracy of the final state approximation was estimated to be better than 0.2 eV from comparison between simulation and experiment for the epoxy group on the surface of perfect HOPG. The carbon sp^2 *C1s* peak at 284.5 eV and the *O1s* peak at 532.3 eV relative to epoxide in the experimental spectra were taken as a common reference to compare results from experiments with calculated relative core chemical shifts. The resultant calculated *C1s* and *O1s* ionization energies of the carbon-oxygen

groups investigated are reported in Table 2.2, taken by [135]. For those oxidation species that have been considered in different local environments more than one value is given.

Table 2.2. Absolute *C1s* binding energies (BE) in electronvolt (eV) of various carbon-oxygen groups calculated by Barinov et al. [135] by DFT at the PBE-GGA level in the plane-waves pseudopotential approximation. Table taken by [135].

Chemical group	***C1s BE (eV)***	***O1s BE (eV)***
C sp^2	284.5	
C vacancy [a]	283.4-284.2	
C-C(O) [b]	283.9-285.0	
C-O epoxy	286.1-286.3	532.3
C-O-C ether	285.7-285.9	534.2-534.7
C=O	285.7	531.4-531.5

[a] C atoms surrounding a single C surface vacancy
[b] nearest and next nearest neighbours to O bonded C atoms

Levi et al. [144,145] comparing carbon *C1s* absolute ionization energies in Table 2.1 with those in Table 2.2, found a discrepancy between individual values of corresponding chemical species. The discrepancy was readily explained: the absolute *C1s* binding energies reported in Table 2.1 were calculated from the relative chemical shifts given by Zhang et al. and the calculated average binding energy of the epoxide group (287.2 eV) reported by the authors [142]. Taking as a common reference the experimental value of 284.5 eV relative to carbon sp^2 *C1s* peak reported by Barinov et al., new values of absolute binding energies were calculated from relative chemical shifts provided by Zhang et al. The following Table 2.3, taken by [144], reports the absolute binding energies obtained by Levi et al., comparing the values already given in Table 2.2 with the new calculated values from Zhang et al. [144]. Assignment of the *C1s* and *O1s* core-level peaks of the spectra acquired in the Doctoral Thesis were made on the base of calculated values of chemical shifts by Levi et al. reported in Table 2.3 [144].

Table 2.3. Absolute *C1s* binding energies (BE) in electronvolt (eV) of various carbon-oxygen groups obtained from Zhang et al. [142] and Barinov et al. [135]. Values were calculated from computed chemical shifts and the experimental reference value of 284.5 for *C sp²* binding energy. Table taken by [144].

	BPE-PW[135]		***PB-IGLO III[142]***
Chemical group	***C1s***	***O1s***	***C1s***
C-H			284.4
C sp²	284.5		284.5
C vacancy [a]	283.4-284.2		
C-C(O) [b]	283.9-285.0		
C-O epoxy	286.1-286.3	532.3	286.2
C-OH			286.3
C-O-C ether	285.7-285.9	534.2-534.7	285.5-285.7
C=O	285.7	531.4-531.5	285.5
O=C-O(H)			287.5-288.1

[a] C atoms surrounding a single C surface vacancy
[b] nearest and next nearest neighbours to O bonded C atoms

Barinov et al. [135], introduced two bands in the *C1s* spectra at lower and higher binding energies with respect to the *C sp²* peak at 284.5 eV, attributed to C atoms surrounding surface vacancies and C atoms neighbours to carbon-oxygen sites. An inclusion of these additional peaks in the *C1s* XPS spectra of coals with respect to the spectrum of a perfect graphitic surface is required due to the high density of defects that characterizes these materials [144]. Moreover, due to the established presence of *sp³* carbons in the structure of the coal samples under examination a component at around 285.0 eV was included in the fitting procedure [144]. The value of 285.0 eV for *C sp³* was deduced, by Levi et al. [144], from theoretical and experimental works found in the literature [140,147]. Furthermore, from analysis of the reported *C1s* binding energies values for C-O species, it is clear that C-O epoxy and C-OH hydroxy group, having very close *C1s* binding energies, contribute to the same *C1s* core-level peak. The same is valid for C-O-C ether and C=O carbonyl groups [144]. As for the *O1s* core-level peak theoretical assignment, DFT calculations by Barinov et al. do not cover all the possible C-O functionalities: *O1s* binding energies for C-OH hydroxyl and O=C-O(H) carboxylic and lactol groups are not given [135]. Levi et al. [144] assigned the *O1s* core-level peaks based on the results of Yamada et al. [141] and Larciprete et al. [27,28]. In particular, Yamada et al. [141] using DFT at

the B3LYP/6-31G(d) level calculated *O1s* binding energies of various graphene models containing C-O functionalities in a Koopmans' theorem based approximation. They used the calculated values to assign the *O1s* core-level peaks in experimental XPS spectra of graphite oxides. A peak at 533.2 was identified and assigned to both ether groups and sp^2 C–OH. Moreover, they stated that a peak at 532.2 rises from the contributions of both O=C-O(H) and epoxide groups [141]. Larciprete et al. [27,28] measured the *O1s* core-level binding energies on the surface of HOPG oxidized by atomic oxygen by means of high-resolution XPS with synchrotron radiation, and assigned a peak between 530 and 531 eV to both C=O and O=C-O(H).

2.1.3. Core-level lineshape analysis

To fit the core-level XPS peaks requires the convolution of Gaussians and Lorentzians functions [148]. The Lorentzian component accounts for the finite lifetime of the core hole state in the photoionization process; thus, it represents the natural linewidth of the XPS signal. The Lorentzian lineshape takes the following analytical form [148]:

$$Y_L\,(E) = \frac{1}{1 + 4\ (\frac{E - E_L}{\Gamma_L})^2} \tag{2.4}$$

where E_L is the binding energy at which the curve shows a maximum, and Γ_L is the full width at half maximum (FWHM). The Lorentzian width is independent of the photon energy used to probe the core level [148], and does not vary very much with the chemical environment of the atoms involved in the photoemission process. For these reasons, it is usually kept constant in fitting procedures.

The Gaussian lineshape is used to consider the instrumental broadening and the phonon broadening of the core level [148]. Its analytical expression is:

$$Y_G(E) = \exp[-4\ln 2(\frac{E - E_G}{\Gamma_G})^2\,] \tag{2.5}$$

where E_G is the binding energy at which the function shows a maximum, and Γ_G is the FWHM. Phonon broadening depends strongly on the chemical environment and on temperature. Conversely, the instrumental broadening holds for all materials at all temperatures. This kind of broadening may be expressed by an instrument response function [148] that depends on the features and parameters of the electron analyser and monochromator, such as pass energy and groove density of the diffraction grating.

Convolution of a Gaussian and a Lorentzian gives a Voigt profile. The Voigt function has been shown to correctly describe the core level emissions of insulators and semiconductors [148]. On the other hand, conductor materials exhibit peculiar lineshapes that require the use of slightly different functions to describe them. Indeed, X-ray photoemission lineshapes of the core electrons in conductors display a characteristic asymmetry on the high binding energy side that cannot be ascribed solely to the contribution of inelastically scattered electrons. Doniach and Šunjić [149] proved that the peculiar skewness of XPS core-level lineshapes of metals is due to the many-electron interactions of the metallic conduction electrons with the core positive hole in the final state. More specifically, the ejection of a photoelectron from a metal surface is followed by a re-adjustment of the ground state of the Fermi gas to the sudden appearance of the hole potential. This results in the formation of electron-hole pair excitations at the Fermi level, which are responsible for the screening of the potential and the consequent asymmetry of the XPS lineshapes. The two authors developed a function to describe the natural linewidth of the XPS core-level peaks of metals that contains an asymmetry parameter. The Doniach-Šunjić function takes the following analytical form [149]:

$$DS(E) = \frac{\Gamma(1-\alpha)\cos[\frac{\alpha\pi}{2} + (1-\alpha)\arctan\left(2\left(\frac{E-E_L}{\Gamma_L}\right)\right)]}{[(E-E_L)^2 + 4\,\Gamma_L^2]^{\frac{1-\alpha}{2}}} \qquad (2.6)$$

where Γ is the gamma function, E_L and Γ_L are defined as in eq.2.4, and α, the singularity index, indicates the amount of asymmetry.

For all but a few metals α is not calculated, but obtained by fitting core-level spectra [150]. In non-conductors systems, due to the low presence of electron-hole pair excitations, the screening of the core hole potential is negligible and α is very small. When α is zero the Doniach-Šunjić function reduces to a Lorentzian function.

The Doniac-Šunjić function is commonly used to fit the XPS core-level spectra of graphite, aromatic molecules and coals [28,135,140,151-153]. It allows, in fact, to consider the intrinsic asymmetric nature of the lineshape deriving from the screening effects of the π electrons delocalized on the aromatic domains.

2.2. Thermoanalytical methods

Thermal analysis methods, such as thermogravimetry (TG), differential thermal analysis (DTA), and differential scanning calorimetry (DSC), have been employed extensively in investigations relating to coal and biomass utilization [154].

Thermogravimetric analysis (TGA) is one of the most common techniques used to rapidly investigate and compare thermal events and kinetics of combustion and pyrolysis of solid raw materials, such as coal and biomass [154-161]. TGA allows to measure the mass loss of a sample as a function of time/temperature. The temperatures at which combustion or decomposition reactions in the sample start can also be followed by TGA [154]. Quantitative methods can be also applied to TGA curves in order to obtain kinetic parameters [162-163].

The rate of a solid-state degradation reaction can be generally described by [154-163]:

$$\frac{d\alpha}{dt} = k(T)f(\alpha) \tag{2.7}$$

where α is the conversion fraction, t is the time, $k(T)$ is the rate constant depending on temperature, T is the absolute temperature and $f(\alpha)$ is a function depending on the reaction mechanism. Integrating the above equation, in isothermal condition, gives the integral rate law:

$$g(\alpha) = \int_0^{\alpha} \frac{d\alpha}{f(\alpha)} = k(T)t \tag{2.8}$$

where $g(\alpha)$ is integrated form of the reaction model. The reaction model $f(\alpha)$ and $g(\alpha)$ may take various forms, some of which are shown in Table 2.4, taken by [154]. The explicit temperature dependence of the rate constant, is usually described by the Arrhenius equation:

$$k(T) = A\, e^{-E_a/RT} \tag{2.9}$$

where A (the pre-exponential factor) and E_a (the activation energy) are the Arrhenius parameters and R is the gas constant. The Arrhenius parameters, together with the reaction model, are sometimes called the kinetic triplet. Substituting eq.2.9 in the above two rate expressions gives:

$$\frac{d\alpha}{dt} = A\, e^{-\frac{E_a}{RT}} f(\alpha) \tag{2.10}$$

$$g(\alpha) = A\, e^{-\frac{E_a}{RT}}\, t \tag{2.11}$$

Kinetic parameters can be obtained from TGA measurements by applying model-fitting methods or isoconversional (model-free) methods either for non-isothermal or isothermal tests.

Model-fitting methods involve the choice of a reaction model [162,163], some of which are shown in Table 2.4 [154]. In particular:

- for treatment of non-isothermal kinetics data, kinetic parameters can be estimate from linear regression applying:

$$\ln\left(\frac{d\alpha}{dt}.\frac{1}{f(\alpha)}\right) = \ln A - \frac{E_a}{RT} \tag{2.12}$$

- for treatment of isothermal kinetics data, the first fit determines the model, *g(α)*, that best fits the isothermal data, while the second determines specific kinetic parameters applying the Arrhenius equation.

Isoconversional methods, instead, calculate E_a values at progressive degrees of conversion without any modellistic assumptions [162,163]:

- for treatment of non-isothermal kinetics data, model-free methods allow estimating kinetic parameters solving:

$$-\ln t = \ln\frac{A}{g(\alpha)} - \frac{E_a}{RT} \tag{2.13}$$

  A plot of $-\ln t$ versus $1/T$, each α yields E_a (from the slope) for that α regardless of the model.

- finally, for treatment of non-isothermal kinetics data several model-free methods have been proposed including the differential method of Friedman, the integral methods of Ozawa as well as of Flynn and Wall [163].

Cumming and McLaughlin [164] indicated that the information obtained from TGA combustion profiles can be used for a first initial evaluation of the combustion behaviour at industrial scale. TGA techniques operate at different conditions to those encountered in a pulverised coal combustor. In fact, intrinsic char reactivity is investigated in TGA at relatively low temperatures, when reaction rates are relatively low. This allows spurious effects due to diffusion limitations to be avoided [165].

Other bench equipment such as drop tube furnaces and entrained flow reactors simulate more closely the combustion conditions of industrial pf combustors. Since the pilot- and full-scale tests are costly to operate, TGA measurements can help in the understanding of coal combustion behaviour and is very useful from a fundamental viewpoint, and for comparison between samples [154].

Despite the well known exothermicity of the entire processes of solid fuel utilization, detailed thermochemical studies of the individual steps that contribute to carbon combustion are lacking. The formation and thermal decomposition of surface oxides at very low temperatures (< 300 K) has been investigated by Wang et al. [15,22] with a focus on self-heating and spontaneous combustion of coal. Some early work on oxygen chemisorption thermicity on carbon at moderate temperature, have shown a moderately exothermic behaviour [166], while abstraction of CO and CO_2 during the desorption step is considered endothermic [167,168]. Haynes and coworkers [24] found, in the early stage of desorption, when mostly CO_2 is released, an exotherm desorption balanced off by a pronounced endotherm of desorption when CO desorption in the later stages.

In a recent study Senneca et al. [145,169] investigated the thermicity of reactions occurring during oxidation at 570 and 770 K and during temperature programmed desorption (TPD) of samples of bituminous coal. Thermoanalytical methods (DTG, DSC, TPD) were used to identify the key reactive steps (chemisorption, structural rearrangement and switch-over of surface oxides, desorption) and their energetics [145,169].

They found that oxygen chemisorption is moderately exothermic (with ΔH=-4 KJ/g), and TPD is overall exothermic (ΔH=-14 kJ/g). In TPD experiments a pronounced exotherm was recorded already at 470 K, when the DTG profile associated with mass loss of the samples was flat and well before the sample started to release CO_2. When, at higher temperature, desorption of CO and CO_2 took place, minima in the DSC curves were recorded. Comparison of the *O1s* spectra, provided a tool to characterize the nature of oxygen bonding on carbon and to determine the relative abundance of carbon-oxygen species. It was shown that the most abundant oxygen functionality in the raw char is epoxy. The rearrangement of epoxy during oxidation occurred together with activation of the more stable and less reactive carbon sites. Results underline the key role of epoxy groups in the early stages of oxidation, providing a mechanistic framework for the identification of the stable and metastable intermediates in the heterogeneous oxidation of coal by molecular oxygen [145].

The exothermicity of the oxidation step was explained based on a mechanism that assumes that oxygen is first uptaken in a metastable form at moderate temperature; metastable surface oxides may

be stabilized at higher temperatures into more energetically favourable carbon-oxygen functional groups, and this exothermic process eventually overcomes the endothermic behaviour associated with abstraction of CO and CO_2 from the surface of the carbonaceous material [145].

Indeed, the beneficial role of oxidation has already been highlighted by Senneca et al., where it was indicated as a measure to reactivate and enhance the combustion rate of carbon with intrinsic low reactivity, such as residual carbon in ash from PF boilers [169-171].

Table 2.4. Set of reaction models applied to describe thermal decomposition in solids. Table taken by [154].

Reaction model	***f(α)***	***g(α)***
Power law	$4\alpha^{3/4}$	$\alpha^{1/4}$
Power law	$3\alpha^{2/3}$	$\alpha^{1/3}$
Power law	$2\alpha^{1/2}$	$\alpha^{1/2}$
Power law	$2/3\alpha^{-1/2}$	$\alpha^{3/2}$
Power law	$1/2\alpha^{-1}$	α^{2}
One-dimensional diffusion	$1-\alpha$	$-\ln(1-\alpha)$
Mampel (first-order)	$4(1-\alpha)[-\ln(1-\alpha)]^{3/4}$	$[-\ln(1-\alpha)]^{1/4}$
Avrami–Erofeev	$3(1-\alpha)[-\ln(1-\alpha)]^{2/3}$	$[-\ln(1-\alpha)]^{1/3}$
Avrami–Erofeev	$2(1-\alpha)[-\ln(1-\alpha)]^{1/2}$	$[-\ln(1-\alpha)]^{1/2}$
Avrami–Erofeev	$2(1-\alpha)^{2/3}(1-(1-\alpha)^{1/3})^{-1}$	$[1-(1-\alpha)^{1/3}]^{2}$
Three-dimensional diffusion	$3(1-\alpha)^{2/3}$	$1-(1-\alpha)^{1/3}$
Contracting sphere	$2(1-\alpha)^{1/2}$	$1-(1-\alpha)^{1/2}$
Contracting cylinder	$(1-\alpha)^{2}$	$(1-\alpha)^{-1}-1$
Second-order	$4\alpha^{3/4}$	$\alpha^{1/4}$

2.3 X-ray Diffraction

X-ray Diffraction (XRD) analysis is a fundamental method for evaluating mineral matter composition and carbon stacking structure of coal. X-ray diffraction is a non-destructive and well-established technique with good reproducibility. This technique offers a particular advantage to use a relatively large amount of sample (≈ 200 mg), and, therefore, the properties yielded represent average properties for the examined sample [172].

The presence of mineral matter adversely affects most aspects of coal utilization and processing. Mineral matter is the inert solid material in the coal which remains behind in a slightly altered form as ash after coal combustion. High ash content can lead to technical difficulties for utilizing the coal with lower efficiency and higher costs of power plants. Some specific problems with high ash content in coal include high ash disposal requirements, corrosion of boiler walls, fouling of economizer sand high fly ash emissions [173]. Table 2.5, taken by [174], summarizes the minerals commonly occurring in coals.

Table 2.5. Mineral matters in coal. Table taken by [174].

Mineral	***Group***	***Mineral***	***Group***
Clay	Kaolinite, Muscivite, Illite, Smectite	**Carbonates**	Calcite, Aragonite, Dolomite, Ankerite, Siderite
Oxydes	Quartz, Rutile, Anatase	**Feldspars**	Orthoclase, Microcline, Plagioclase
Sulfides	Pyrite, Marcasite	**Phosphates**	Apatite, Crandallite, Gorceixite, Goyazite,
Sulfates	Gypsum, Alunite, Jarosite		

The carbon stacking structure of coal contains short-range graphite-like structures, i.e. crystalline carbons, which are extremely small, giving rising to three diffuse peaks. These peaks correspond to the (00l) and (hk0) reflections of graphite [175,176]. In particular, the (002) peak corresponds to the inter-layer spacing of graphite, while (100) and (110) peaks arise from hexagonal ring structure. The asymmetric feature of the (002) band suggests the existence of another band (γ) on the left side. The γ band represents the saturated structure such as aliphatic side chains, which is grafted on the edges of coal crystallites [177,178]. In addition to the graphite-like structure, coal has a significant amount of highly disordered material, amorphous carbon, which contributes to the background intensity.

Fig. 2.2, taken by [172], is a schematic illustration of the simplified coal structure. Unlike graphite, coal crystallite is extremely small and contains significant amounts of aliphatic side chains on its edges (Fig. 2.2a taken by [172]). These small crystallites can be linked via their side chains to form the so-called macromolecule, with the amorphous carbon being trapped in it (Fig.2.2b and c taken by [172]).

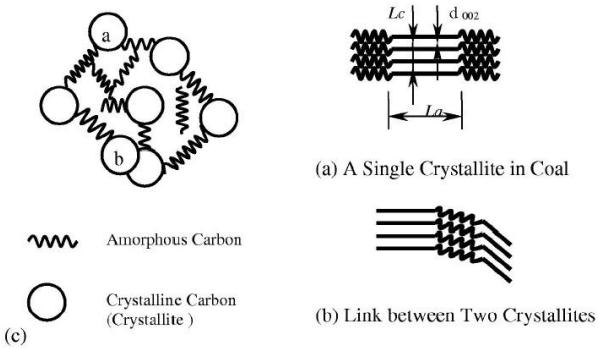

Fig.2.2. Schematic illustration of the simplified coal structure based on XRD observations. Fig. taken by [172].

The inter-layer spacing (d_{002}), and the crystallite size (average stacking height (L_c), average diameter (L_c)) have been established as the parameters for evaluating the stacking structure of highly crystalline carbon materials [172]. The inter-layer spacing of aromatic layers (d_{002}) is calculated from the peak position by means of Bragg's equation:

$$2dsen\theta = n\lambda \tag{2.14}$$

where θ is the scattering angle, n a positive integer and λ is the wavelength of incident wave.

The average stacking height (L_c) and average diameter (L_a) of the layer structure, are calculated by means of Scherrer 's equation [172]:

$$L_a = 1.84\lambda \,/\, (B_a \, cos\phi_a)$$

$$L_c = 1.84\lambda \,/\, (B_c \, cos\phi_c) \tag{2.15}$$

where λ is the wavelength of X-ray used, B_a and B_c are the half width of the (100) and (002) peaks and ϕ_a and ϕ_c are the corresponding scattering angles.

2.4 Fourier Transform Infrared Spectroscopy

Fourier transform infrared (FT-IR) spectroscopy is a widely adapted analytical technique for determining the different functional groups in coal structure. This technique, is able to reveal carbo-hydrogenated structures (aromatic and aliphatic) and heteroatomic functions (mainly oxygenated), as well as to perceive the presence of minerals [179-181]. The sample is exposed to continuously changing wavelengths of infrared radiation absorbs light when the incident radiation corresponds to the energy of a particular molecular vibration (both stretching and bending).

Energies of the stretching vibrations correspond to infrared radiation with wave numbers between 1200 and 4000 cm^{-1}, while the bending vibration is in the range of 500-1200 cm^{-1}. This part of the infrared spectrum is particularly useful for detecting the presence of functional groups, because these groups have characteristic and invariant absorption peaks at these wavelengths [179-181]. Table 2.6, taken by [181], reports the band assignments for the Infrared Spectra of coal.

Table 2.6. Band assignments for the Infrared Spectra of coal. Table taken by [181].

Bands (cm^{-1})	***Assignment***	***Bands (cm^{-1})***	***Assignment***
540	Clay and silicate minerals	2851	Aliphatic symmetric -CH_2 stretching
669	Aromatic out of plane C-H deformations	2920	Aliphatic asymmetric -CH_2 stretching
1032-1090	Silicate minerals	3618-3620	Clay minerals
1375	Stretching modes of methyl group	3696-3700	Kaolinite and illite minerals
1600	C=C aromatic stretching		

2.5 Raman Spectroscopy

The Raman spectrum of graphite was first recorded more than 40 years ago and, by the time the Raman spectrum of graphene was first measured in 2006, Raman spectroscopy had become one of the most popular techniques for the characterization of disordered and amorphous carbons, fullerenes, nanotubes, diamonds, carbon chains and polyconjugated molecules [182-184].

The Raman signals graphite crystals and graphene layers result from lattice vibrations (phonons) and are very sensitive to the degree of structural disorder. Indeed, Raman scattering on phonons is to a large extent determined by electrons: how they move, interfere and scatter [182-184]. Thus, any variation of electronic properties due to defects, edges, doping or magnetic fields affects positions, widths and intensities of the Raman peaks, enabling one to probe electrons via phonons. It follows,

then, that one of the most prominent prerogatives of Raman spectroscopy applied to the structural analysis of carbon-based materials is its sensitivity to the degree of extension and defectiveness of the graphene-like layers that comprise their structure [182-184].

The review of Ferrari et.al. [182] provides a valuable reference for the assignment of the peaks of the Raman spectrum of carbonaceous materials. The first-order Raman spectra of graphene and graphite are essentially identical, and are characterised by a single peak, called G band, corresponding to the high-frequency (1580 cm^{-1}[182-184]). The spectra of polycrystalline graphites and defective graphene, on the other hand, exhibit additional first-order bands (generally referred to as D or 'Defect' bands [182-184]), which are known to arise from structural defects (edges, carbon vacancies, presence of heteroatoms and intercalated compounds) and to grow in intensity relative to the G band with increasing degree of disorder. In polycrystalline carbonaceous materials consisting of large numbers of small graphitic crystallites (like coals and related materials), carbon atoms at the edges of graphene layers are considered as the most probable origin of the D band [182-184]. The D band is usually observed around 1350 cm^{-1} in the Raman spectrum. Another first-order band accounting for structural disorder is the D_2 band at 1620 cm^{-1} which can be observed as a shoulder on the G band. Disordered nanocrystalline carbon material exhibit another distinctive feature at around 1500 cm^{-1}. This peak, usually referred to as the D_3 band, originates from the amorphous carbon fraction of the solid (small PAHs, aliphatic residues, functional groups containing heteroatoms), and is located between the two peak maxima (the D and G bands) [182].

Furthermore, the D peak at 1350 cm^{-1} in the Raman spectra of amorphous carbon material can exhibit a shoulder between 1190 and 1200 cm^{-1}, which was denominated as D_4, and was tentatively attributed to sp^2-sp^3 bonds or C–C and C=C stretching vibrations of polyene-like structures [184].

2.6 Surface Area mearurement

Surface area estimates are useful for understanding the pore structure evolution of carbon materials such as coal and char throughout thermochemical processes. Typically, the surface area of a porous material is determined using the model of Brunauer, Emmett and Teller (BET) and the adsorption isotherm of nitrogen at 77 K [185]. The derivation of the BET equation is based on Langmuir's analysis for unimolecular layers. The BET model uses a layer by layer version of the adsorbate adsorbing on the surface. It assumes that all sites on the surface are energetically homogeneous and that the heats of adsorption for all layers, except the first, are the same.

The BET equation for adsorption is as follows [185]:

$$\frac{P/P_0}{V\,(1-P/P_0)} = \frac{1}{C\,V_m} + \frac{C-1}{C\,V_m}\,(P/P_0) \qquad (2.16)$$

where constant C is obtained from a plot of the data. According to eq.2.16 a plot of $(P/P_0)/[V\,(1-P/P_0)$ versus P/P_0, results in a straight line with slope $(C-1)/(C\,V_m)$ and intercept $1/(C\,V_m)$. Brunaueret al. [186] considered the model to be applicable in the relative pressure interval of 0.05-0.35. The volume of the monolayer, V_m and the constant C are thus determined from the slope and intercept corresponding to that interval.

However, subjecting to the probing gas molecular kinetic diameter (0.36 nm) and instrument precision constraints, the micropore at the size of is difficult to be captured completely by means of the BET measurement [187]. Since the CO_2 molecules are more prone to enter small pores due to a smaller kinetic diameter (0.33 nm) under a higher temperature (273 K) compared with N_2, the CO_2 adsorption has been used in the surface area measurements of activated carbons [188].

Dubinin and Radushkevich set forth an equation to estimate the micropore volume using the low and medium pressure portions of the adsorption isotherm [189]. This theory is based on the postulate that the mechanism for adsorption in micropores is that of pore filling rather than a layer-by-layer formation of a film on the walls of the pores. The DR equation is an adaptation of the earlier Polanyi potential theory of adsorption, and assumed the following form [189]:

$$log(W) = \log(W_0) - BT^2\,log^2(P_0/P) \qquad (2.17)$$

where constant B is related to the adsorbate. A plot of $log^2(P_0/P)\ vs.\ log(W)$ is a straight line with intercept $\log(W_0)$.

Chapter 3

Role of surface oxides in coal char oxidation

3.1 Introduction

The present study aims at contributing to a better atomistic characterization of the nature of oxides which form on the surface of coal chars upon oxidation, their rearrangement and desorption as carbon is heated up, according to the model proposed in ***Chapter 1*** (section 1.1.3).
The ***Chapter 3*** is organized in the following parts:

- *Thermoanalytical characterization of oxidized chars (3.3.1)*: to characterize the thermal stability of functional groups which are formed upon oxidation at different temperatures, char samples have been oxidized in thermobalance and analyzed using Temperature Programmed Desorption Technique. Results are presented and discussed.
- *Surface characterization of oxidized chars by XPS (3.3.2)*: in order to get an insight into the reactions that produce CO or CO_2, it is important to characterize the complexes formed in the oxidation step and their transformation during the process. The chemical nature of carbon-oxygen functionalities has been clarified by analysis of *C1s* and *O1s* core-level XPS Spectra acquired at high-resolution using Synchrotron radiation.
- *Assessment of the dynamics of surface oxides during alternated oxidation/desorption (Carboloop)(3.3.3):* the exact nature of surface oxides formed at low/moderate temperature, their rearrangements and desorption as carbon is heated up, are the very key points of the Carboloop Process. For this reason, an experimental campaign of XPS measures has been purposely designed to characterize the nature of surface oxides of char upon alternated cycles of oxidation and desorption.

3.2 Experimental Section

3.2.1 Material

South African coal, a medium-rank bituminous coal with a high content of inertinite macerals, was used for the current experiments. Proximate and ultimate analysis data are given in Table 3.1. The heating value of the chars is also reported, as measured by the isoperibolic calorimeter Parr 2000. Chars were prepared by pyrolyzing batches of coal for 5 min in a lab-scale fluidized bed reactor at 1123 K in nitrogen flow.

Table 3.1. Proximate and Ultimate Analysis.

Ash	**Volatiles**	**C**	**H**	**N**	**O** [a]	**LHV**
(wt%)	(wt%)	(wt%)	(wt%)	(wt%)	(wt%)	(MJ/kg)
20.4	4.6	75.0	1.2	1.8	21.6	28

3.2.2 Oxidation and Desorption treatments in Thermobalance

Char samples were ground and sieved in size range 100–150 μm and were subjected to the following set of thermoanalytical experiments: pre-oxidation treatment a 650 K ≤ T ≤970 K for times ranging from 10 to 45 minutes and Temperature Programmed Desorption (TPD) with analysis of evolved gas. Experiments were performed using NETSCH 409 CD apparatus connected with a NDIR CO and CO_2 analyser (ABBAO2020 Uras 14). About 20 mg of char was used in each test. In the pre-oxidation step the sample was heated to T_{ox} at the heating rate of 20 K/min in a flow of high purity nitrogen (250 mL/min) and held at this temperature for 5 min before switch in a flow of synthetic air (250 mL/min) for a time t_{ox}, subsequently the sample was cooled to 473 K in nitrogen at the heating rate of 20 K/min. After the cooling step, the TPD experiment was performed heating the sample up to 1573 K in nitrogen at the heating rate of 20 K/min and was held at temperature for 40 min. TPD gas evolution was worked out to obtain the CO-CO_2 released as a function of time/temperature. The mass recorded during TPD experiments was worked out in order to obtain DTG plots of ($dw/dt\ w_0^{-1}$) vs. t, where w, w_0 are the actual and the initial weight of sample (after the pre-oxidation stage). The amount of CO and CO_2 released has been normalized for $w_{0.}$

3.2.3 Samples preparation for XPS

South African char was used for the current experiments (Table 3.1). Samples analyzed were in the form of slabs with dimensions of approximately 6 × 6 mm^2 and thickness of 1 mm. Oxidation treatments were performed by heating up in electric oven under a flux of air to the temperatures 723 K ≤ T_{ox} ≤ 1073 K. The treatments were carried out for t_{ox} ranging from 1 to 120 min. For comparison, isothermal combustion tests were carried out on the samples, in form of powder in the size range 100–150 μm, at the same combustion temperature T_{ox}. In this case, the sample was loaded in the TGA and heated up to T_{ox} in a flow of nitrogen at the heating rate of 20 K/min. Once the present temperature was approached, the gas was switched over from nitrogen to air and the sample was held at T_{ox} for time t_{ox}. This procedure allows to estimate the carbon burnoff level.

3.2.4 Spectra acquisition of oxidized char samples

The XPS experiments were performed in the ultra high vacuum chamber (UHV) (base pressure 8 × 10^{-11} mbar) of the SuperESCA beamline at the Elettra synchrotron radiation facility (Trieste, Italy). Details about the parameters of the Elettra storage ring and a technical description of the SuperESCA beamline are provided in *Appendix I.*

Samples in the form of slab were deposited as thin film on circular adhesive foils of about 6 mm of diameter. The sample on a circular adhesive foil was carefully fixed to a Ta frame with a 6 × 6 mm^2 front side window to expose the sample surface. An Au foil with dimensions of approximately 3 × 6 mm^2 was placed in good electrical contact with the sample. Au was used as a reference to calibrate the binding energy position. The sample holder was loaded in the main chamber and alignment of the sample surface with the X-ray beam and analyser was done externally by means of a manual manipulator.

Electrons were collected at an angle of 20° with respect to the surface normal by a Phoibo analyzer (SPECS GmbH) equipped with a home-made detector. The measurements were performed with the beam impinging at an angle of 37° with respect to the normal to the sample surface. The spot of the X-ray beam on the sample surface had a diameter of about 200 μm.

Survey spectra acquisition were recorded at photon energies 650 eV to verify the alignment and investigate possible interferences arising from inorganic matter and contaminants. The photon energy was selected to include in the survey spectrum both *O1s* and *C1s* peaks. During acquisition of the spectra it was carefully checked that no binding energy shift due to charging effects occurred.

C1s and *O1s* core level spectra were measured at photon energies of 400 and 650 eV, with energy resolutions of 80 and 150 meV, respectively. The binding energy range was 350-0 eV and 550-0 eV. For each spectrum the binding energy position was calibrated by measuring the Fermi level position of the Au reference sample.

3.2.5 CLC samples preparation

The validity of the Carboloop concept has been checked by means of discontinuous experiments in which periodic exposure of carbon samples to oxidation and desorption conditions, similar to that experienced by fuel particles in looping combustion, has been accomplished in a fluidized bed micro reactor. South African char was used for the current experiments (Table 3.1) Approximately 2 g of a sample, in the form of a powder in size range 100–150 μm, was placed in a cylindrical stainless steel reactor heated up externally by an electric oven. Tests consisted of sequential oxidation/desorption steps carried out as follows:

Step 1: 1° Oxidation Cycle. The sample was initially loaded into reactor and heated in a flow of air (300 mL/min) up to T_{ox} = 573 K at the heating rate of 20 K/min. The sample was then kept in the flow of air for a time t_{ox} = 30 min. The sample was cooled in nitrogen and collected at 298 K.

Step 2: 1° Desorption. The sample was re-loaded into the reactor and heated in a flow of oxygen-free stream (pure CO_2) (300 mL/min). The temperature was stepwise raised to the desorption temperature T_{des} = 973 K at the heating rate of 20 °C/min. The sample was held at T_{des} for a time t_{des} = 15 min before the temperature was again stepwise decreased in a flow of pure CO_2. The sample was collected at 298 K. Step 1 and 2 were then iterated three times.

3.2.6 Spectra acquisition of CLC char samples

The XPS experiments were performed in the ultra high vacuum chamber (UHV) (base pressure 8×10^{-11} mbar) of the SuperESCA beamline at the Elettra synchrotron radiation facility (Trieste, Italy). Samples in the form of powder were deposited as thin film on circular adhesive foils of about 6 mm of diameter. Spectra acquisition was performed following the procedure reported in section 3.2.4.

3.3 Results and Discussions

3.3.1. Thermoanalytical characterization of oxidized chars

In order to get an insight into the reactions that produce CO or CO_2, it is important to characterize the thermal stability of the complexes formed in the oxidation step and their transformation during the process [30]. In this section, to highlight the influence of oxidation temperature on the nature of functional groups, char samples have been oxidized in thermobalance at different temperatures, and analyzed using Temperature Programmed Desorption Technique. Results are presented and discussed.

The weight loss of the sample and the release of CO and CO_2 were continuously monitored throughout thermoanalytical experiments. Fig.3.1 shows the DTG plots obtained over Temperature Programmed Desorption experiments of char samples upon pre-oxidation at different temperatures. To better visualize and interpret the evolution of the carbon-oxygen functionalities during the desorption process, oxidized samples have been compared with the raw samples and divided in two groups according to pre-oxidation temperature.

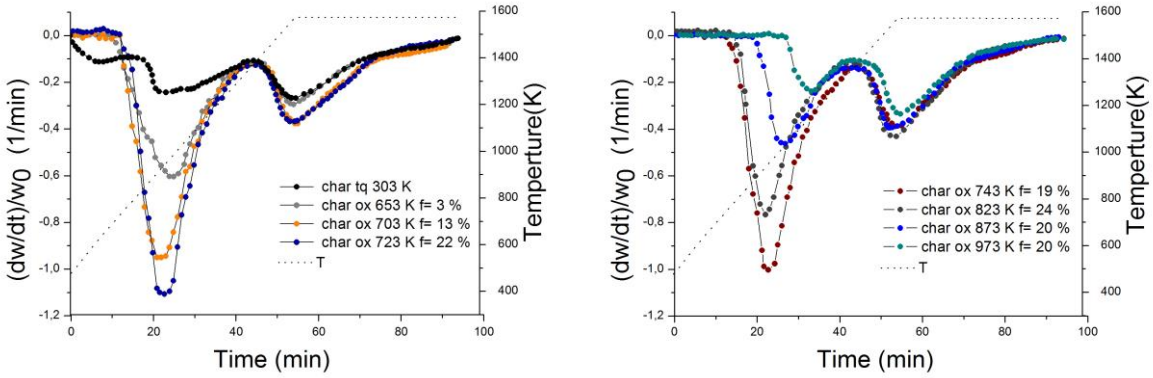

Fig.3.1. DTG plots obtained over TPD experiments of oxidized char samples at different temperatures**.** The carbon burnoff level *%f*, obtained in the pre-oxidation step prior to TPD, is also reported.

Comparison at first glance suggests that pre-oxidation affected the DTG curves obtained during the TPD. In Table 3.2 are reported carbon burnoff level (*%f)* obtained in the pre-oxidation step prior to TPD. The Table 3.2 reports also data recorded during the TPD measurements, in particular: the weight loss during the Non Isothermal step ($\Delta w_{TPD\ NI}$), during Isothermal step ($\Delta w_{TPD\ Iso}$), the total weight loss ($\Delta w_{TPD\ tot}$), and the DTG peak temperatures (T_{max}) of the TPD.

Table 3.2. Carbon burnoff level obtained in the pre-oxidation step prior to TPD, the weight loss obtained in the TPD steps, and DTG peak temperatures of the TPD.

T_{ox}(K)	303	653	703	723	743	823	873	973
%f	0	3	13	22	19	24	20	20
$\Delta w_{TPD\ NI}$	5.9	10.3	14.7	15.5	13.5	9.4	5.7	1.7
$\Delta w_{TPD\ Iso}$	7.3	7.4	9.6	10.4	10.5	12.1	10.2	8.3
$\Delta w_{TPD\ tot}$	13.2	17.7	24.3	25.9	24.0	21.5	15.9	10
T_{max}	673 973 1550	973 1550	973 1550	973 1550	973 1550	973 1550	973 1550	973 1550

The Temperature Programmed Desorption technique enables to determine the energetic distribution of a variety of surface oxygen complexes formed in gasification and has often been used to relate such distribution or the amount of the unstable complexes to the gasification reactivity of carbons. [38].

The profiles of CO, the main gaseous product of the desorption, and of CO_2 are reported in Fig.3.2 and they closely reflect the DTG curves.

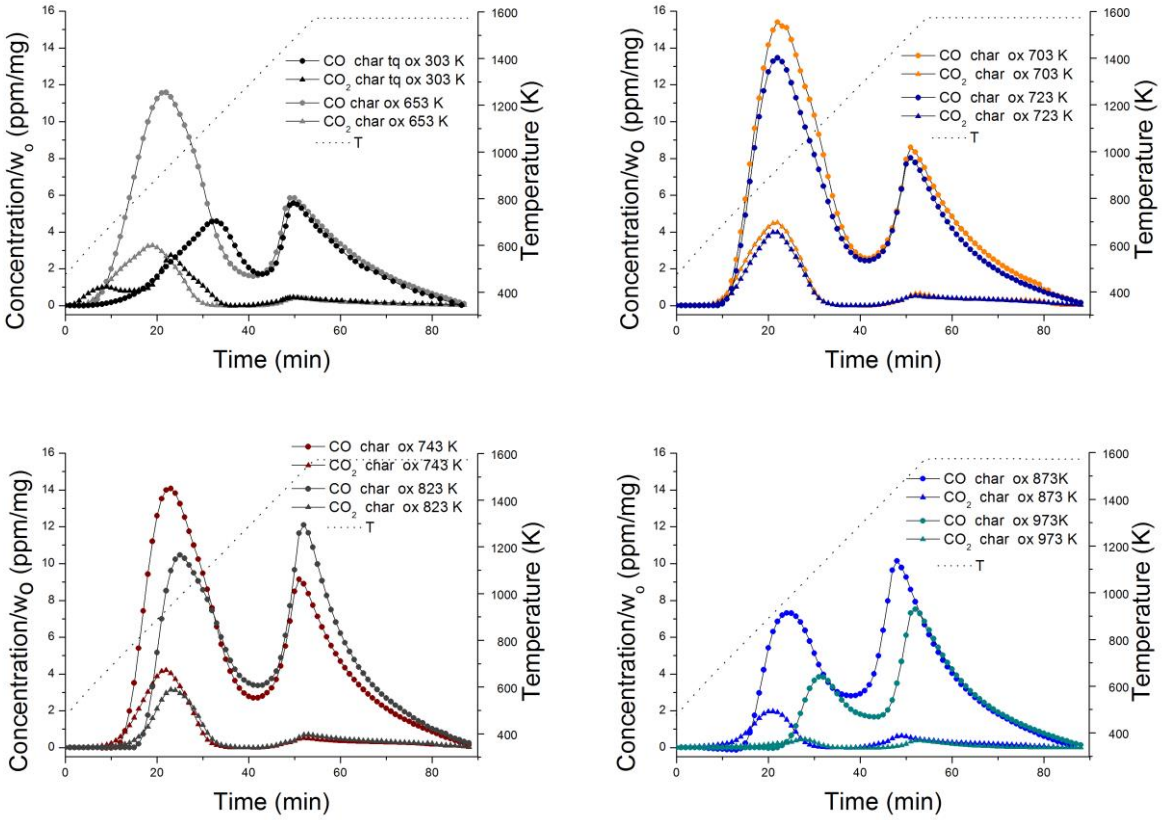

Fig.3.2. Gas evolution of the TPD tests of the oxidized char samples at different temperatures.

Gas analysis of the raw samples shows the CO_2 release starts above 470 K with a marked peak at 973 K. A modest shoulder is observed at 673 K. The release of CO starts at 673 K with a marked peak at 1073 K. A late release of CO and CO_2 occurs around 1500 K.

Pre-oxidation of samples results in a pronounced change in both gas profiles.

Upon pre-oxidation at 653 K, CO and CO_2 profiles result in a much more pronounced gas releases around 973 and 873 K respectively, and a smaller release at 1550 K. CO and CO_2 release starts above 673 K. CO and CO_2 profiles at 1550 K do not show any changes.

Pre-oxidation at 703 K $\leq$ T $\leq$ 823 K results in an increase of the CO and CO_2 concentration during TPD, which, however, keep the same shape as the sample oxidized at 653 K, while remarkable changes are observed after oxidation at 873-973 K.

Pre-oxidation at higher temperatures deeply affected both CO and CO_2 evolution with noticeable reduction of desorbed gas peaked up at 1023 and 973 K, respectively. CO release starts at higher temperature, 773 K and 873 K for char oxidized at 873 K and 973 K, respectively, while CO_2 release starts above 470 K. This peak may be explained as the effect of the abrupt ether consumption catalysed by the presence of vicinal epoxides [27,28]. Moreover, the release of CO and CO_2 at higher temperature occurs at 1450 K for the sample oxidized at 873 K.

The maximum temperatures (T_{max}) corresponding to the peaks of CO are reported in Table 3.3 together with the amount (mg) of gas released during Non Isothermal step (CO_{NI}) and Isothermal step (CO_{Iso}). The same data for CO_2 are reported is Table 3.4.

Table 3.3. Amount of CO released during Non Isothermal and Isothermal step, peak temperatures of CO evolution of char samples in TPD, as a function of the pre-oxidation temperatures.

T_{ox}(K)	303	653	703	723	743	823	873	973
$w\ CO_{NI}$	3.0	7.6	10.5	11.1	9.7	6.9	4.2	1.4
$w\ CO_{Iso}$	6.2	6.3	7.8	8.9	8.2	9.9	8.2	6.2
T_{max}	1073	973	973	973	973	1023	1023	1023
	1500	1500	1500	1500	1550	1550	1450	1550

Table 3.4. Amount of CO_2 released during Non Isothermal and Isothermal step, peak temperatures of CO_2 evolution of char samples in TPD, as a function of the pre-oxidation temperatures.

T_{ox}(K)	303	653	703	723	743	823	873	973
$w\ CO_{2\ NI}$	2.8	3.1	4.0	4.3	3.6	2.4	1.5	0.3
$w\ CO_{2\ Iso}$	0.9	0.9	0.9	1.1	0.9	1.0	0.8	0.6
T_{max}	673-973	873	873	923	923	973	973	973
	1500	1500	1500	1500	1550	1550	1450	1550

Table 3.5 reports the sum of CO and CO_2 released during Non Isothermal step ($w\ CO_{NI} + CO_{2\ NI}$), Isothermal step ($w\ CO_{Iso} + CO_{2\ Iso}$) and total gas ($w\ CO_{tot} + CO_{2\ tot}$) during TPD experiments of char samples upon pre-oxidation at different temperatures. Data are compared with the total weight loss ($\Delta w_{TPD\ tot}$) and are in agreement according the maximum error of 15 %.

Table 3.5. Gas released and total weight loss of char samples in TPD, as a function of the pre-oxidation temperatures.

T_{ox}(K)	303	653	703	723	743	823	873	973
$w\ CO_{NI} + CO_{2\ NI}$	5.8	10.7	14.5	15.4	13.3	9.3	5.7	1.7
$w\ CO_{iso} + CO_{2\ iso}$	7.1	7.2	8.7	10.0	9.3	10.9	9	6.8
$w\ CO_{tot} + CO_{2\ tot}$	12.9	17.9	23.2	25.4	22.6	19.3	14.7	8.5
$\Delta w_{TPD\ tot}$	13.2	17.7	24.3	25.9	24.0	21.5	15.9	10

When exposure to oxygen is performed above 700 K the amount of surface oxides responsible of the desorption of CO-CO_2 at 873-973 K increase. Moreover, a most noticeable change concerns the loss of functional groups desorbed as CO_2 at low temperature 470 K. When at higher temperatures, oxidation takes place (873-973 K), gas analysis suggests that abstraction of these labile surface complexes has already happened during the oxidation step due to the high temperature. However, these oxidation conditions leave on the carbon surface a little amount of labile functional groups that start to be released as CO_2 already at 470 K.

To highlight the influence of pre-oxidation temperature on the nature of functional groups, Fig.3.3 reports the amount of gas released $(w\ CO_{tot} + CO_{2\ tot})/w_0$ as function of pre-oxidation temperature. Notably the value of carbon conversion reached on the pre-oxidation step is also reported. The plot shows a progressive increase of surface oxide complexes in chars oxidatized up to 700 K and increasing value of *%f* up to 20. In the experiments at higher oxidation temperature roughly same carbon burnoff level was reached but the percentage of total gas released decreases.

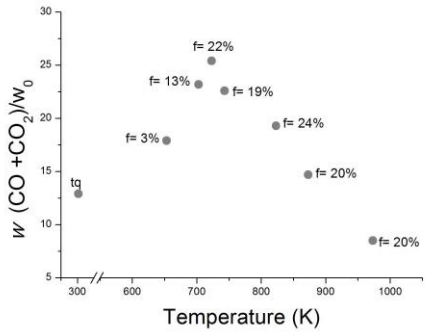

Fig.3.3 Amount of gas released $(w\ CO_{tot} + CO_{2\ tot})/w_0$ in TPD as function of pre-oxidation temperature of char samples. The carbon burnoff level *%f*, obtained in the oxidation step prior to TPD, is also reported.

The decrease of formation of carbon oxides upon oxidation has been observed by Wang et al. [15] in the study of the early stages of oxidation al low temperature, which was ascribed to "unreactive" oxygenated complexes being formed during oxidation and permanently deactivating the reaction sites for further oxygen adsorption. As results, they found that a period of oxidation eventually results in a reduction in the concentration of species responsible for the production of $CO\text{-}CO_2$ [15].
The deactivation of sites active towards oxygen adsorption at mild temperature as a consequence of the accumulation of stable oxygenated functionalities has been also postulated by Salatino et al. [13].

When an oxidized coal char is subjected to a heating program temperature ramp, the surface oxides desorb primarily as the oxides of carbon, CO and CO_2 [38].
Montoya at al. [54], investigated the "effect of neighbouring" surface oxygen groups *C(O)* on the desorption of the CO molecule from the carbonyl model using DTF Theory. They found that the presence of the neighbouring surface oxygen group decreases the CO desorption energy. It has been shown that the presence of an epoxy group near an oxidized carbon surface debilitates the edge adjacent to the epoxy group facilitating the gasification of the graphene layers in the form of CO [54].
In the key of "neighbouring effect" TPD results suggest that the increasing $w\ CO\text{-}CO_{2\ NI}$ upon oxidation at moderate temperature could be related to high concentration carbonyl/epoxy on carbon surface.
Release of CO/CO_2 below 1000 K was also observed in a study on reduced graphene oxide when hydroxyl and epoxy sites were in close proximity by [54].
The role of epoxy interaction with surface oxides has been pointed out also by Larciprete at al. [27,28]. They found that ether-epoxy pairs attract the diffusing epoxides and convert in lactone-ether pairs promoting the desorption of $CO\text{-}CO_2$.
When oxidation at higher temperature takes place (873-973 K), abstraction of these labile functional groups has already happened during the pre-oxidation step. However, the peak of CO at 1023 K could be related to neighbouring carbonyl/carbonyl groups or carbonyl/semiquinone groups as proposed by Montoya at al. who found that also these interactions lower, in a lesser way, the desorption energy of CO [55].
Gas evolution at high desorption temperature (around 1500 K in this study) could be related to stable oxides or to the presence of epoxy group in close proximity to other sp^3 carbon bonds [29].

It is well established (and confirmed in the present study) that CO/CO_2 ratio increases as the desorption temperature is increased according to the Boudouard reaction:

$$2CO_{(g)} \leftrightarrow C_f + CO_{2(g)} \quad (3.1)$$

On the other hand, CO_2 evolution at low temperature, could be also related to secondary interaction according to eq.3.2. giving rise to a consistent $CO\text{-}CO_2$ shift, more efficiently than the homogeneous CO disproportionation of the Boudouard reaction [53].

Interaction phenomena could occur within the char structure during the TPD process. These phenomena could be attributed to eq.3.2 [37]:

$$CO_{(g)} + C(O) \leftrightarrow C_f + CO_{2(g)} \quad (3.2)$$

were: $CO_{(g)}$ represents "free" gaseous, CO_2 resulting from the desorption of a surface oxygen complex; C(O) is a surface oxygen complex; and C_f is an unoccupied surface-active site.

It has been shown that*:*

- secondary CO_2 evolution appears as a reflection or satellite peak under primary CO desorption features [37].

As pointed by Hall and Calo [37], thermally stable C(O) complexes do not participate in secondary reactions at temperatures significantly below their desorption temperature. This means that, at the temperatures required to activate (i.e., thermally decompose) the surface complexes, the forward step of eq.3.2 (ie., CO_2 formation) is favoured [37]. At high temperature, the reverse Boudouard reaction (the reverse step of eq.3.1) takes place, favouring the high CO/CO_2 ratio.

Recently, Montoya at al. studied the adsorption of CO on unsaturated edges of carbonaceous materials and elucidated pathways for CO_2 desorption. They found possible and energetically feasible desorption CO_2 pathways after CO adsorption. In particular, they underlined the role of the epoxy in the adsorption of CO leading to the formation of a carbonate group at the edge of the graphene layer with an exothermicity of 35.6 kcal/mol [55].

The degree to which secondary interactions affects resultant TPD spectra seems to be a complex function of the carbon pore structure (most probably in micropores) [37]. For instance, if a CO molecule is released in a narrow pore of char from any surface complex, it is possible that the CO molecule can interact with surface oxygen complexes favouring the CO_2 desorption [55].

Secondary interactions, as well as Boudouard reaction, could explain the lower CO/CO_2 ratio in the first ramp of the TPD experiments, while at high temperature, the reverse Boudouard reaction takes place, favouring the higher CO/CO_2 ratio.

3.3.2. Surface characterization of oxidized chars by XPS

Temperature programmed desorption experiments are supported by X-ray photoelectron spectroscopy (XPS) of oxidized char samples in order to highlight the distribution of functional groups formed upon oxidation at different temperatures. Analysis of the spectra deconvolution provides significant clues on the extension of the oxygen uptake on the carbon surface and the evolution of the carbon-oxygen functionalities upon oxidation. The *C1s* and *O1s* high-resolution photoemission spectra oxidized South African char samples recorded at room-temperature are reported below. To avoid the contribution of metal oxides [i.e. (2p) Al ≈ 74 eV, (2p) Si ≈ 103 eV, and ($2p^{3/2}$), Ca ≈ 347 eV] scan spectra have been analyzed and are reported in Fig.3.4.

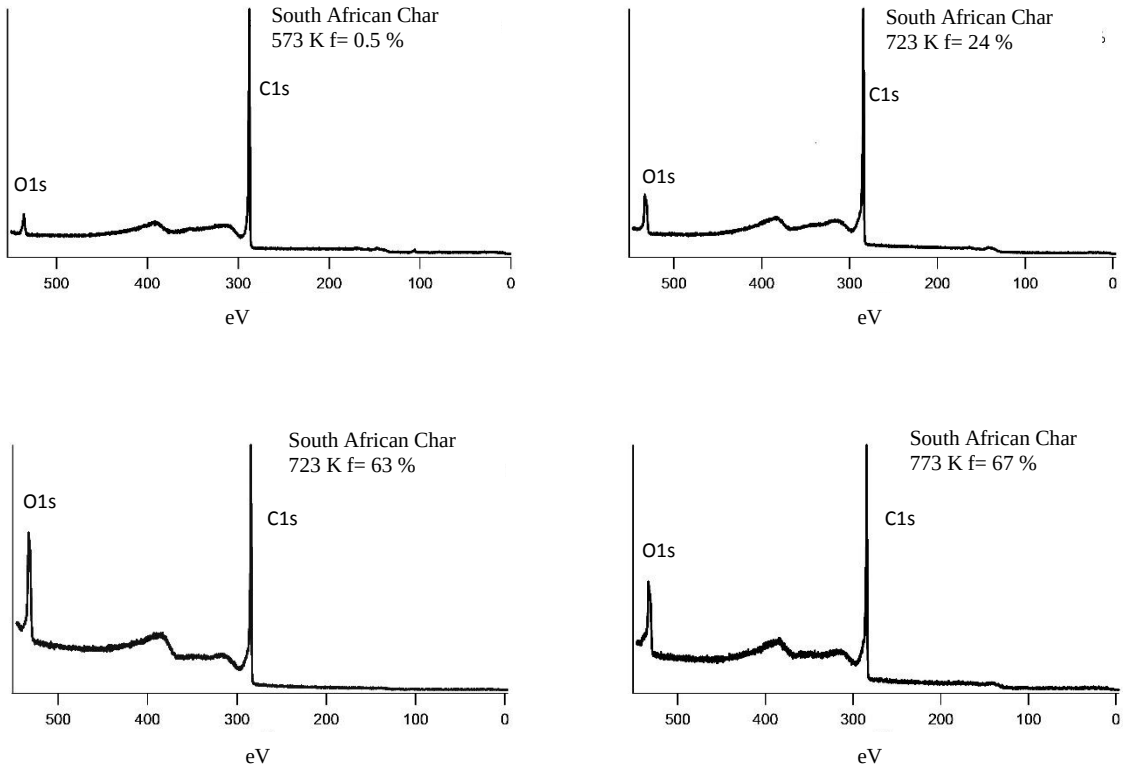

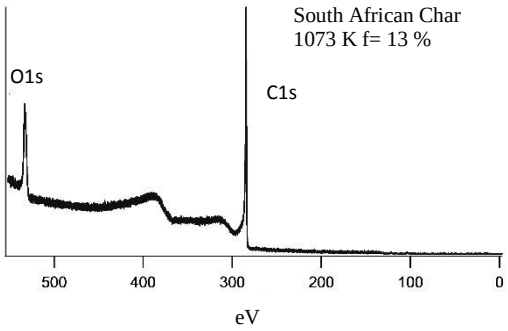

Fig.3.4. Scan spectra of oxidized char samples at different temperatures**.** The carbon burnoff level *%f* is also reported.

Scan spectra of the char samples do not show the XPS peaks of Al (74eV), Si (103eV) and Ca (347eV). This allows to exclude the contribution of metal oxides to the *O1s* peak.

To separate the contribution to the intensity of the inelastically scattered electrons and make a comparison of the individual spectra possible, the Shirley background [190] was removed from each of them. Background subtraction was performed with the software *IGOR Pro* version 6.12A. In Fig.3.5 are reported *C1s* and *O1s* spectra of oxidized samples. The *C1s* curve clearly shows a main component located at about 284.5 eV. This main peak represents sp^2 carbons in C=C bonds in aromatic domains of unoxidized carbon rings and in aliphatic chains [27,28,135,142]. Instead, other components due to sp^3 and oxidized carbons are identified on the high binding energy side: at 288.2 eV related to HO-C=O, at 286.2 eV related to epoxides and C-OH, at 285 eV related to C sp^3 and C-C(O) and finally at 283.7 related to carbon vacancies. The *O1s* curve shows three components: the main component at 532.2 is associated with electrons photoemitted from epoxy oxygen. The component on the high binding energy side (533.4 eV) is assigned to ether and hydroxyl groups, and the component on the low energy side (530.8 eV) is assigned to carbonyl, carboxyl and lactone groups. Finally, the components on the high binding energies are assigned to H_2O probably derived from desorption in the pore structure of hydroxyl groups. Bagri et al. found that hydroxyls were not detected in the infrared spectra at temperatures above 773 K and desorbed as H_2O [29].

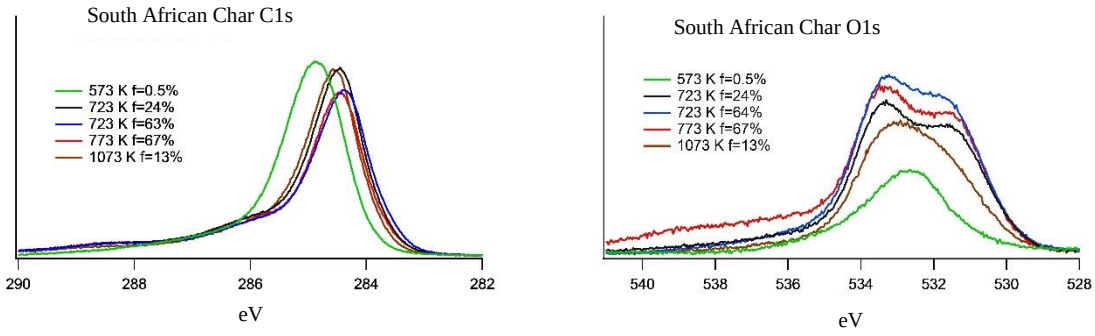

Fig.3.5. *O1s* and *C1s* XPS spectra of oxidized char samples at different temperatures. The carbon burnoff level *%f* is also reported.

For all the set of the *C1s* spectra of the oxidized samples at temperature above 573 K, the whole spectrum seems to be slightly shifted towards lower binding energies. Moreover, a sharp decrease of the peak at around 285 eV in the region related to C sp^3 is observable. After oxidative treatment at 723 K ≤ T ≤ 773 K clearly distinguishable peaks appear at around 288.4 and 286.2 eV, obviously due to the increasing formation of carbon-oxygen species. The *O1s* spectrum of the char sample oxidized at 573 K consist of a very broad peak centred at about 532.2 eV with a shoulder on the high binding energy side. Oxidation deeply affects the shape the *O1s* curves. For the sample oxidized at temperature above 573 K a sharp rise in intensity is evident. After oxidative treatments at 723 K ≤ T ≤ 773 K the peak on the high and the peak on the low binding energy side increases. After oxidative treatment at 1073 K the whole spectrum seems to be slightly shifted towards higher binding energies.

Spectra were fitted, after background removal, with Doniach−Sunjic function convoluted with Gaussians. The use of Doniach−Sunjic function allows to take into account the lineshape intrinsic asymmetric nature deriving from the screening effects of the delocalized π electrons on the final state hole potential [149]. Band assignment is based on the calculated values of binding energies as obtained from the theoretical works of Zhang et al. [142] and Barinov et al. [135] following the procedure used in [144,145]. In this context, Table 2.3 (*Chapter 2*) should be taken as a reference. Analysis of the spectra deconvolution provides significant clues on the extension of the oxygen uptake on the carbon surface and the evolution of the carbon-oxygen functionalities upon oxidation.

The fitting parameters include, for each peak, the FWHM and singularity index α of the Lorentzian component, the width of the Gaussian component, the binding energy and a dimensionless factor determining the actual intensity of the peak. Because of the large number of free fitting parameters, curve fitting was performed in two steps. In the first step, the binding energies were fixed at the values

taken from the reference works [144,145]. The parameters determining the shape of the peaks were thus determined. For a matter of simplicity, to each peak the values of Lorentzian FWHM was assigned, and α was determined for the sp^2 component in the spectrum of the raw sample taken from the reference works [144,145]. This is valid in the approximation that the lifetime of the final state and the screening of the π electrons do not change very much with the chemical environment. In the second fit, the parameters of FWHM and α were fixed and the binding energies and intensities of the peaks were optimized. As the best results of curve fitting those approximations which gave the smallest value of the root-mean-squared-error (RMSE) were accepted. Curve fitting was performed with the software *IGOR Pro* version 6.12A. The program uses the Levenberg–Marquardt non-linear least squares fitting algorithm [191], which minimizes the sum of the squares of the deviations using a linear approximation of the model to be fitted to the data. The binding energies, intensities and lineshape parameters of the components resulting from the non-linear fitting are given in *Appendix I.*

The following graphs in Fig.3.6 show the decomposition of the *C1s* and *O1s* spectra previously reported. Each component is given a different colour. Peak assignment is indicated in the legend. In each case the black dots and the red lines reproduce the experimental and the best-fit curves, respectively. The Shirley background was added to each spectrum.

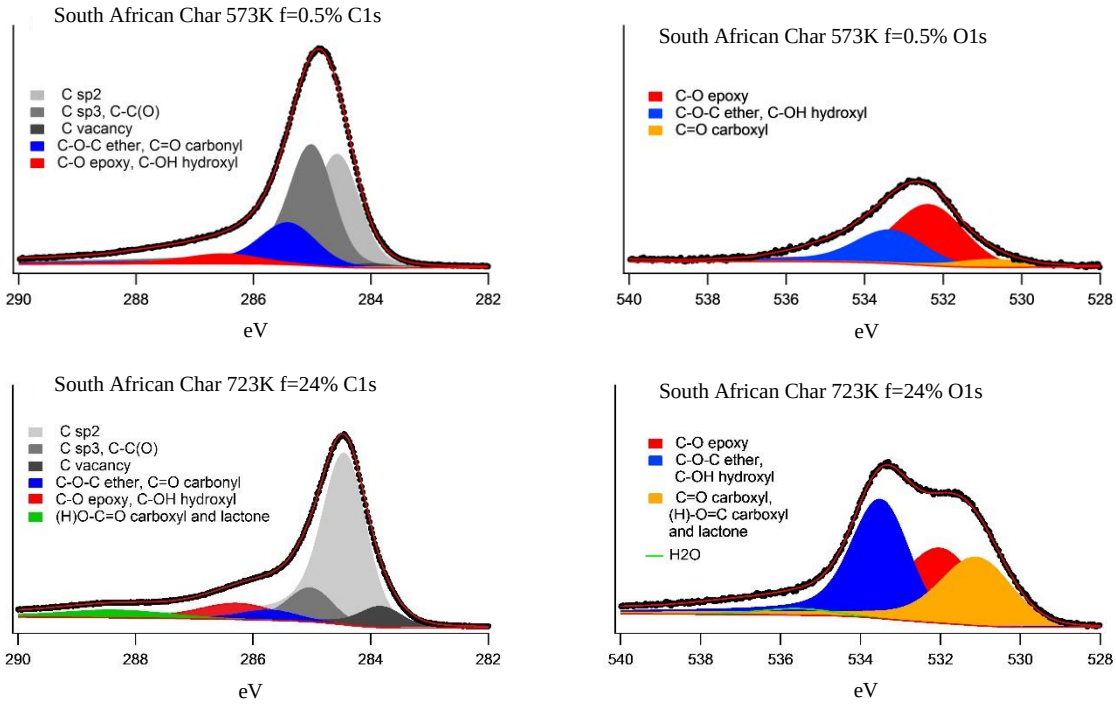

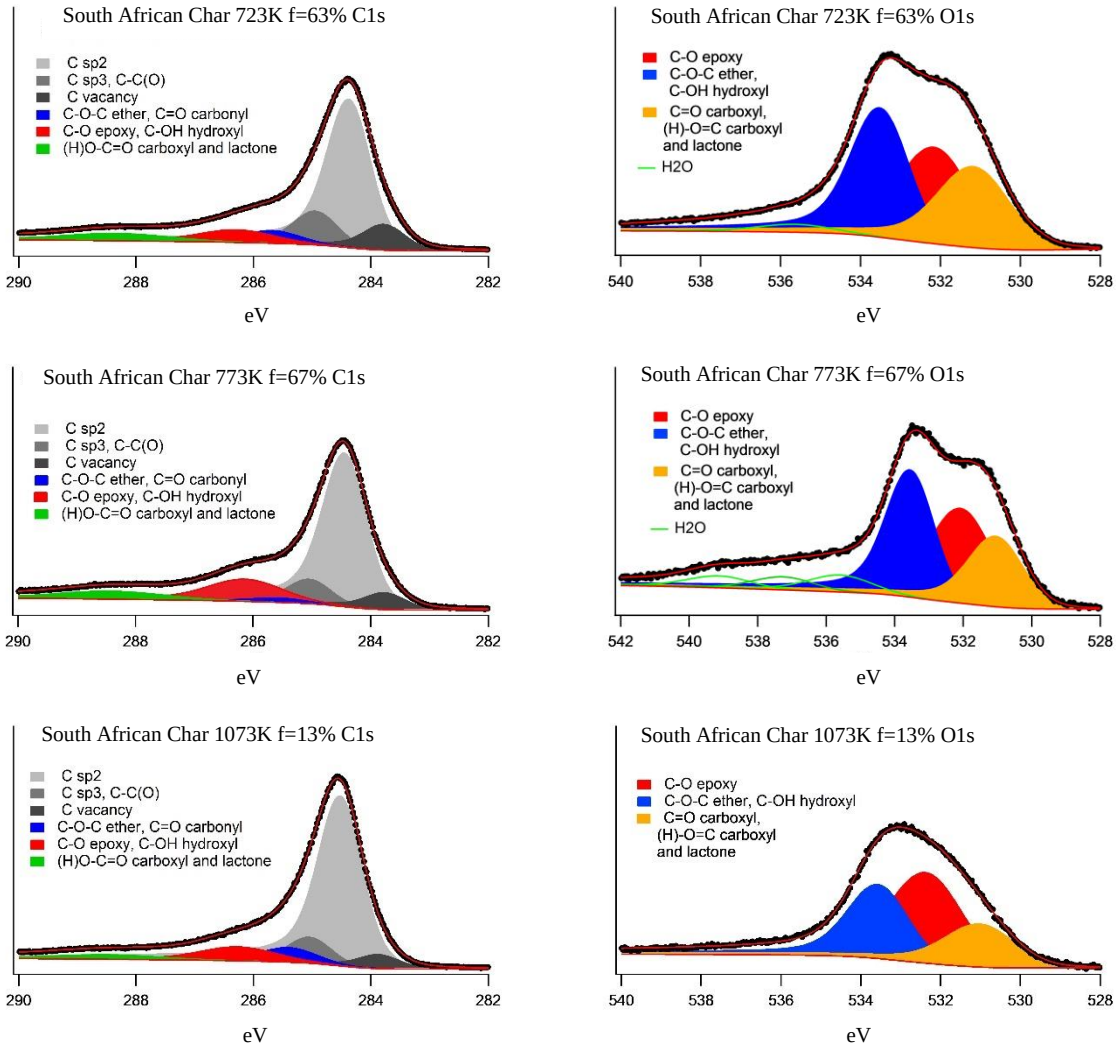

Fig.3.6. *O1s* and *C1s* XPS spectra of oxidized char samples at different temperatures. Spectral components obtained by deconvolution are shown, Peak assignment is indicated in the legend, Black dots and red lines refer to experimental and best-fit curves, respectively. The shirley background was added to each spectrum. The carbon burnoff level *%f* is also reported.

The intensity of the XPS peak (I_x) is proportional to the concentration of a given element (C_x) according to eq.2.2 *(Chapter 2)* [130]. XPS qualitative analysis was carried out to better visualize and interpret the evolution of the carbon-oxygen functionalities during the oxidation process. For *C1s* spectra the relative (%) intensity of each component was calculated according to eq.3.3. For the *O1s* spectra the relative (%) intensity of each component was calculated according to eq.3.4. This procedure allows to take into account the different oxidation degrees.

$$\%Intensity\ C_i = \frac{Area_{Ci}}{\sum_i Area_{Ci}}. 100 \quad (3.3)$$

$$\%Intensity\ O_i * = \frac{Area_{o_i}}{\sum_i Area_{o_i}} . \left(\frac{\sum_i Area_{o_i}}{\sum_i Area_{Ci}}\right) .100 \quad (3.3)$$

$$\%\ Area\ O_{tot}/C_{tot} = \frac{\sum_i Area_{o_i}}{\sum_i Area_{C_i}} .100 \cong \frac{[O]}{[C]} \quad (3.4)$$

Total intensity of *C1s* and *O1s* spectra and their ratio are reported in Table 3.6. The intensities of the components resulting from the non-linear fitting are given in *Appendix I.*

Table 3.6. Total intensity of *C1s* and *O1s* spectra and their ratio *%Area* O_{tot}/C_{tot}. The carbon burnoff level *%f* is also reported.

T (K)	***time (min)***	***f %***	***C 1s*** $_{area}$ ***(a.u.)***	***O 1s*** $_{area}$ ***(a.u.)***	***%Area*** O_{tot}/C_{tot}
573	30	0.5	5599	1360	24
723	30	24	5570	3337	61
723	120	63	5259	3861	72
773	60	67	5154	3624	71
1073	1	13	5321	2679	50

Fig.3.7 reports the ratio *%Area* O_{tot}/C_{tot}, calculated according eq.3.4, as function of temperature/carbon burnoff level. The plot shows a progressive increase of the amount of oxide complexes with temperature of oxidation up to $T_{ox} \approx 700$ K and $\%f \approx 20$. In this range of temperature, the amount of oxide complexes seems to increase by extent of conversion. For higher oxidation temperature, of the percentage of surface functional groups decreases. Data are in agreement with previous results shown in Fig.3.3.

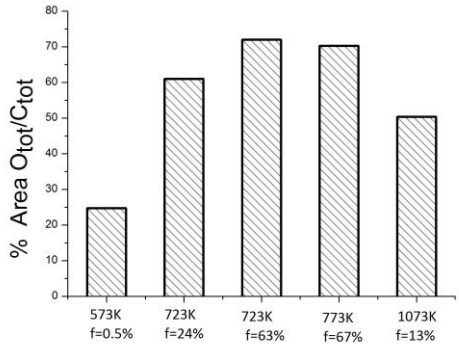

Fig.3.7.*%Area O_{tot}/C_{tot}* of oxidized char samples at different temperatures**.** The carbon burnoff level *%f* is also reported.

The following bar graph histograms report the calculated relative intensities of the components of the *C1s* and *O1s* spectra of oxidized samples (Fig. 3.8):

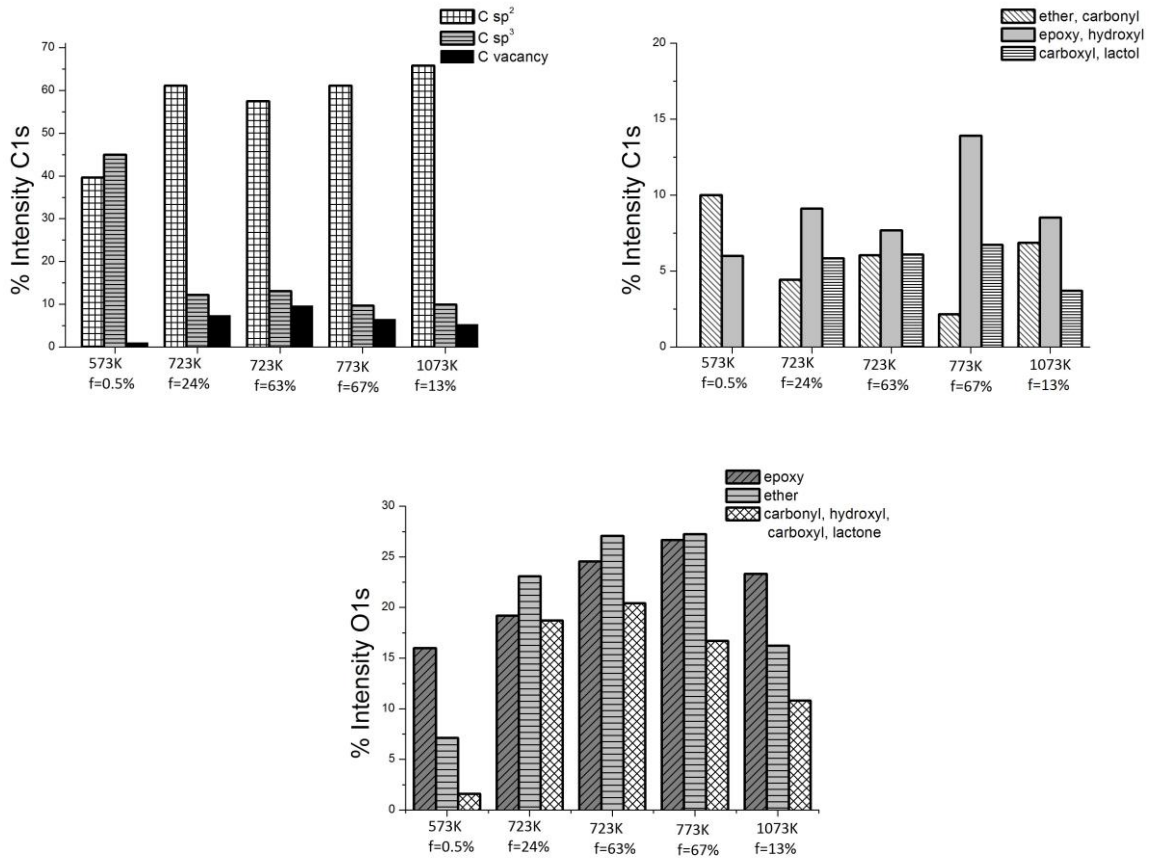

Fig.3.8 Intensities of the components of the *C1s* and *O1s* spectra of the different samples. The carbon burnoff level *%f* is also reported.

As can be seen from the graphs relative to the *C1s* spectra reported above, upon oxidation at 573 K, 40% of carbon is in the form of C sp^2. Reasonably, these carbon atoms are mainly taking part in conjugated C=C double bonds. C sp^3 and carbon atoms linked to oxidized carbon (C-C(O)) represent 45% of the total carbon, while carbons surrounding vacancies in the aromatic planes are the 1%; finally, a contribution of 15%, to the total intensity is given by carbon atoms in carbon-oxygen groups, mainly epoxides (C-O epo), hydroxyls (C-OH), ethers (C-O-C) and carbonyls (C=O). Main component of the *O1s* spectrum, at about 532.2 eV, is due to epoxy groups; it follows that more than 15% of the oxygen present on the char surface is in the form of epoxides. The remainder oxygen forms ethers-hydroxyls (7%), and carbonyls (2%). Their components are at 533.4 and 530.8 eV respectively.

Upon oxidation at 723 K a pronounced increase in intensity of the C sp^2 component is observed, accompanied by a decrement of C sp^3 and C-C bonds in proximity of oxidized sites (C-C(O)) and of ether-carbonyl component. The carbon vacancies increase as a consequence of carbon consumption and formation of new active sites. Significant increase is shown of epoxy-hydroxyl groups. Further analysis reveals the increment of the carbon-oxygen functionalities, moreover a new component appears at 288.2 eV, which is attributed to carbon in carboxylic and lactone groups ((H)O-C=O). The carbon vacancies increase as a consequence of carbon consumption and the formation of new active sites. The *C1s* spectrum evolution can be explained by a considerable expansion of the oxidized domains, a decay of the C-C(O) bonds as they progressively transform into C−O bonds, and an increase of aromatic domains C sp^2 as result of graphitization process. The *O1s* spectrum clearly shows that extensive uptake of oxygen is taking place in this condition. The sharp rise in the intensity of the *O1s* signal is evident in the case of the sample treated in air at 723 K. An increase in the ratio of the intensity for all the species is observed [i.e. epoxy (19%), ether (23%), carbonyl (19%)]. Reasonably, rearrangement of epoxides towards ether and carbonyl groups is the predominant event taking place on the surface of this sample. However, upon extensive oxidation at 723 K, the *O1s* spectrum does not show a further extensive chemisorption of oxygen (Table 3.6). Moreover, it indicates the desorption of labile species (i.e. carbonyl) at about 530.8 eV. Surface oxides desorption is modest but still kinetically limited at 723 K.

Upon oxidation at 773 K a pronounced increase in intensity of the C sp^2 component is observed, accompanied by a more pronounced decrement of C sp^3 and C-C bonds in proximity of oxidized sites

(C-C(O)) and of ether-carbonyl component. At the same time, carbon vacancies and carbon-oxygen species increase. The most significant increase is shown by epoxy-hydroxyl followed by carboxyl and lactone groups. It has been shown that the epoxy and hydroxyl groups on graphene are energetically favourable. Hydrogen bonds play an important role in the stability of these aggregates [29]. The carbon vacancies decrease compared to the samples oxidized at 723 K, probably as a consequence of vacancies saturation due to the high extension of carbon burnoff. However, upon extensive oxidation at 773 K, the *O1s* spectrum does not show a further chemisorption of oxygen compared to extensive oxidation at 723 K (Table 3.6). In particular the peak of ethers (27%) almost equals that of epoxy component (26%) with a further decrease of the component at 530.8 eV (17%). Results suggest that structural rearrangement of epoxides towards ethers and carbonyls upon extensive oxidation promotes also the desorption of labile species. Surface oxides desorption is modest but still kinetically limited at 773 K.

Upon oxidation at 1073 K the *C1s* spectrum still shows a considerable increase in intensity of the C sp^2 main component at 284.5 eV accompanied by a more pronounced decrement of C sp^3 and C-C bonds in proximity of oxidized sites (C-C(O)) and of the ether-carbonyl component. The carbon vacancies increase as a consequence of carbon consumption and formation of new active sites. Results suggest that this component is a function of carbon burnout level. In parallel the *O1s* spectrum still reveals the existence of the main component with epoxy group as predominant species (23%), followed by ether (16%) and carbonyl (10%) component. Reasonably, due to the high temperature, desorption of labile species is the predominant event taking place on the surface of this sample.

In the key of "neighbouring effect" TPD, results suggest that the increasing $w\ CO_{NI} + CO_{2\ NI}$ upon oxidation at moderate temperature could be related to high concentration of (carbonyl-hydroxyl-/epoxy on carbon surface. Fig.3.9 shows the ratio of ether-hydroxyl (533.4 eV) /epoxy (532 eV) and carbonyl-carboxyl (530.8 eV) /epoxy (532 eV) estimated from *O1s* spectra deconvolution.

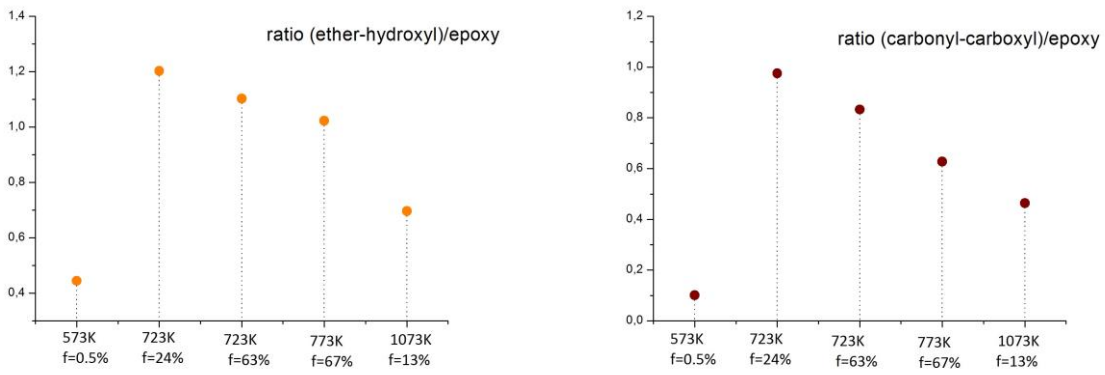

Fig.3.9. Ratio of (ether-hydroxyl)/epoxy and (carbonyl-carboxyl) /epoxy estimated from *O1s* spectra deconvolution. The carbon burnoff level *%f* is also reported.

The plot shows an increasing ratio of (ether-hydroxyl) /epoxy and (carbonyl-carboxyl) /epoxy from 573 to 723 K (reaching carbon burnoff of 24%), followed by a decrease for higher carbon burnoff and high temperature. This result confirms the high interaction between carbonyl/epoxy and ether-hydroxyl/epoxy groups upon oxidation at mild temperature and could explain the origin but also the different percentage of CO/CO_2 evolution in TPDs.

The comparison of results obtained with char samples oxidized between 500 and 1000 K, are interpreted in the frame of recent result of Senneca et al. [145]. They found that the rearrangement of epoxy during TPO experiments happened together with activation of the more stable and less reactive carbon sites. Results were in good agreement with semi-lumped kinetic models of carbon oxidation which include [145]:

$C_f^* + O_2 \xrightarrow{1} C(O)^{\#}$	$\Delta H < 0$	formation of '*metastable*' surface oxides
$C(O)^{\#} + O_2 \xrightarrow{2} C(O) + CO, CO_2$	$\Delta H < 0$	oxygen-driven complex switch-over
$C(O) \xrightarrow{4} C_f^* + CO, CO_2$	$\Delta H > 0$	desorption into CO, CO_2

In particular when oxidation is performed at low temperature, chemisorption is likely to occur extensively, but the energy barrier for the rearrangement of the early oxides towards more stable forms is not overcome. This is likely to be the case for chemisorption up to 573 K. When exposure to oxygen is performed at moderate temperature, oxidation extends beyond the chemisorption step. At moderate temperature, energy barriers for rearrangement of the native surface oxides into more

stable, possibly favoured by complex switch-over driven by molecular oxygen, may be overcome. Epoxy groups are the functionalities with the lowest thermal stability and are dominant group at the low oxidation stage (in particular: T<700 K), which could in the first instance be associated to the "metastable" oxygen complexes, while ethers, carbonyl and semiquinones form prevail as oxidation proceeds. At high temperature (T_{ox} /$T_{des} \geq$ 800 K), energy barriers for desorption into CO/CO_2 of labile surface oxides may be overcome. Experimental results underline the importance of evolution of epoxy group (by complex-switch-over driven by molecular oxygen) into more stable surface oxides (carbonyl-ether) when oxidation temperature is performed up to 700 K. In addition, results suggest that the interaction of the epoxy groups with the other surface oxides (ether, carbonyl) could promote the removal of C atoms from the C backbone as results of $CO\text{-}CO_2$ evolution. When oxidation is performed at T ≥ 800 K, the desorption of functional groups has already happened, leaving a low amount of surface oxides (mainly epoxides).

2.3.3. Assessment of the dynamics of surface oxides during alternated oxidation/desorption

The exact nature of surface oxides formed upon low/moderate temperature, their rearrangements and desorption as carbon is heated up are the very key points of a looping combustion concept developed by the Naples group under the name of Carboloop [53]. An experimental campaign of XPS measurements has been purposely designed to characterize the nature of surface oxides of char upon alternated cycles of oxidation and desorption. Cycling is performed between oxidation in air at 573 K for 30 min and desorption in CO_2 at 973 K for 15 min. Char sample oxidized in air at 573 K for 30 min (*1° Ox* in this section) has been previously compared with chars oxidized at higher temperatures. In this section, it is compared with chars exposed to iterated oxidation/desorption cycles.

The *C1s* and *O1s* high-resolution photoemission spectra oxidized South African char samples recorded at room-temperature are reported below. To avoid the contribution of metal oxides scan spectra have been analyzed and are reported in Fig.3.10.

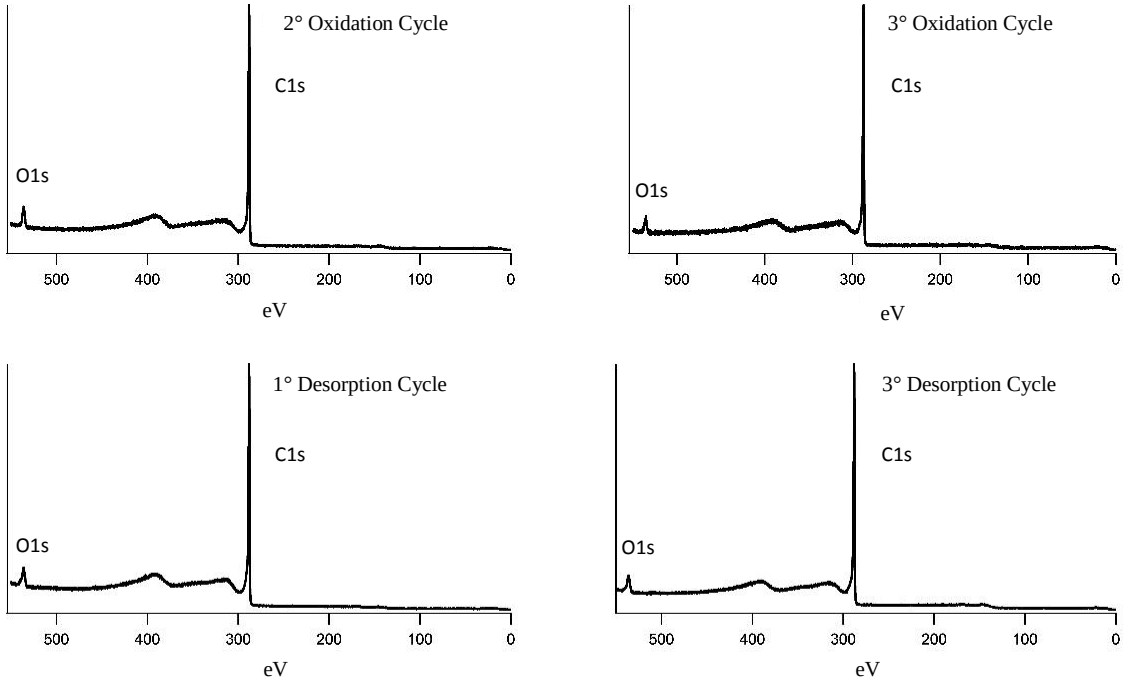

Fig.3.10. Scan spectra of oxidized char samples after oxidation/desorption cycles.

Scan spectra of the char samples do not show the XPS peaks of Al, Si, and Ca. This allows to exclude the contribution of metal oxides to the *O1s* peak.

Fig.3.11 are reported *C1s* and *O1s* spectra of oxidized char samples after oxidation/desorption cycles.

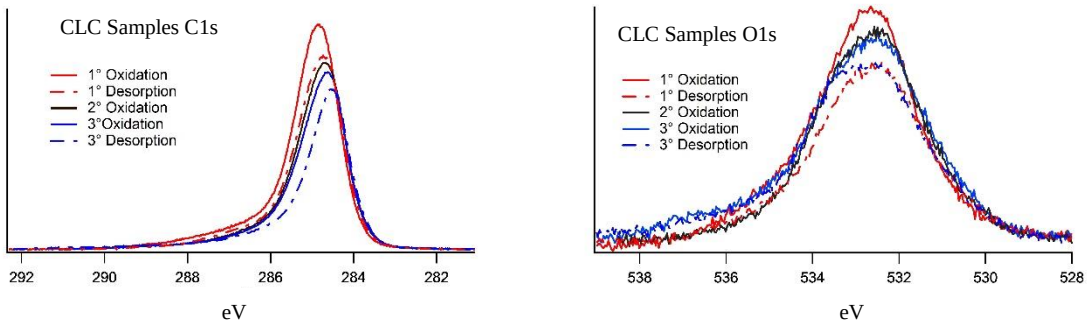

Fig.3.11. C1s and O1s spectra of oxidized char samples after oxidation/desorption cycles.

The *C1s* curves clearly show a main component located at about 284.5 eV. A progressive decrease of carbon content is observed upon iterated oxidation/desorption cycles. The *O1s* spectra consist of a very broad peak centred at about 532.2 eV. Analysis shows a tendency to uptake oxygen during the oxidation stage and a decrease of oxygen content as result of the desorption steps.

Spectra were fitted, after background removal, with Doniach−Sunjic functions convoluted with Gaussians. The following graphs show the decomposition of the *C1s* and *O1s* spectra (Fig.3.12). Each fitting component is given a different colour. Peak assignment is indicated in legend. In each case the black dots and the red lines reproduce the experimental and the best-fit curves, respectively. The Shirley background was added to each spectum.

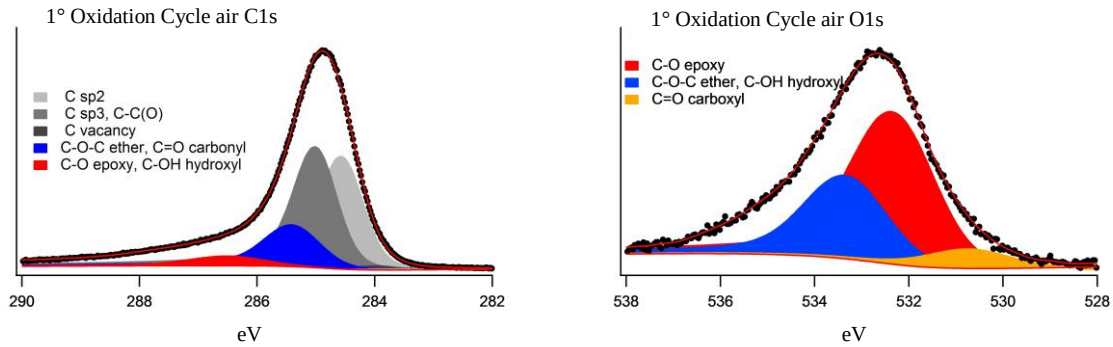

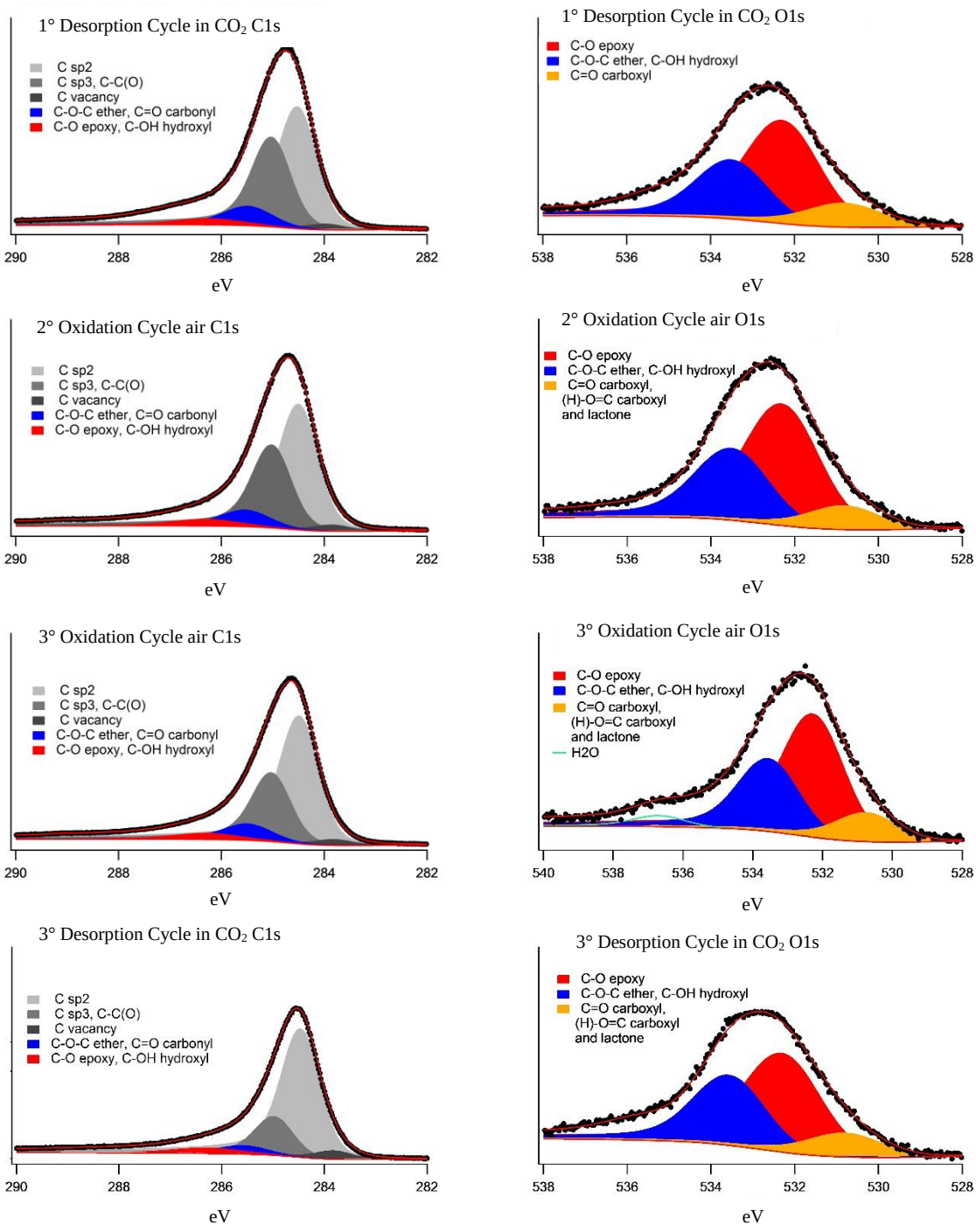

Fig.3.12. O1s and C1s XPS spectra of oxidized char samples after oxidation/desorption cycles. Spectral components obtained by deconvolution are shown. Peak assignment is indicated in the legend, Black dots and red lines refer to experimental and the best-fit curves, respectively. The shirley background was added to each spectrum.

To better visualize and interpret the evolution of the carbon-oxygen functionalities during the oxidation process, for *C1s* spectra, the relative intensity of each component and the *%Area* O_{tot}/C_{tot}, have been calculated according eq.3.3-4 reported in the previous section 3.3.2. This procedure allows to take into account the carbon burnoff level upon oxidation.

Table 3.7. Total intensity of C1s and O1s spectra and their ratio *%Area* O_{tot}/C_{tot}.

n° Cycles	***C 1s*** $_{area}$	***O 1s*** $_{area}$	***%Area*** O_{tot}/C_{tot}
1°Ox	5599	1360	24
1°Des	5374	1148	21
2°Ox	5270	1359	26
3°Ox	4922	1393	28
3° Des	4112	1045	25

Table 3.7 reports the total intensity of *C1s* and *O1s* spectra and their ratio *%Area* O_{tot}/C_{tot}. The intensities of the components resulting from the non-linear fitting are given in *Appendix I.* Analysis of Table 3.7 confirms that the char samples exhibit a pronounced tendency to uptake oxygen during the oxidation stage even after multiple cycles. Table 3.7 shows also a progressive drop of carbon content after oxidation/desorption cycles and a decrease of oxygen content as result of the desorption steps. The following bar graph histograms report the calculated relative intensities of the components of the *C1s* and *O1s* spectra of oxidized sample (Fig.3.13):

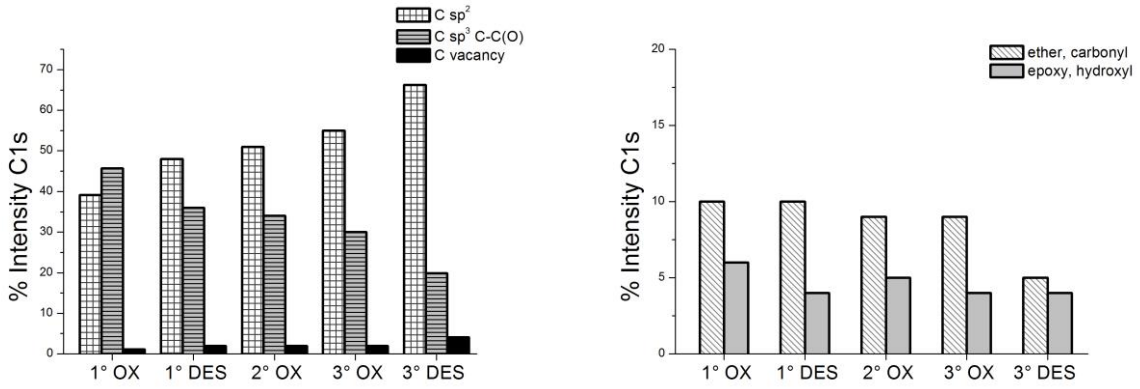

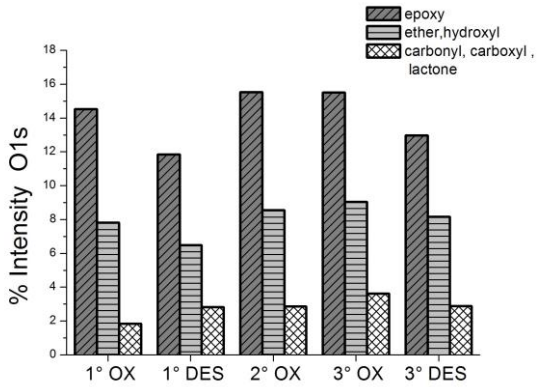

Fig.3.13. Intensities of the components of the *C1s* and *O1s* spectra of oxidized char samples after oxidation/desorption cycles.

Results referred to char coal oxidized at 527 K (*1° Ox*) were previously discussed. Upon thermal treatments, a pronounced increase in intensity of the C sp^2 component is observed, accompanied by a decrement of C sp^3 and C-C bonds in proximity of oxidized sites (C-C(O)) and of ether-carbonyl component. The carbon vacancies increase as a consequence of carbon consumption and the formation of new active sites. No significant variations are shown by epoxy-hydroxyl group. The *C1s* spectra evolution can be explained by a considerable expansion of aromatic domains C sp^2 as result of graphitization process and a decay of the C-C(O) bonds as they progressively transform into C−O bonds.

O1s spectra still reveal the existence of the main component with epoxy group as predominant species at low oxidation temperature, followed by ether and carbonyl component. To better clarify this evidence, Fig.3.14 shows the evolution of each functional group estimated from *O1s* spectra deconvolution.

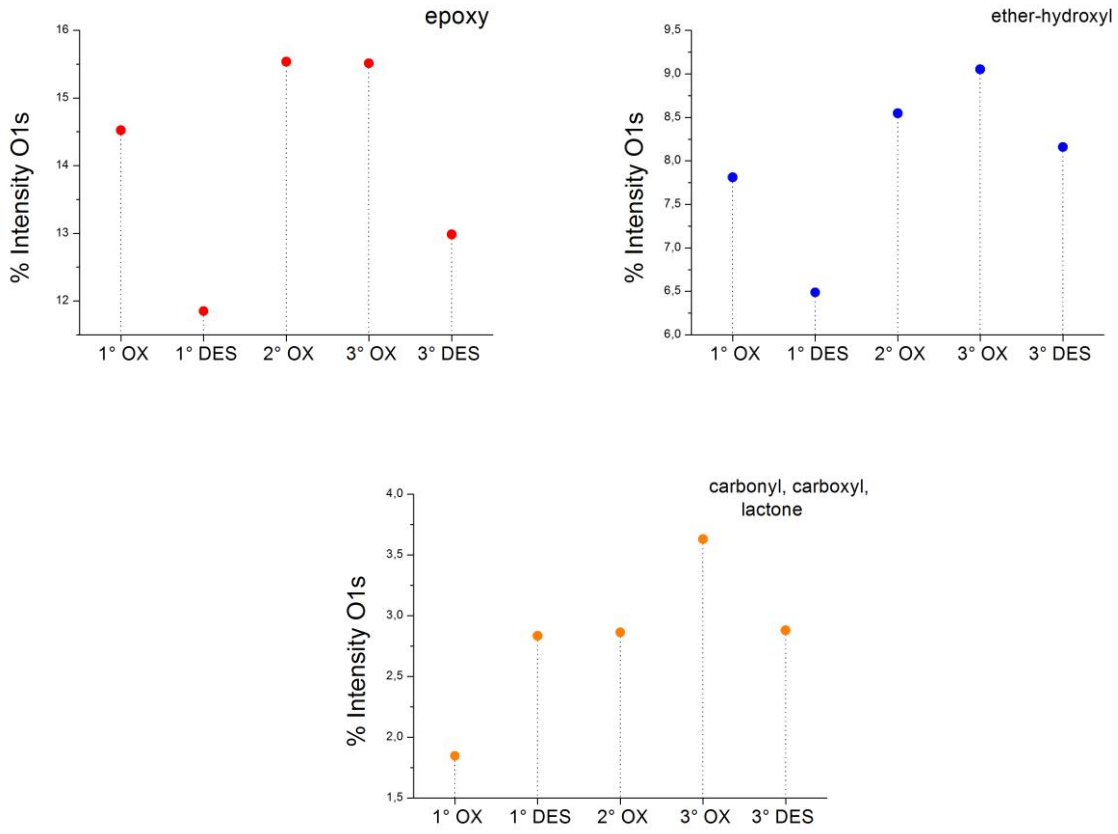

Fig.3.14. Evolution of "epoxy", "ether-hydroxyl" and "carbonyl-carboxyl-lactone" estimated from *O1s* spectra deconvolution spectra of oxidized char samples after oxidation/desorption cycles.

Upon the 1° Desorption Cycle the peak of the epoxy decays significantly, further decrement of ether-hydroxyl is observed. This result is in agreement with previous study made by Senneca et al. [144,145]. A first remarkable result regards the growing of carbonyl component. Upon the 2° Oxidation Cycles an increase in the ratio of the epoxy is evident. However, the carbonyl group does not show further increase. Upon the 3° Oxidation Cycle, the peak of the epoxy group does not show further increment pointing out rearrangement of epoxides towards ether and/or carbonyl group. The peak of adsorbed H_2O probably trapped in the pore structure may arise from the desorption of hydroxyls favoured by surface structural rearrangements [29]. The 3rd Desorption Cycle shows again the decay of the epoxy component, followed by the decrement of ether-hydroxyl end carbonyl groups. It is interesting to note that the two desorbed char samples show the same relative amount of carbonyl group. This peak may arise from a balance between the fraction of carbonyl desorbed as CO/CO_2 and the fraction of carbonyl rearranged. Upon the 1° Desorption Cycle the fraction of carbonyl rearranged

is higher, while upon the 3° Desorption Cycle the desorption of carbonyl may be favoured due to higher ratio carbonyl/epoxy.

XPS results of the samples prepared by means of discontinuous experiments in a fluidized bed micro reactor in the present work, confirm rearrangement of surface oxides (epoxy) upon thermal treatments.

This interesting result is supported by Molecular Dynamic simulations found in literature. Computational study revealed that reduction by thermal treatment leads to the formation of carbonyl and ether groups [27-29]. Bagri et al. analysis revealed that the formation mechanisms of groups such as carbonyls and ether rings have different origins. Overall, carbonyls were created by rearrangement of epoxy groups and hydroxyls closely surrounded by saturated carbons (sp^3), but the formation of substitutional oxygen (C–O–C ether rings) was favoured at high temperatures. They found that the formation of carbonyls is linked to the interplay between hydroxyl and epoxy groups or to two epoxy groups bonded with two neighbouring carbon atoms and facing the opposite side of the sheet. The generation of carbonyls was favoured thermodynamically, as shown by the reduction in the total energy of the system on formation of these functional groups. Moreover, the relative stability of holes decorated by carbonyl pairs was explained by the strain in the basal plane induced by different functional groups. They found that, in the case of a hole with a carbonyl pair, the bonding configuration remains close to planar sp^2 hybridization because of the formation of C=O bonds, which leads to little strain in the basal plane. A hole with a carbonyl pair is therefore a relatively strain-free structure that results in a lower formation energy compared to that for the epoxy pair [29].

Larciprete et al. employed high resolution XPS spectroscopy (HR-XPS) with synchrotron radiation in conjunction with ab initio calculations to probe oxygen functionalities on the surface of highly oriented pyrolytic graphite (HOPG) after oxidation with atomic oxygen and upon heating. They found that in the early stages of oxidation, epoxy is the dominant surface species, while ethers and C=O bonds become more abundant in the later stages of oxidation as a result of O saturation of vacancies and dangling bonds at the edges. Furthermore, they suggested that, for high concentration of neighbouring epoxy oxygen on the C basal plane of graphite, the aligned epoxy groups tend to unzip into ethers due to the cumulative cleaving force exerted on the underlying C–C bonds [27,28].

Senneca et al. [145] in previous campaign by thermal analytical experiments, observed a pronounced exothermicity at 473 K, when the DTG profile associated with mass loss of the samples was flat and well before the sample starts to release CO_2. When, at higher temperature, desorption of CO and CO_2

takes place, minima in the DSC curves were recorded. These two circumstances suggested that chemisorption and rearrangement of surface oxides towards more stable species might be exothermic while, as expected, abstraction of CO and CO_2 is inherently endothermic [145].

The comparison of results obtained with char samples prepared by means of discontinuous experiments in a fluidized bed micro reactor are interpreted in the conceptual frame of recent result of Senneca et al. [145]. They have proposed a frame of the thermochemistry associated with the interplay of different reaction paths:

$C_f^* + O_2 \xrightarrow{1} C(O)^{\#}$	$\Delta H < 0$	formation of '*metastable*' surface oxides
$C(O)^{\#} + O_2 \xrightarrow{2} C(O) + CO, CO_2$	$\Delta H < 0$	oxygen-driven complex switch-over
$C(O)^{\#} \xrightarrow{3} C(O) + CO, CO_2$	$\Delta H < 0$	rearrangement of '*metastable*' oxides into stable complexes
$C(O) \xrightarrow{4} C_f^* + CO, CO_2$	$\Delta H > 0$	desorption into CO, CO_2

When oxidation is performed at low temperature, chemisorption is likely to occur extensively, but the energy barrier for the rearrangement of the early oxides towards more stable forms is not overcome. Upon further heating up and in the inert conditions typical of TPD experiments, reaction *step 3* occurs in parallel with release of CO/CO_2 (reaction *step 4*). The overall heat of reaction is the result of the balance between the heat associated with reaction *steps 3* (exothermic) and the heat associated with reaction *step 4* (endothermic). The overall thermochemistry will be determined by the balance between exo- and endothermic processes. The temperature at which chemisorption is performed is relevant to the balance of exo- vs. endothermic processes and to the overall thermicity [145]. As mentioned before, when exposure to oxygen is performed at moderate temperature, oxidation extends beyond the chemisorption step. This implies that *step 2* may partly take place in the pre-oxidation step, disclosing its exothermic nature [145].

The framework provided should only be regarded as a broad reference. It assumes the existence of only one type of native chemisorption sites, and only one path towards site rearrangement/stabilization, at odds with the well-known existence of a wide population of sites on the surface of coal char [24,25].

3.4 Conclusions

The chemical nature of the carbon–oxygen complexes on the surface of solid carbons was investigated with reference to a char from medium-rank coal (South African).

Correlating thermoanalytical and structural (XPS) characterization, suggests the effect of temperature of oxidation on the nature of the carbon–oxygen complexes. In particular, deconvolution of the *O1s* spectra provides valuable clues on epoxidation as being the prevalent type of oxygen functionalization when oxidation is performed at low temperature (early stage of oxidation). TPD measurements show that the amount of surface oxides responsible of the desorption of CO-CO_2 increases, when expose to oxygen is performed at temperature up to 700 K. At the same time, *O1s* spectra show a more pronounced increase in the number of ether and carbonyl bonds. This observation suggests that the rearrangement of the C–O bonds takes place during oxidation up to 700 K.

Experimental results are in substantial agreement with semiglobal reaction scheme that was assumed as the reference [145] and provide additional insight into the role of the individual reaction steps. Altogether TPD and XPS characterizations, suggest that the "metastable" oxides may prevailingly consist of epoxy functionalities, whereas the more stable oxides would be composed by ether and carbonyl moieties. At higher temperatures, and upon extensive oxidation (in particular: $T \approx 700$ K, $f \approx 20$), "metastable" surface oxides (epoxy) evolve into more stable carbon-oxygen complexes (ether, carbonyl). When oxidation is performed at $T \geq 800$ K, the desorption of functional groups has already happened, leaving a low amount of surface oxides (mainly epoxides). In addition, results suggest that the interaction of the epoxy groups with the other surface oxides (ether, carbonyl) could explain the enhanced evolution of CO-CO_2 in TPDs when expose to oxygen is performed at temperature up to 700 K and $f \approx 20$. In particular, the ratio between carbonyl/epoxy and ether-hydroxyl/epoxy could promote the removal of C atoms from the C and back bone as results of CO/CO_2 evolution. Experimental results underline the importance of evolution of epoxy group into more stable surface oxides (by complex-switch-over driven by molecular oxygen) when oxidation temperature is performed up to 700 K.

Results are helpful not only in view of applications to stationary combustion or gasification of carbons, but also to shed light on the dynamical patterns of carbon chemisorption/desorption under alternating oxidizing conditions, relevant to "looping combustion" of carbon, as in the "Carboloop" concept proposed by the Naples group. In fact, thermally activated rearrangement/isomerization or

complex-switch-over driven by molecular oxygen of surface oxides, are the very key points of the Carboloop process. XPS results of the samples prepared by means of discontinuous experiments in a fluidized bed micro reactor in the present work, confirm rearrangement of surface oxides (epoxy) upon thermal treatments.

.

Chapter 4

Assessment of the influence of oxyfiring conditions on char structure and reactivity

4.1 Introduction

When coal particles are heated up in an oxy-combustor, they undergo the stage of heat up and pyrolysis in a CO_2 rich atmosphere. Besides the well-known influence of thermal conditions, the composition of the pyrolysis atmosphere may also have important effects on the formation and properties of pyrolysis products [82,192]. As a matter of fact, a large concentration of carbon dioxide may impact on the reactive processes all the way through devolatilization and char burnout. An international collaboration, embodying researchers from three institutions (Aachen, Bochum and Naples) has engaged an experimental campaign directed to understand the effects of CO_2 enriched atmospheres on coal pyrolysis and oxy-combustion [82,192]. The rationale behind the experimental campaign is summarized in Fig.4.1.

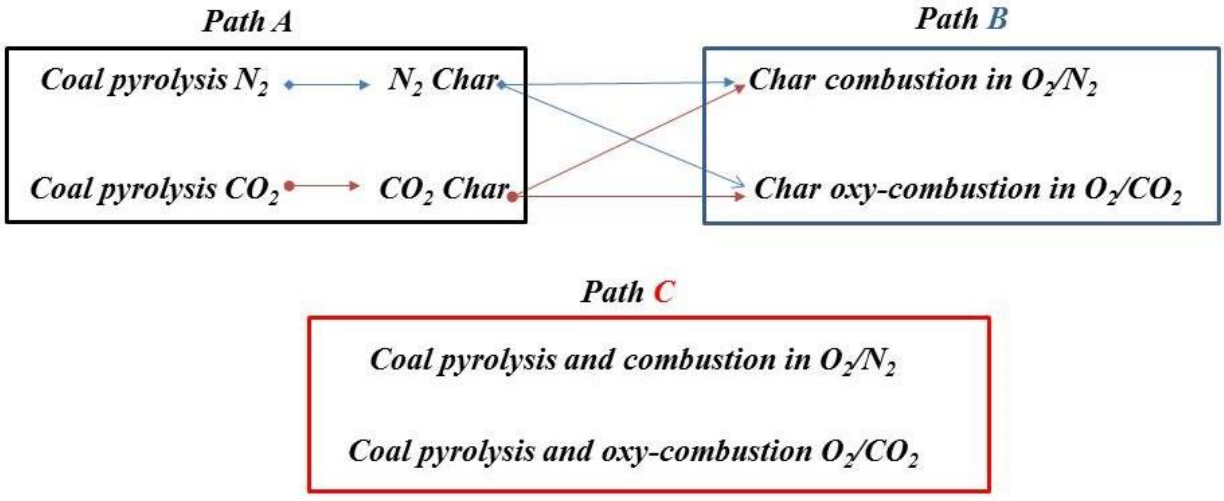

Fig. 4.1. Rationale of the experimental campaign.

According to Fig.4.1 the ***Chapter 4*** is divided in the following parts:

-*Characterization of products of coal pyrolysis at conditions relevant to oxyfiring (4.3.1)***:** in order to isolate the effects of CO_2 on the pyrolysis stage, the current study compares the influence of inert (N_2) vs. reactive (CO_2) gas atmospheres as well as reactor type (and associated test conditions) on properties of gas, tar and char from pyrolysis of a high volatile bituminous coal. This section correspond to the study of ***path A***. Pyrolysis products were analyzed by several techniques to highlight differences in structure, reactivity and chemical composition [82,192]. Samples pyrolyzed in DTR by ***path A*** have been subjected to isothermal and non-isothermal TGA experiments carried out with $O_2/CO_2/N_2$ atmospheres with the aim of assessing the intrinsic kinetics of the chars with O_2, CO_2 and mixtures of O_2/CO_2 (*regime I*) (***path A+ B)***.

-*Evolution of carbon structure in oxyfiring conditions (4.3.2):* DTR have been used to perform tests in oxidizing environments: air (21 vol% O_2/N_2), oxy21 (21 vol% O_2/CO_2) and oxy30 (30 vol% O_2/CO_2). The scope was to investigate the fate of coal in atmospheres typical of air and oxy-fuel combustion (*regime II*), when pyrolysis, the early stage of combustion and gasification potentially overlap, which correspond to ***path C***. Samples produced in DTR by ***path C*** at residence time of 120-130 ms, were analyzed by several techniques to highlight differences in structure and chemical composition.

The experimental campaign has been carried out in collaboration with the Ruhr University of Bochum and RWTH of Aachen. The location of the experimental set ups is specified in section 4.2.

4.2 Experimental Section

4.2.1 Material

A hard coal from Colombia was used for the current experiments. Proximate and ultimate analysis data are given in Table 4.1, classifying the coal as high volatile bituminous coal. The fuel was sieved to a suitable size fraction with a mass-weighted diameter of d_{50} = 108 µm. Proximate analysis (moisture, ash and volatile matter) of the coal was carried out in accordance to DIN standards 51718 (moisture at 379 K), 51719 (ash at 1088 K), 51720 (volatile matter at 1173 K) and 51900 (higher heating value HHV).

Table 4.1. Standardized analyses of the examined Colombian coal (dry basis except moisture).

Moisture (wt%)	**Ash** (wt%)	**Volatiles** (wt%)	**C** (wt%)	**H** (wt%)	**N** (wt%)	**S** (wt%)	**O** [a] (wt%)	**HHV** (MJ/kg)	**d_{50}** (µm)
2	4.8	39.0	75.2	5.1	1.7	0.84	12.3	31.000	108

4.2.2 Experimental Setups

The experimental conditions are summarized in Table 4.2 for comparison at a glance.

Table 4.2. Summary of the process conditions.

Reactor type	**TGA**	**FixBR**	**FBR**	**DTR**
Location	Naples	Naples	Aachen	Bochum
Process type	Batch	Batch	Batch	Continuous
Temperature	1173 K	873 K	1473 K (oven)	1573 K (wall)
Gas flow (l/min)	0.2	0.2	0.833	50
Heating rate	5 K/min	5 K/min	1-2·10^4 K/s [a]	≈ 3·10^4 K/s [b]
Residence time (s)	1800 [c]	5400 [c]	10	0.12 (N_2) [b] 0.13 (CO_2) [b]
Time resolution (s)	1	30	2 (FT-IR)	-
Gas analysis	-	x	x	x
Tar analysis	-	x	-	x
Char analysis	-	x	x	x
Soot-like analysis	-	-	-	x

[a] estimation based on CPD model prediction. [b] calculated with CFD model. [c] holding time after heat-up.

A preliminary screening of the pyrolysis of the Colombian coal in N_2 and CO_2 was carried out by **thermogravimetric analysis**. Different test rigs have then been used to perform pyrolysis with different heating rates, final temperature and holding time: A **fixed bed micro reactor (FixBR)** with heating rates of 5 K/min and holding times in the scale of minutes/hours; a **fluidized bed reactor**

(FBR) capable of heating rates in the order of 10^4 K/s and residence times in the scale of seconds; a **drop tube reactor (DTR)**, where particle heating rates in the order of 10^4-10^5 K/s and residence times in the scale of milliseconds can be established. Experimental activity in DTR has been carried out by the Group of Professor Scherer in Ruhr University in Bochum, while experimental activity in FBR has been carried out by the Group of Professor Kneer RWTH in Aachen. Detailed descriptions of **FBR** and **DTR** are given in *Appendix II*. FBR-chars and DTR-chars were sent to Naples to investigate differences in structure, reactivity and chemical composition. In the course of the experimental work regarding the drop tube pyrolysis of coal, the appearance on the wall of the ceramic filter of a fluffy carbonaceous solid material, different from char collected at the bottom of the ceramic filter was noticed [81]. This phenomenon was more remarkable in CO_2 than in N_2. The soot-like and char fractions have been effectively separated from each other implementing a procedure based on the suspension of raw carbon particulate in ethanol, followed by settling, and decanting [119,192]. The structural characterization of char and soot-like was verified by several chemical and spectroscopic techniques.

4.2.3 Pyrolysis experiments

Thermobalance. Pyrolysis experiments were carried out in a *Netzsch 409 TG-DSC* apparatus. Approximately 20 mg of sample were loaded in the pan in each test. An upward flow of gas of 200 ml/min was used. The temperature was raised from 298 K to 423 K and held at 423 K for 5-10 min to release moisture. The sample was then further heated up at a constant heating rate of 5 K/min to the final temperature of 1173 K. The sample was finally held at isothermal conditions for 30 min. Experiments were carried out in 100 mol% N_2 and 100 mol% CO_2. The mass recorded during experiments is worked out in order to obtain TG plots of w/w_0 vs. T and DTG plots of $(dw/dt\ w_0^{-1})$ vs. T, where w, w_0 are the actual and the initial weight of sample (after the dehumidification stage), t the time and T the temperature. The DSC curves were also recorded throughout the experiment.

Fixed bed reactor. A fixed bed micro reactor was set up for pyrolysis experiments as depicted in Fig.4.2.

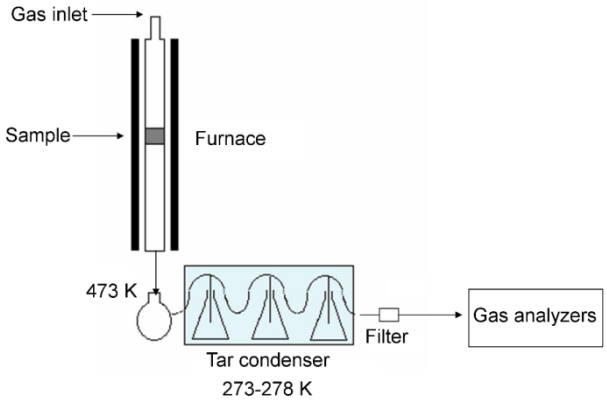

Fig.4.2. Fixed bed micro pyrolysis reactor.

The reactor consists of a tubular quartz reactor (inner diameter d_i = 20 mm) heated externally by an electric furnace. Approximately 1 g of the sample is placed inside the reactor from the very beginning of the experiment and heated accordingly. A thermocouple is inserted into the bed. N_2 or CO_2 are fed from the reactor top at flow rate of 0.2 l/min (STP) and leave the reactor from the bottom. The reaction products at the reactor outlet are quickly cooled down to 473 K and then to 273 K as they flow through three bubblers (without solvent) in series. The tar captured by the bubblers is analyzed off-line by a gas chromatograph (GC) coupled with a mass spectrometer (MS). The incondensable gas stream which leaves the bubblers passes through a filter to capture residual tar or water and then is sent to gas analyzers (*ABB AO2020*), including *Caldos 27* and *Uras 26* modules, for the measurement of O_2, CO, CO_2, CH_4 and H_2. The yield in tar and char was assessed by weighing the collected samples. The gas yield was determined by difference. The overall yield of CH_4/CO/H_2/CO_2 was also measured by integration of the gas concentration profile. It was calculated that CH_4/CO/H_2/CO_2 accounted for approximately 90% of the gaseous yield.

4.2.4 Samples characterization

Gas. As the three test rigs are equipped with different gas analyzers, which are calibrated for different gas species, typical light gas species were identified which could be used to compare the gas evolution under these conditions in the specific test rigs. The typical light gas species CH_4, CO and CO_2 were identified as useful measures in all test rigs. Additionally, H_2 emissions for the both fixed bed experiments are given.

Tar. The tar samples of the fixed bed reactor were dissolved out in two steps (1-propanol and acetone) and analyzed by a gas chromatograph and online mass spectrometry as detector (GC-MS) (*AGILENT GC 7890* apparatus coupled with *MSD 5975C*). In the GC an *HP-35* (length 30 m, d_i 250 µm, film 0.25 µm) column is mounted. Sample injection was done in splitless mode at 523 K with a gas flow of 1 ml/min (STP). The temperature program consists of four isothermal steps: 323 K (5 min), constant heating for 30 min to 473 K (5 min), constant heating for 1.75 min to 543 K (5 min) and finally constant heating for 6 min to 573 K (15 min). The transfer line between the GC and the MS is held at 573 K. MS spectra are acquired in scan mode in the range 40-500 amu.

Char. Char samples from the FixBR, FBR and DTR were analyzed in detail by several techniques.

The elemental composition was determined by a *LECO CHN 628*.

Scanning electron microscopy (SEM) was used in order to get a first impression of the changes in char surface properties. SEM images were taken with a *FEI INSPECT S.*

X-ray photoelectron spectroscopy (XPS) was carried out by an UHV set-up equipped with a *Gammadata-Scienta SES 2002* analyzer to analyze the surface of the char samples. At a pressure of $5 \cdot 10^{-10}$ mbar, the samples were exposed to monochromatic Al Kα (1486.6 eV, 14.5 kV, 30.5 mA) radiation and a pass energy of 200 eV was chosen to achieve an energy resolution better than 0.6 eV. A flood gun was used to compensate charging effects. The main *C1s* peak at 284.8 eV, which originates from carbon contaminations, was used to calibrate binding energies. XPS experimental activity has been carried out by the Group of Professor Scherer in Ruhr University. Spectra interpretation has been carried out jointly with Naples.

X-ray diffraction (XRD) profiles were recorded using a *Bruker D2 Phaser* apparatus with Cu Kα radiation (30 kV, 10 mA). Scattered X-ray intensities were collected between $2\theta = 5$ and 75° with a scan velocity of $0.05 \cdot 2\theta$ s^{-1}.

The *Netzsch 409 TG-DSC* apparatus has been used to perform also combustion and temperature programmed desorption (TPD) experiments of the chars produced in the previously described test rigs. In combustion experiments, the heating rate was set at 5 K/min and the final temperature at 1123 K. A flow of synthetic air (21 mol% O_2 and 79 mol% Ar) is used. In TPD experiments the heating rate is set at 20 K/min and the final temperature is at 1473 K. A gas flow of pure Ar is used. On-line analysis of CO and CO_2 in the off gas is carried out by means of *ABB AO2020* analyzers.

Soot-like/char separation. The soot-like/char separation procedure here presented is based on that set up in previous works [119]. Experimental activity of soot-like/char separation has been carried out

by the Group of Dr. Cajolo and Dr. Apicella in IRC-CNR. Interpretation has been carried out jointly, in particular comparing this carbonaceous solid material with char collected at the bottom of the ceramic filter, analyzed section 4.3.1 '*char analysis'*.

About 100 mg of raw carbonaceous particulate was placed in a 50 ml Falcon tube with 40 ml of ethyl alcohol and agitated using an ultrasonic bath for 5 min. The suspension was then allowed to settle for about 45 min. The top 20 ml of the suspension was decanted into a second tube, and the tube containing the bottom fraction was refilled. Both tubes were again ultrasonically agitated, and the settling was repeated. The number of the extractions steps were repeated until the complete disappearance of suspended particles in the solution. The two products, soot-like and char, so separated were dried by evaporation and weighed. The balance closure for total mass used to check the quality of the quantitative separation results.

Soot-like and Char samples were analyzed in detail by several techniques.

XRD, TG-DSC and SEM devices are previously described.

FTIR spectra in the 4000–400 cm^{-1} range were acquired in the transmittance mode using a *Nicolet iS10* spectrophotometer. Analysis has been performed on sample dispersions prepared by mixing and grinding the samples in KBr pellets (0.2–0.3 wt%). The KBr dispersions were compressed at 10 Ton for 10 min into a thin disk. KBr disks were dried before performing the analysis in a desiccator for 48 h to remove the absorbed water.

Raman spectra were measured by means of a *Horiba XploRA* Raman microscope system with an excitation wavelength of λ=532 nm (frequency doubled Nd:YAG-solid state laser, 25 mW). Care has been taken to avoid modification of the carbon structure due to laser-induced heating effects. To minimize the probability of structural damages due to the thermal decomposition induced by the laser, the power of the excitation laser beam was reduced to about 0.1 mW. The Raman spectra were collected with an acquisition time of 30 s and an accumulation of 6 runs.

4.2.5 Thermogravimetric analysis of DTR N_2 and DTR CO_2 chars

Thermogravimetric analysis was carried out on DTR N_2 and DTR CO_2 chars. Non-isothermal TGA is a common technique for a fast comparison of coal reactivity, since one single run allows to scan a large temperature interval. The peak of the DTG curves (derivative of the weight loss) is considered to give a reasonable ranking of different chars. The assessment of kinetic parameters from non-isothermal TG tests is of course a more difficult job. In general, isothermal TGA is considered more

adequate for kinetic analysis, but requires a large number of tests at different temperatures to be performed. In the present work, the limited availability of char samples justified the recourse to a combination of non-isothermal and isothermal TGA experiments, as will be described in the following.

Experiments were carried out in a *Netzsch 409 TG-DSC* apparatus with experimental conditions summarized in Table 4.3. A notation of the type DTR A-E G has been used to label the experiments, where A describes the atmosphere of the char preparation experiment in the drop tube reactor (N_2 or CO_2), E describes the type of thermogravimetric experiment (TGNI for non-isothermal and TGI for isothermal thermogravimetric experiment), G the gas composition of the TG experiment. In all the experiments, approximately 20 mg of sample were used, and the gas flow rate was 200 ml/min (standard temperature and pressure, STP). In non-isothermal experiments, the sample was heated up in a reactive atmosphere of desired composition with a heating rate $H = 5$ K/min to the final temperature T_f and then held at this temperature for a time of $t_h = 30$ min. In isothermal TG tests, the reaction temperature was reached instead in flowing argon, then the gas was switched to the desired composition and the sample was held at these conditions until complete burn off.

Isothermal air experiments were carried out at four different values T_f within the range 623-748 K. Isothermal CO_2 experiments were carried out at three values T_f in the range 1073-1173 K. Notably, the isothermal TGA tests were limited to only two gas compositions and a maximum of four temperature points for each, due to the limited amount of char samples available.

Table 4.3. Experimental conditions of TGA experiments.

TG experiment	**TG technique**	**Gas composition (vol%)**			T_f	t_h	H
DTR A-E G		Ar	CO_2	O_2	(K)	(min)	(K/min)
DTR N_2-TGNI air	NI	79		21	1173	30	5
DTR CO_2-TGNI air	NI	79		21	1173	30	5
DTR N_2-TGNI oxy30	NI		70	30	1173	30	5
DTR CO_2-TGNI oxy30	NI		70	30	1173	30	5
DTR N_2-TGNI CO_2	NI		100		1373	30	5
DTR CO_2-TGNI CO_2	NI		100		1373	30	5
DTR N_2-TGI air	I	79		21	623-748		
DTR CO_2-TGI air	I	79		21	623-748		
DTR N_2-TGI CO_2	I		100		1073-1173		

Precautions were taken to favor uniformity of temperature within the sample and absence of internal and external mass transfer limitation, accordingly the particle size was low (≅ 100 μm) in all experiments and the sample was evenly spread on the sample pan. Moreover, in non-isothermal

experiments a slow heating rate was used (5 K/min) and in isothermal experiments the upper limit of the temperature was kept low to remain under *regime I* conditions.

Even though, multistep reaction schemes were proposed to describe the chemistry of char oxidation over wide pressure and temperature ranges [151], for sake of simplicity in the present work, a single power law expression will be used to describe the kinetics of coal char oxidation and gasification.

The degree of char (or rather carbon) conversion f of a char particle is herein defined as:

$$f = \frac{m_0 - m(t)}{m_0 - m_\infty} \tag{4.1}$$

m_0 is the initial mass of the char, m is the mass of the char at time t and m_∞ is the mass residue in the TG experiment (equal to the ash content of the corresponding char). During the conversion process, the instantaneous reactivity r of the char can be expressed as:

$$r = \frac{df}{dt}\,\frac{1}{A(f)} = k_0 \exp\left(-\frac{E_\mathrm{a}}{R_{gas}\,T}\right) p_{\mathrm{O2/CO2}}^{n} \tag{4.2}$$

where k_0 ($\mathrm{min^{-1}\ bar^{-n}}$) is the pre-exponential factor, E_a (kJ/mol) the activation energy, p (bar) the partial pressure of the gaseous reactant (O_2 or CO_2), n the reaction order (which is assumed to be equal to unity in the present work) and R_gas the ideal gas constant. $A(f)$ is a function which takes into account the evolution of conversion rate with carbon conversion degree.

In order to evaluate the kinetic parameters of eq.4.2, results of both non-isothermal thermogravimetric and isothermal thermogravimetric experiments have been used, according to the following procedure:

Firstly, the weight loss data measured during TGI experiments were worked out to calculate:

- Plots of instantaneous rate of reaction df/dt vs. carbon conversion f;
- Time to attain 50% of char conversion τ;
- Plots of normalized rate of reaction $\tau\, df/dt$ vs. carbon conversion.

Notably, upon normalization the plots relative to the different temperatures merge in one single curve which can be described by the equation $\tau\,(df/dt) = Y(f)$. Regression over this curve allowed to estimate the function $Y(f)$, and consequently of the function $A(f)$ in eq.4.2.

Secondly, the weight loss data measured during both TGNI and TGI experiments have been worked out to obtain Arrhenius plots:

- TGNI: Arrhenius plots of instantaneous conversion rate: $\ln\,(df/dt\;(A(f)^{-1})$ vs. $1/T$,
- TGI: Arrhenius plots of average rate in the first 50% of conversion $\ln(R{=}0.5/\tau)$ vs. $1/T$.

Regression of the Arrhenius plots from TGNI and TGI experiments allowed to estimate the values of pre-exponential factor and activation energy of eq.4.2.

4.2.6 DTR oxy-char samples

The same experimental procedure and set up of the DTR reactor was used to perform tests in oxidizing environments: air (21 vol% O_2/N_2), oxy21 (21 vol% O_2/CO_2) and oxy30 (30 vol% O_2/CO_2). The scope was to investigate the fate of coal in atmospheres typical of air and oxy-fuel combustion, when pyrolysis, combustion and gasification potentially overlap, which correspond to ***path C*** in Fig.4.1. Char samples collected at 120-130 ms residence time have been labelled as DTR air, DTR oxy21, DTR oxy30, respectively [81].

The chars collected at the outlet of the drop tube reactor were analyzed for their ash content (a_i), where a_{coal} is the mass fraction of ash in the raw coal and a_i the mass fraction of ash in the given char sample *i*. The mass loss *M* accomplished in the reactor was then calculated by means of eq.4.3:

$$M_{i,daf} = \left(\frac{1 - \frac{a_{coal}}{a_i}}{1 - a_{coal}} \right)_{dry} \tag{4.3}$$

Based on the ash content, which had already been reported in [81], char conversion degree *f* has been calculated according to the following eqs. 4.3 and 4.4:

$$f = \left(\frac{M_i - M_{N2}}{1 - M_{N2}} \right) \tag{4.4}$$

where M_{N2} is the mass loss in the DTR N_2 experiment. The residence time of the particles in the reactor, according to CFD calculations, is approx. 125 ms [81].

Notably in eq.4.4, the char conversion degree due to heterogeneous combustion is calculated by correcting the mass loss obtained under oxidizing atmospheres for the volatile loss due to pyrolysis, as measured in the nitrogen experiment (M_{N2}). In a first approximation, the total residence time is assumed as reaction time. This approach may appear coarse, but it was necessary to compare the (oxy-) combustion *conversion degree* in the DTR reactor (***path C***).

4.2.7 DTR chars characterization

All DTR chars were subjected to a detailed chemico-physical characterization which included proximate and ultimate analysis, helium density, N_2 and CO_2 adsorption, XRD, XPS, some of which were reported in previous section 4.2.4.

The density of the chars outgassed in vacuum was determined with buoyancy measurements in helium by a magnetic suspension balance of Rubotherm type IsoSORP Static at 298 K in a pressure range of 0-20 bar. This value can be interpreted as the true density of the solid. Experimental activity has been carried out in Ruhr University. Interpretation has been carried out jointly with Naples. Two different measurement methods were applied to determine the surface area of the chars in this study. The widely used N_2 adsorption measurements on the basis of the Brunauer-Emmett-Teller (BET) theory [186] were carried out to identify the surface area of macro- and mesopores. The micropore surface area of the chars was identified by CO_2 adsorption measurements. For the analysis of the CO_2 adsorption, Dubinin-Radushkevich-Kaganer (DR-K) is applicable [189,193] which is the most commonly used approach in literature. Before N_2 physisorption measurements, the chars were outgassed at 423 K overnight in vacuum and the following measurements were performed at 77 K (liquid nitrogen bath) using Bel-Japan Belsorp-Mini with optimized protocols and nitrogen of 99.995 % purity. The CO_2 measurements were carried out with the outgassed samples (1.5 h at 423 K in vacuum) at a temperature of 273 K and in a pressure range up to 1 bar and CO_2 of 99.995 % purity. Additionally, SEM imaging was done by means of Zeiss GeminiSEM.

4.3 Results and discussion

4.3.1 Comparison of experimental procedures for the characterization of pyrolysis relevant to coal oxyfiring

In order to isolate the effects of CO_2 on the pyrolysis stage, the current study compares the influence of inert (N_2) vs reactive (CO_2) gas atmospheres as well as reactor type (and associated test conditions) on properties of gas, tar and char from pyrolysis of a high volatile bituminous coal. This section corresponds to the study of ***path A*** (Fig.4.1). Pyrolysis products were analyzed by several techniques to highlight differences in structure, reactivity and chemical composition [82,192].

Fig. 3.3 reports the TG and DTG curves obtained from pyrolysis of coal in N_2 and CO_2. Between 573 and 823 K a marked stage of pyrolysis is observed in both N_2 and CO_2. Approximately 40 wt% (Table 3.4) is obtained with DTG peak at 710 K. Differences in N_2 and CO_2 appear negligible below 923 K, whereas differences appear evident above 923 K because of the onset of char gasification in CO_2, with a marked peak at 1173 K. The temperature of the FixBR experiments was set at 873 K on the basis of these results in the TG apparatus.

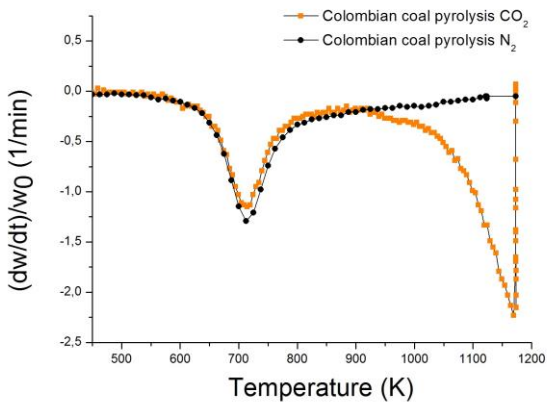

Fig. 4.3. TG and DTG curves of pyrolysis in N_2 and CO_2.

Pyrolysis products

The yield of different pyrolysis products is reported in Table 4.4 for all the experiments. Notably the yield in char in the FixBR experiments in both N_2 and CO_2 is consistent with the value from proximate analysis. The char yield decreases moving to the DTR-N_2 and further to FBR-N_2 chars.

Table 4.4. Pyrolysis yields on dry basis of all experiments in (wt%) .

	TGA		**FixBR**		**FBR**		**DTR**	
Atmosphere	N_2	CO_2	N_2	CO_2	N_2	CO_2	N_2	CO_2
Char	60 [a]	60 [a]	63 [a]	65 [a]	41 [b]	45 [b]	51 [b]	48 [b]
Soot-like	0	0	0	2 [a c]	n.d.	n.d.	4	29
Volatile	40 [d]	40 [d]			59 [d]	55 [d]	45 [d]	23 [d]
Thereof: **liquid**			19 [a]	16 [a]	26 [d]	n.d.	20 [d]	n.d.
Thereof: **gaseous**			18 [d]	17 [d]	33 [e]	n.d.	25 [e]	n.d.

[a] determined by weighing. [b] calculated by ash tracer method. [c] soot-like on filter. [d] calculated by difference. [e] calculated from gas analysis.

During experiments in the FixBR in CO_2, it was observed that the filters located before the gas analyzers often got clogged by a black sticky material. Moreover, a brownish powder was recovered also at the bottom of reactor and in the tubing from the reactor to the tar condensers. The same problem was not encountered in N_2 experiments. The material collected in the filter and also inside the tubing was observed by SEM and analyzed by coupled EDX. One image taken is shown in Fig. 4.4.

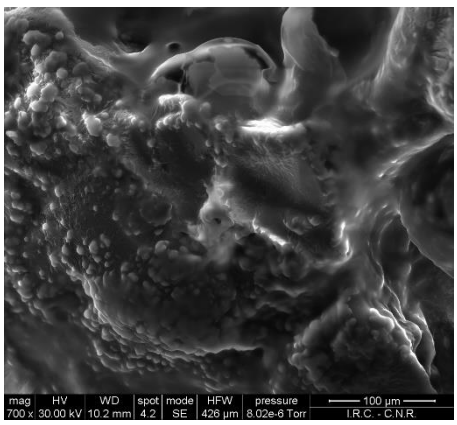

Fig.4.4. SEM image of deposits in the tubing downstream of the fixed bed reactor.

The elemental composition of the sample, determined by EDX, was mainly carbon with small percentage of oxygen. The sample seems to be constituted by a material fused and resolidified entrapping several microspheres with particle size below 4 µm. Upon prolonged exposure to the electronic beam, the matrix underwent visible transformations which indicated the occurrence of melting. Differently the spheres were not affected at all. This observation suggests that the matrix could be formed by a heavy tarry material, while the spheres appear soot-like solid carbonaceous products. From the weight gain of the filters a soot-like yield of 2 wt% was estimated in the FixBR-CO_2 experiment.

The gas species CH_4, CO and CO_2 were measured for all experiments. In the FixBR experiments, H_2 was also determined. To facilitate comparison and analysis of the results, the mass ratios referred to CO were calculated. The ratio CO_2/CO in the CO_2 experiments was excluded because the CO is not merely a pyrolysis product but originates also from gas phase and Boudouard reactions. The mass ratios are summarized in Table 4.5.

Table 4.5. Mass ratios of the selected representative light gas species.

Test rig	**FixBR**		**FBR**		**DTR**	
Atmosphere	N_2	CO_2	N_2	CO_2	N_2	CO_2
H_2/CO	0.19	0.18	n.d.	n.d.	n.d.	n.d.
CH_4/CO	1.2	1.2	0.05	0.001	0.47	0.02
CO_2/CO	1.5	-	0.16	-	0.50	-

It can be noted that the values of CO_2/CO and CH_4/CO decrease moving from FixBR to DTR to FBR suggesting high pyrolysis temperatures and long residence times increases the CO production due to the reverse water gas shift reaction. When CO_2 vs. N_2 experiments are compared, similar CH_4/CO and H_2/CO values are obtained for FixBR. Instead upon substitution of N_2 with CO_2 the CH_4/CO value decrease by a factor of 20 in the DTR and by a factor of 50 in the FBR. In fact, CO produced during the FBR experiment largely exceeded the carbon content of the parent coal while CO_2 yield was negative. It is believed that in the FBR, due to the long residence time (10 s) and high temperature (1473 K) the reverse water gas shift reaction and also heterogeneous gasification contributes to CO production.

The tars collected in fixed bed reactor test were analyzed by GC-MS. The temperature program of the GC-MS was limited to 573 K, therefore heavier tar was not properly identified. Table 4.6 presents

the ratio of peak area measured for each chemical species in the chromatograms of the tar produced in CO_2 over that of the tar produced in N_2. This analysis allows to compare at a glance whether the substitution of N_2 with CO_2 augments or reduces the yield in the given species. It can be observed that exposure to CO_2 brings about a general increase of aromatics with simultaneous decrease of aliphatic species.

Table 4.6. Tar compositions from fixed bed experiments presented as mass ratio (CO_2/N_2) of each tar species.

Compounds	**Yield in CO_2/ yeld in N_2**				
Phenol	1.62	Dimethyl-Phenol	1.94	Dimethyl-Naphthalene	0.95
Methyl-Phenol	0.97	Ethyl-methylPhenol	1.08	Trimethyl-Naphthalene	0.96
Ethyl-Phenol	1.63	Methyl-Naphthalene	0.89	Methyl-Phenanthrene	0.80
Dodecane	1.65	Tridecane	1.21	Tetradecane	1.02
Dodecene	1.72	Tridecene	1.25	Tetradecene	0.96
Pentadecane	0.97	Hexadecane	0.78	Heptadecane	0.92
Pentadecene	0.97	Hexadecene	1.37	Heptadecene	0.91
Octadecane	0.75	Nonadecane	0.83	Eicosane	0.85
Octadecene	1.08	Nonadecene	0.79	Eicosene	1.09
Heneicosane	0.89	Docosane	0.80	Tricosane	0.86
Heneicosene	1.01	Docosene	0.91	Tricosene	0.83
Tetracosane	0.87	Pentacosane	0.79	Hexacosane	0.85
Tetracosane	0.87	Pentacosene	0.78	Hexacosene	0.74
Heptacosane	0.85	Octacosene	0.91	Tricotane	0.09
Octacosane	0.99	Nonacosane	0.75		

The GC-MS analysis of the condensed tars of the DTR experiments was not quantitatively. Mass spectra of the resulting peaks [80] were used to identify the different chemical compounds. Due to the heterogeneity of the produced tars, separation of all chemical compounds was not always successful. Besides different hydrocarbons such as alkanes, alkenes and benzene derivates, oxygen-functionalized hydrocarbons such as alcohols or esters were detected. Nevertheless, the tars prepared in N_2 exhibited a smaller variety of olefins compared to the tars prepared in CO_2 atmosphere.

Char analysis

SEM pictures of the chars are shown on Fig.4.5.

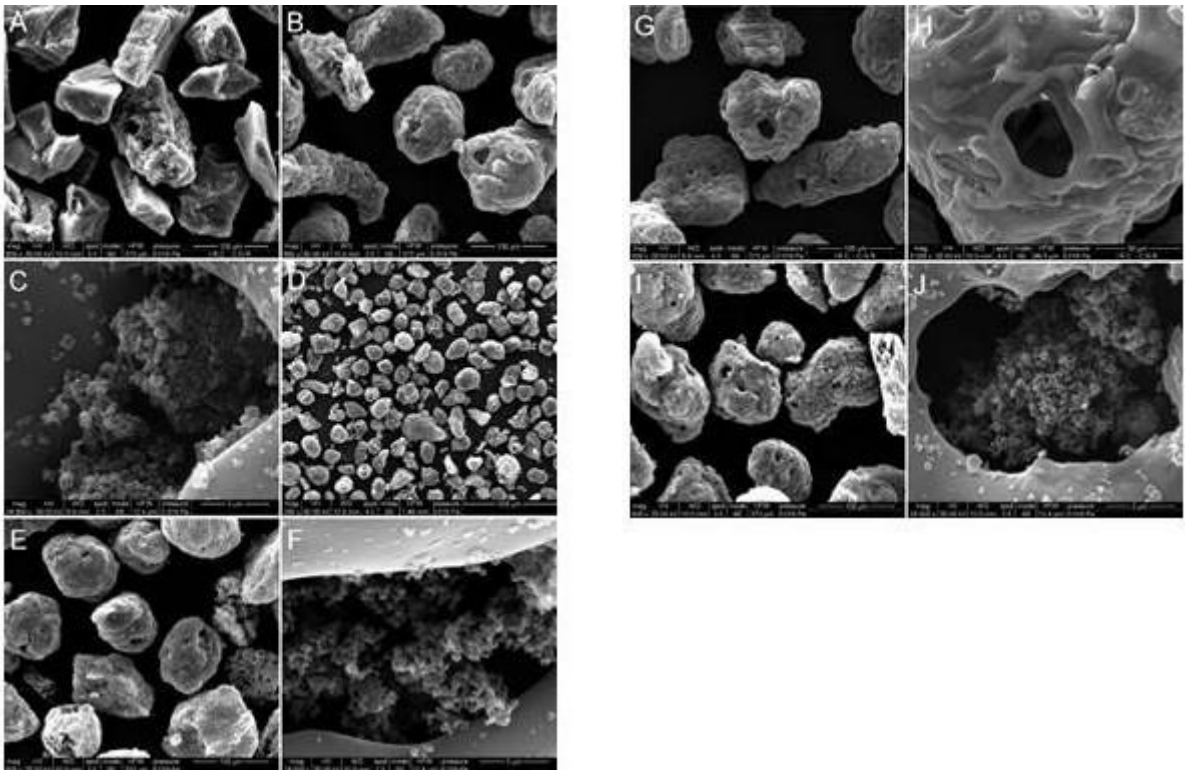

Fig. 4.5. SEM images: A FixBR-CO_2, B/C FBR-N_2, D/E/F FBR-CO_2, G/H DTR-N_2, I/J DTR-CO_2 .

Chars prepared in the fixed bed reactor looked quite similar at the SEM, therefore only the image of one of them (CO_2) is reported in Fig.4.5 A. Particles appear quite rough in shape and retain the original coal particle size. At higher magnification, some small particles are observed on the surface. The presence of pores is limited. Chars produced in the fluidized bed reactor in N_2 are shown in Fig.4.5 B/C. In this case particles morphology has changed. Particles appear smooth and rounded and large pores have been produced. On the surface of some of the particles, sub-micrometric soot-like particles can be observed. At larger magnification, it can be observed that aggregates of these particles can be found also inside the pores of some char particles. The elemental analysis by EDX confirm that they are essentially carbonaceous. Char particles produced in the fluidized bed reactor in CO_2 are shown in Fig.4.5 D/E/F. In this case particles still appear round with some pores. A population of char particles of smaller size (in the order of 20-30 μm) is also observed, which may have been

originated from fragmentation. Soot-like sub-micrometric particles appear to be largely present both on the particle surface and inside the pores.

Chars produced in the DTR are shown in Fig.4.5 G/H (in N_2) and I/J (in CO_2). In this case, particles appear smooth and porous but not round. At large magnification again the presence of soot-like carbon particles is observed also inside the pores of the CO_2-char.

The ash contents and elemental analysis (EA) of the char samples are summarized in Table 4.7. The ash content of char samples, when compared to the value of 4.8 wt% of the raw coal, indicates a volatile yield of 35 wt% in the fixed bed reactor, which is in good agreement with the amount of char recovered during the test and used to calculate the yields in Table 4.4. This value is slightly below the proximate analysis value of 39 wt% (Table 4.1), suggesting that the char contains a residual 4 wt% of non-devolatilized matter. The ash contents of DTR and FBR chars instead suggest completion of pyrolysis.

Table 4.7. Proximate and elemental analyses of different char samples on dry basis.

Test rig	**T** (K)	**Atm**	**C** (wt%)	**H** (wt%)	**N** (wt%)	**Ash** (wt%)	**H/C** [a]
FixBR	873 K	N_2	81.7	2.4	2.3	7.4	$2.9\ 10^{-2}$
		CO_2	80.5	2.2	2.4	6.9	$2.7\ 10^{-2}$
FBR	1473 K	N_2	86.8	0.4	1.3	11.5	$4.6\ 10^{-3}$
		CO_2	86.4	0.7	1.7	10.7	$8.1\ 10^{-3}$
DTR	1573 K	N_2	82.3	2.0	1.8	9.4	$2.4\ 10^{-2}$
		CO_2	82.7	0.8	1.6	10.0	$9.7\ 10^{-3}$
For comparison: raw coal			75.2	5.1	1.7	4.8	$6.8\ 10^{-2}$

[a] mass based.

Concerning N/C ratio, no significant change in this ratio was observed in all experiments. Important changes are instead observed in the H/C content of the chars, which is in fact indicative of the progress of aromatization and graphitization of the carbonaceous structure, also referred to as thermal annealing. Notably H/C value is maximum in the chars produced in the fixed bed reactor in both N_2 and CO_2, which can indeed be regarded as relatively young and little graphitized chars, while it decreases significantly in the high temperature chars.

The impact of pyrolysis conditions on the structure of the chars can also be analyzed from the XRD spectra of Fig.4.6. The diffractograms of turbostratic carbon materials such as coal chars typically exhibit two broad bumps in the regions around $2\theta = 25°$ (002) and 43° (10) bidimensional reflection).

These lines arise from scattering of X-ray radiation through the planes of the graphitic crystallites. In particular, the (002) peak correspond to the inter-layer spacing of graphite, while (100) and (110) peaks arise from hexagonal ring structure. In disordered carbons the (002) band is often found to be asymmetric because of the superimposition of the γ band at slightly lower 2θ values on the left-hand side. The γ band has been proven to be associated with the packing of saturated structures such as aliphatic side chains [175-178].

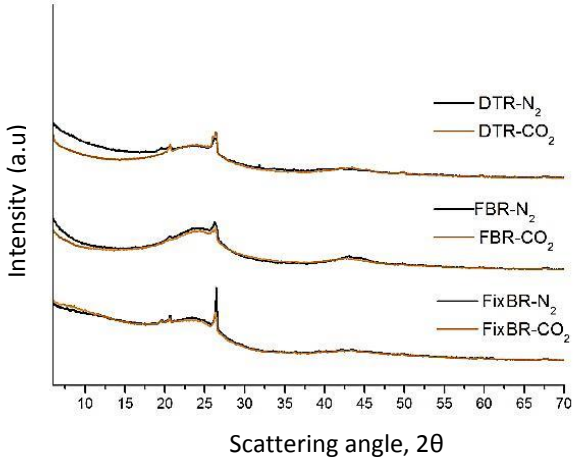

Fig.4.6. XRD patterns of the chars collected in the different test rigs.

In chars prepared in the fixed bed reactor (FixBR-N_2 and FixBR-CO_2) and also in the chars prepared in the drop tube reactor (DTR-N_2 and DTR-CO_2), the (002) and (10) bands hardly increase, whereas both bands become more intense and sharp in the char prepared in the fluidized bed reactor. Negligible differences are observed between chars prepared in N_2 or CO_2. In addition to the bands of the organic matter, other peaks are observed which pertain to inorganic matter, in particular to alumina silicates. In the raw coal sample, the peaks of quartz (SiO_2) are observed at $2\theta \approx 21°$ and 26.7° as well as those of kaolinite ($Al_2Si_2O_5(OH)_4$) at $2\theta \approx 12.5°$ and 25.0°. Endothermic dehydration of kaolinite begins at 823–873 K producing disordered meta-kaolin, and at higher temperature mullite and cristobalite. In fact, kaolinite disappears from the spectra of the chars prepared in the fluidized bed and drop tube reactor. The intensity of the peak attributed to quartz decreases in the chars prepared at higher temperature, as well, while another crystalline phase appears which can be attributed to mullite.

Fig.4.7 shows the DTG plots obtained during combustion of the six chars in TG. In all cases a single peak is observed. The temperature corresponding to the peak is reported in Table 4.8.

Table 4.8. DTG and TPD CO peak temperatures.

Test rig	**Atm.**	**DTG peak in air** (K)	**TPD in argon CO peaks** (K)
FixBR	N_2	780	1110/1570
FixBR	CO_2	780	1110/1570
FBR	N_2	800	1570
FBR	CO_2	795	1150/1570
DTR	N_2	730	1570
DTR	CO_2	810	1110/1570

It can be observed that the same values are obtained for the two FixBR chars in N_2 and CO_2. In the two fluidized bed chars, the main DTG peak are very close, but in the CO_2 char the rate of weight loss between 700 and 800 K is moderately higher than that of the corresponding N_2 char. Major differences are observed for the DTR chars: the DTG peak of the DTR-CO_2 char is shifted by 80 K compared to the DTR-N_2 char suggesting a distinctively lower combustion reactivity.

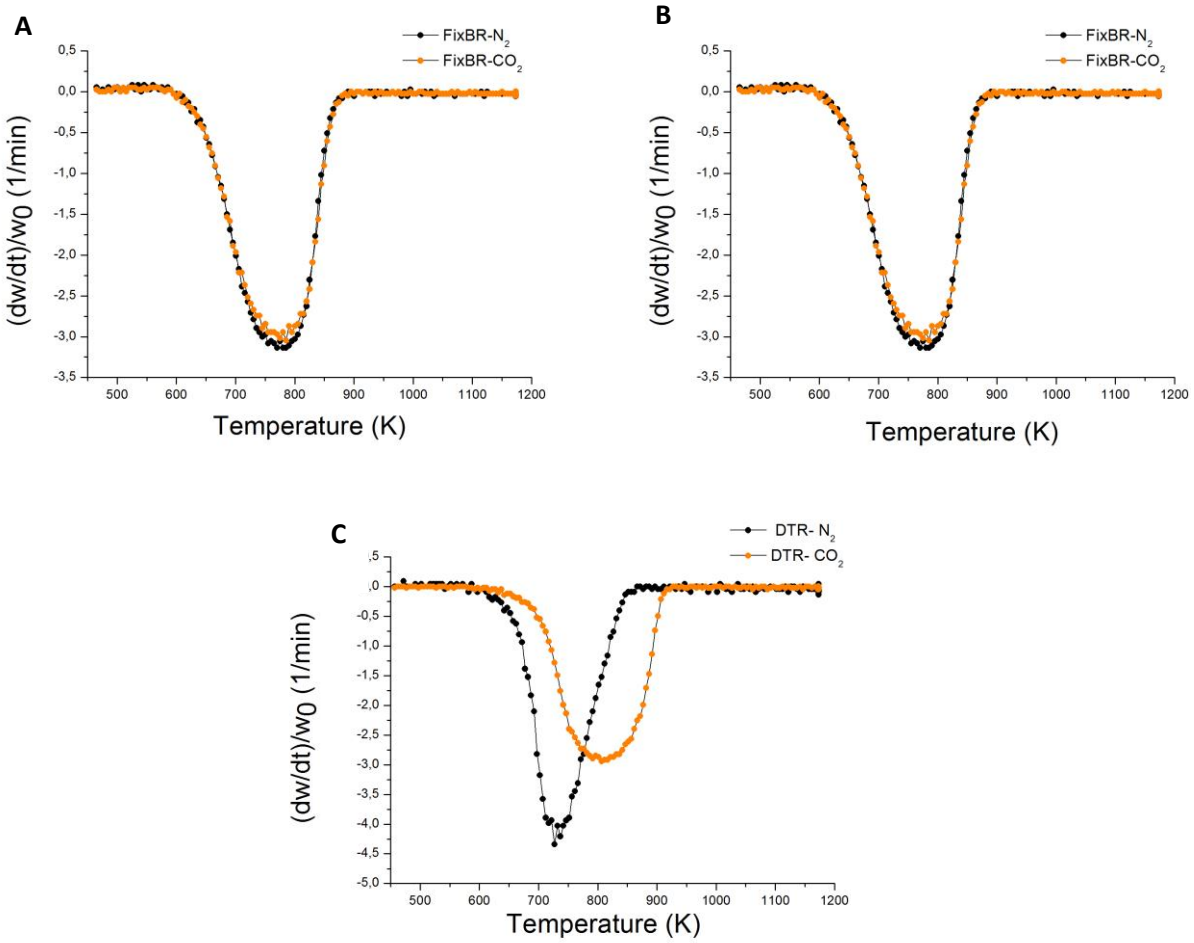

Fig.4.7. DTG plots of the char samples: FixBR (A), FBR (B) and DTR (C).

The effect of N_2 vs. CO_2 rich pyrolysis atmosphere therefore impacts on the residual char reactivity differently according to the reactor conditions. As a consequence, when pyrolysis is carried out in N_2, it can be observed that the values of the DTG peak temperature increase in the order DTR< FixBR<FBR, and, therefore, it can be assumed that combustion reactivity increase with the reverse order. When pyrolysis is carried out in CO_2 a different reactivity order is observed: FixBR>FBR>DTR.

The results of TPD experiments are shown in Fig.4.8 reporting the profiles of CO and CO_2 evolved upon heating in argon as a function of time. CO largely exceeds CO_2 in all the TPDs.

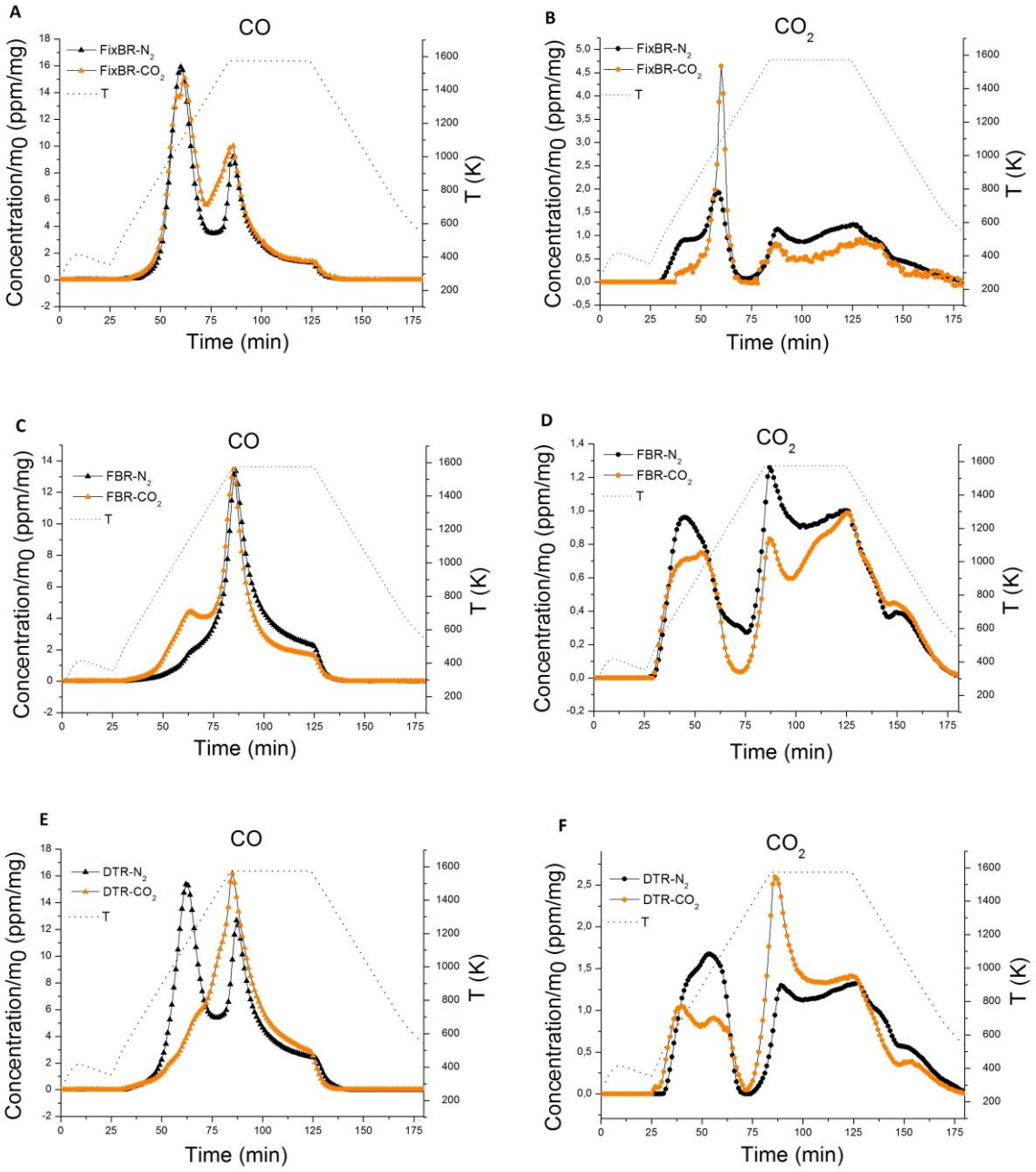

Fig.4.8. Gas evolution of the TPD tests of the char samples: FixBR (A-B), FBR (C-D) and DTR (E-F).

For the FixBR chars, the release of CO occurs in two stages, with a first peak after 35 min at 1110 K and a second one after 60 min at 1570 K. Minor differences are observed in the evolution of CO and CO_2 of the two fixed bed chars (Fig.4.8 A/B). The temperatures corresponding to the TPD peaks are also reported in Table 4.8. The similarity of TPD profiles is consistent with the similarity of the DTG curves and evocative of a similar distribution of active sites with formation of similar C-O complexes on the structure of these chars.

In the FBR-chars, the first CO peak sensibly decreases compared to the fixed bed chars. In fact, it is little pronounced in the FBR-CO_2 char and hardly visible in the FBR-N_2 char. The loss of the first CO peak can be related to the loss of active sites with low activation energy and is consistent with the lower reactivity of FBR chars compared to fixed bed ones. The difference between FBR-N_2 and FBR-CO_2 are of lesser extent and in fact are consistent with the modest differences also observed in TGA combustion tests.

The profiles of the DTR-N_2 char appear similar to those of the fixed bed char, with two pronounced CO peaks. The CO-TPD profile of the DTR-CO_2 char is different from the previous one and resembles more closely the one of the FBR char, with only one major CO peak at 1570 K. The loss of the first peak of the CO profile in the TPD of DTR-CO_2 char suggests that the more active sites, those which are more labile and produce the early CO peak, are lost upon pyrolysis in the drop tube rector with CO_2, but not with N_2. This is consistent with the lower rate of combustion attained for the same sample in TGA.

Results of TGA and TPD analysis are complemented by XPS analysis of the samples. A selection of *O1s* XPS spectra is shown in Fig.4.9. The fitting is based on the deconvolution suggested in *Chapter 2*. Data were fitted using *CasaXPS* software. The presence of three main groups of carbon-oxygen complexes is observed, as already reported in *Chapter 3* for coal chars: 1. C-O-C ether; 2. C=O, C-OH and (H)O-C=O, 3. epoxy. In the fixed bed (low temperature chars), epoxy groups prevail over the other C-O functional groups and very similar results are obtained in the N_2 and CO_2 case. This result is consistent with the high reactivity and the similarity of the FixBR-N_2 and FixBR-CO_2 chars. It is also consistent with the presence of remarkable early TPD peaks. In fact, a direct relationship between reactivity of coal chars and abundance of epoxy groups has been suggested and discussed in *Chapter 3*.

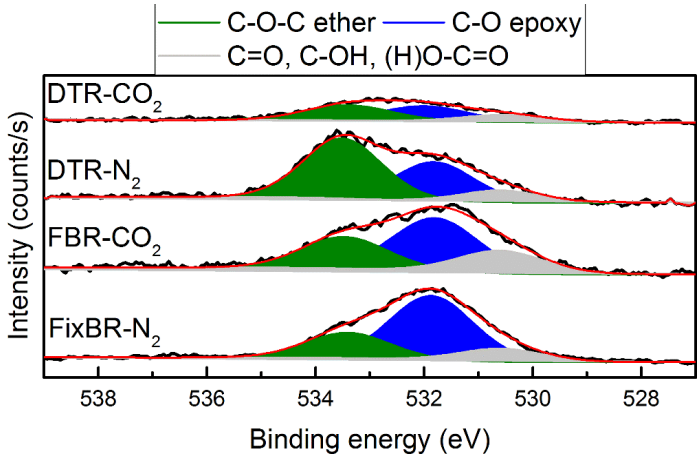

Fig.4.9. *O1s* XPS spectra of selected chars collected in the different test rigs.

A progressive loss of epoxy is observed moving from FixBR-N_2 to DTR-CO_2. Apparently epoxy groups decrease with both temperature and presence of CO_2 in the pyrolysis environment. In the DTR-CO_2 char, however, the very severe pyrolysis conditions apparently reduce the very amount of all oxygen complexes, resulting in the minimum combustion reactivity

Char soot-like separation

In the course of the experimental work regarding the drop tube pyrolysis of coal in N_2 and CO_2, the appearance on the wall of the ceramic filter of a fluffy carbonaceous solid material, different from char collected at the bottom of the ceramic filter was noticed [81]. This phenomenon was more remarkable in CO_2 than in N_2. The soot-like and char fractions had been effectively separated from each other implementing a procedure based on the suspension of raw carbon particulate in ethanol, followed by settling, and decanting [119,192]. The structural characterization of char and soot-like was verified by several chemical and spectroscopic techniques. The soot-like and char samples obtained by means of the procedure described above will be labelled according to the following denominations: (S or C)-(N_2 or CO_2), where S and C identify the soot-like and char fractions, respectively. The samples before separations will be referred as “char+soot-like”.

Table 4.9 reports the separation yields and the percentage distribution of soot-like and char for each particulate sample. Even though some material losses occurred during the collection procedure the recovery was > 90 %.

Table 4.9. Separation yields and the percentage distribution of soot-like and char.

Sample (soot-like + char)	Weight (mg)	Separation yield (%)	Char (mg)	Soot-like (mg)	char (wt%)	soot-like (wt%)
CO_2	86.6	93.9	17.2	64.1	21.2	78.8
N_2	73.0	92.4	35.7	31.7	52.9	47.1

Fig.4.10 shows the DTG curve conducted in air environment, SEM imagine and PDS profile of the sample CO_2 collected on the wall of the ceramic filter. A double step of weight loss can be noticed in the DTG profile confirming the presence of two different components. SEM imagine shows a solid characterized by irregular shape and particle size close to that of the parent coal feed, together with a multitude of submicronic carbon aggregates. Also Laser granulometric analysis, performed on a *Mastersizer 2000* granulometer (Malvern Instruments), gives out a bimodal distribution peaked in the ranges: 26–30 µm and 80–200 nm.

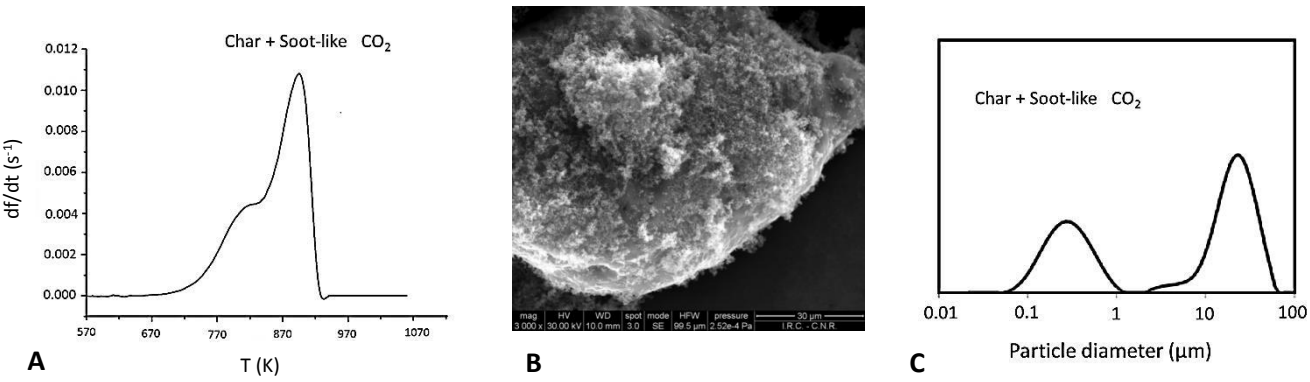

Fig.4.10. A) DTG profile in air environment, B) SEM imagine and C) Particle size volumetric distribution of sample "char + soot-like CO_2" .

The separation efficiency was preliminary checked by means of SEM and DLS. Results are reported in Fig.4.11. SEM imagines show that the top fraction is mainly composed of sub-micrometric particles (left image) with a size distribution peaked around 200 nm in the PSD curve (center of the figure), whereas the bottom fraction is constituted of coarse particles showing an unique peak around 30 µm by granulometry technique. Considering the high sensitivity of the Dynamic Light Scattering in detecting even traces of large size particles (the signal is proportional to the third power of the particle diameter), this large-size peak is actually negligible and due to very few amounts of char particles contaminating the soot-like fraction.

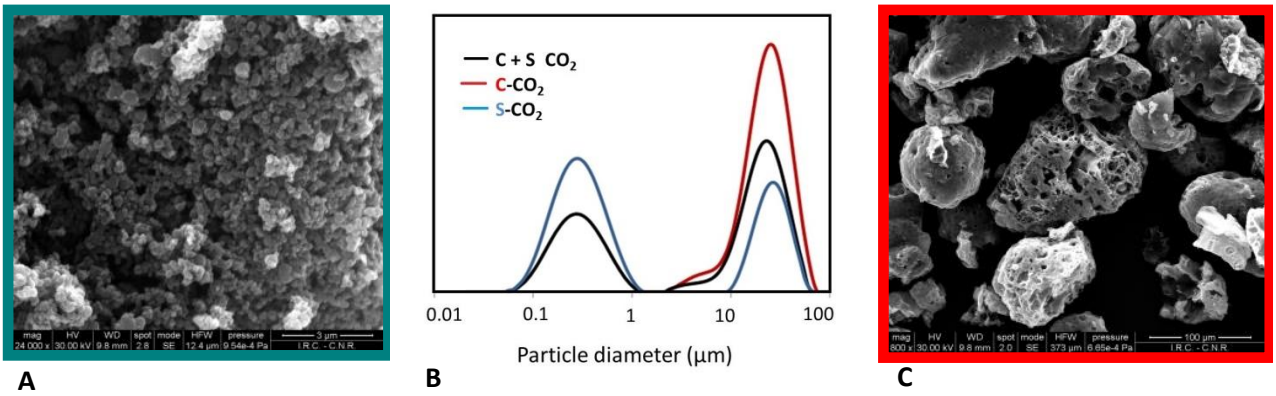

Fig.4.11. A, C) SEM imagines S-CO_2 and C-CO_2. B) Particle size volumetric distribution of "char + soot-like CO_2" S-CO_2 and C-CO_2. .

A single weight loss peaked at about 800 and 880 K, features the DTG profiles of char and soot-like, respectively (Fig.4.12). The higher oxidation temperature of soot-like indicated the lower oxidation reactivity of soot-like in comparison to char. Moreover, a significant residue was left by the char (about 10 %) whereas a negligible residue was left in the case of soot-like sample, indicating that soot-like was ash free. The sample "char + soot-like material" N_2 showed the same trend.

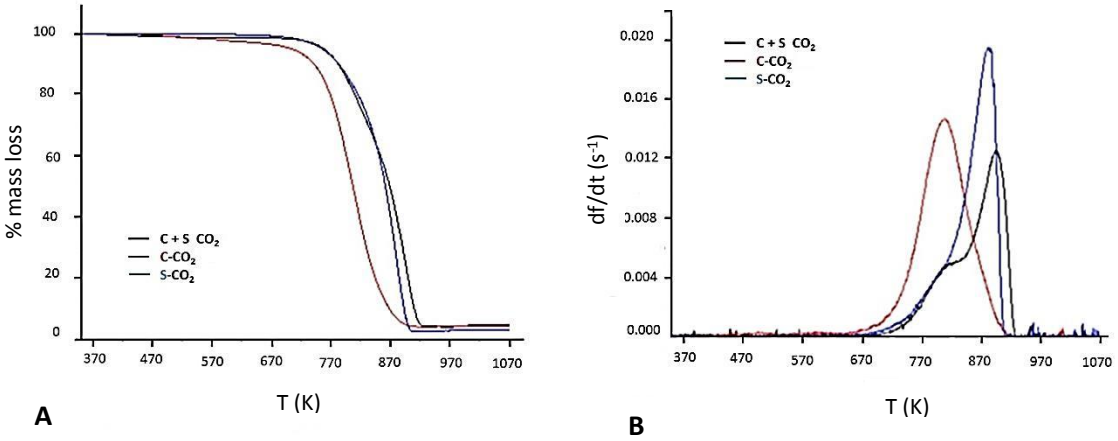

Fig.4.12. A) TG and B) DTG combustion profiles of sample CO_2 collected on wall of the ceramic filter before and after separation procedure.

The temperature corresponding to the DTG peak is reported in Table 4.10 together with the D/G ratio obtained from deconvolution of Raman spectra.

Table 4.10. DTG peak temperature and Raman D/G ratio of samples.

Sample	DTG peak in air (K)	D/G
C- CO_2	809	0.89
S- CO_2	882	0.86
C- N_2	768	0.62
S-N_2	844	0.54

The DTG peak values of soot-like are in general higher than the DTG peak values of the corresponding char samples, indicating that soot-like, as expected, is systematically less reactive than the corresponding char. Moreover, the DTG peak values of the CO_2 samples are higher than those of the N_2 samples, thus that when pyrolysis is carried out in CO_2 the resulting char and soot-like are less reactive.

FTIR spectra show the differences in the abundance of functional groups. FTIR spectra, in the 1800-600 cm^{-1} range, of char and soot-like produced in N_2 and CO_2 are contrasted in Fig.4.13. In particular, both char and soot-like fractions of CO_2 samples present broad and unstructured spectra typical of sp^2 carbon-rich materials. FTIR spectra of both N_2 and CO_2 soot-like samples do not exhibit the typical peaks near 1100 cm^{-1} due to clays and other minerals present in the starting coal. This is in agreement with the absence of residue in the TG oxidative analysis above reported.

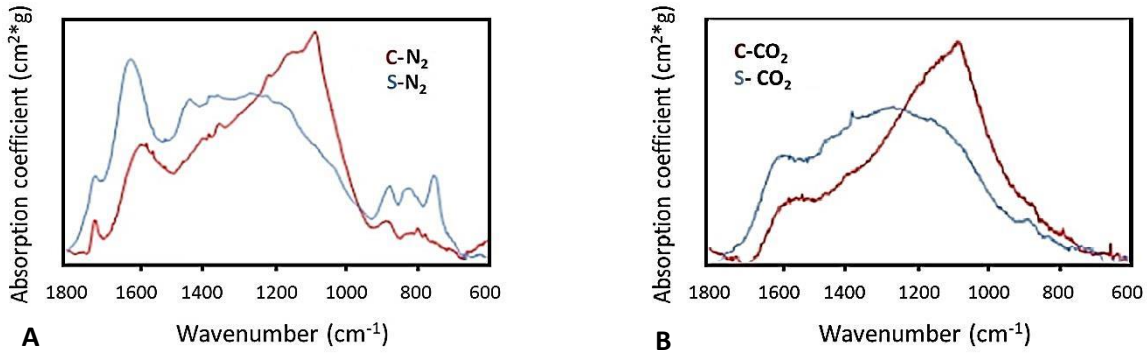

Fig.4.13. Infrared mass absorption coefficients of A) N_2 soot-like and char, B) CO_2 soot-like and char.

The Raman spectra of S-CO_2 and S-N_2 are reported in Fig.4.14A. In disordered nanocrystalline carbon material, the G band arises from small graphitic crystallites, while the carbon atoms at the edges of graphene layers are considered as the most probable origin of the D band [182,183]. The I(D)/I(G)

ratios, evaluated from Raman spectra deconvolution, are reported in Table 4.10 The D (at about 1350 cm^{-1}) and G (at about 1600 cm^{-1}) peaks have been fitted by Lorentian (L) and Breit-Wigner-Fano (BWF) curves, respectively. Two additional L lines were also used to fit the substructures clearly visible on both sides of the D peak (at about 1230 and 1450 cm^{-1}) associated to the merging of different PAH moieties [183]. For highly disordered carbons, characterized by an aromatic cluster size < 2 nm, the I(D)/I(G) ratio increases linearly with the crystal size following the equation proposed by Ferrari et al. [182]. The I(D)/I(G) ratio is about the same for char and soot-like. From the data, the two different fractions have a similar relative degree of order of carbonaceous structure. By contrast, significant differences can be noticed for effect of the CO_2 and N_2 atmosphere. Particularly, a higher I(D)/I(G) ratio, i.e. a higher aromatic extension, is noticeable in the CO_2 samples.

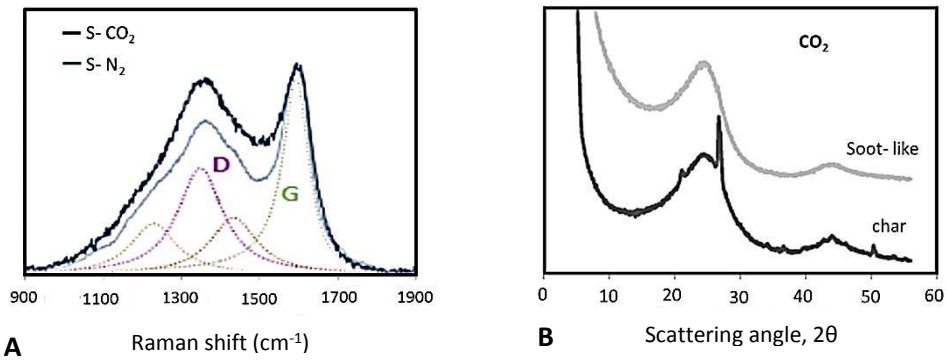

Fig.4.14. A) Raman spectra of S-N_2 and S-CO_2 and deconvolution of S-N_2 spectrum. B) XRD patterns of CO_2 soot-like and char samples.

The XRD spectra of char and soot-like from CO_2 sample are reported in Fig.4.14B. Two broad peaks in the regions around 2θ =25° ((002) and γ bands) and 43° ((10) bidimensional reflection) are present both for char and soot-like. In agreement with Raman analysis, no substantial differences are notable in the carbonaceous matrix. However, char spectrum presents ash at 2θ = 20°, 28° and 50°, which are completely absent in the soot-like spectrum.

DTR char reactivity

Samples pyrolyzed in DTR by ***path A*** have been subjected to isothermal (TGI) and non-isothermal (TGNI) thermogravimetric experiments carried out with $O_2/CO_2/N_2$ atmospheres with the aim of assessing the intrinsic kinetics of the chars with O_2, CO_2 and mixtures of O_2/CO_2 (*regime I*) (***path A+B).*** Fig.3.15 reports the curves of normalized conversion rate from TGA experiments on previously prepared chars, according to ***path A+B*** in Fig.4.1. It can be noted that the plots relative to all TGA combustion experiments at different temperatures overlap with each other and the resulting curve passes through a maximum at conversion values around $f = 0.3$. The plots relative to CO_2 char experiments at different temperatures also overlap with each other resulting in a curve which, after the first 10% of conversion, is monotonously decreasing. These trends resemble the trends in the N_2 and CO_2 surface areas reported in Fig.4.17. Curves have been fitted by polynomials, providing expressions $Y(f)$ reported in Fig.4.15.

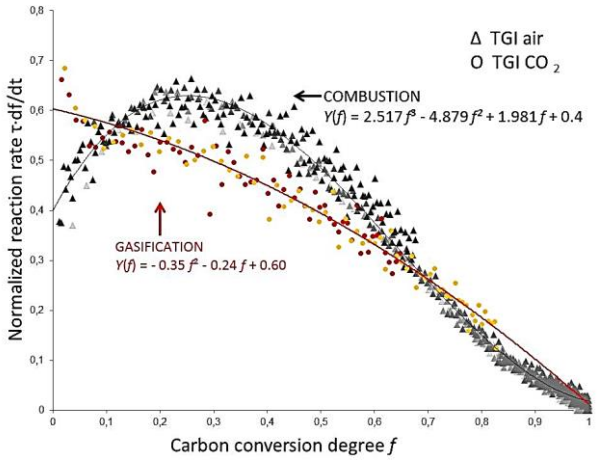

Fig.4.15. Evolution of reaction rate with conversion during TGI CO_2 and TGI air experiments. Data obtained at different temperatures (1073-1173 K and 623-748 K) are shown with different shades of red (TGI CO_2) and grey (TGI air).

It can be recalled that maxima in the curves of instantaneous conversion rate are well documented in the literature in the case of combustion of coal and biomass chars. This phenomenon was attributed to evolution of internal porosity along burn off. It was described by models such as Bhatia and Permutlers random pore model [194]. Accordingly, in the early stages of combustion, pores will open up making additional surface area available for reaction, while at large conversion degree the collapse of pores will induce a progressive reduction of combustion rate. Monotonously decreasing curves of

instantaneous conversion rate have been reported instead for gasification of chars with CO_2 and H_2O [195]. In fact, also the extent and pattern of pore activation has been reported to be remarkably different in gasification compared to combustion [9]. In particular, micropores are more extensively activated by carbon dioxide than by oxygen [9].

The Arrhenius plots obtained from non-isothermal and isothermal experiments are reported in Fig. 4.16. It can be observed that the agreement between isothermal and non-isothermal results is good. For the char-CO_2 reaction, both DTR N_2 and DTR CO_2 chars exhibit linear Arrhenius plots in the temperature range investigated. On the contrary in air and oxy30 atmospheres, Arrhenius plots are linear only in the low temperature range. The kinetic parameters for the char-CO_2 reaction have been obtained from regression of the experimental Arrhenius plot over the entire temperature range, while the kinetic parameters for the char-O_2 reaction have been obtained by regression over the low temperature, linear region of the plot. Results are reported in Table 4.11.

When we compare the kinetic parameters obtained for the DTR N_2 and DTR CO_2 chars, we notice that the values of the pre-exponential factors are always higher for the DTR N_2 chars compared to the DTR CO_2 chars, whereas the values of activation energy are the same and in the order of those reported in the literature [196]. The ratio of the pre-exponential factors therefore gives the relative scale of reactivity of the chars, accordingly DTR N_2 chars are more reactive than DTR CO_2 chars by a factor of 7 towards oxygen and by a factor of 2 towards carbon dioxide. It is recalled that this result refers to a case of ***path A+B*** of the scheme in Fig.4.1.

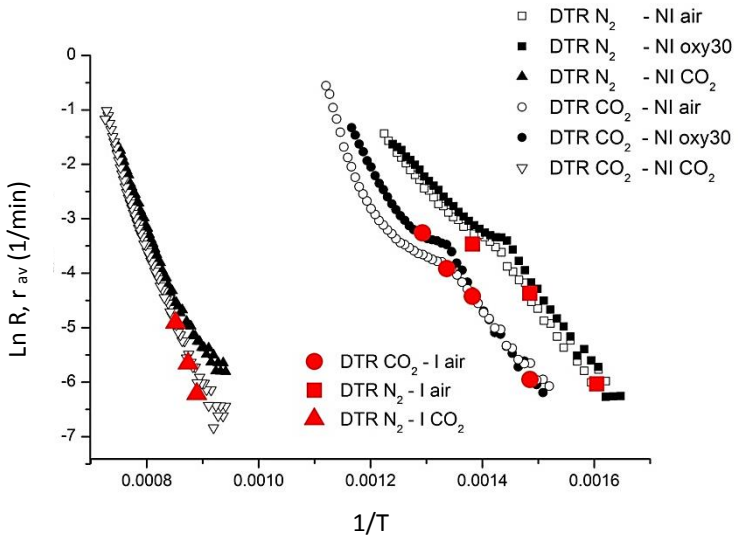

Fig.4.16. Arrhenius plots of the TGNI and TGI tests in different atmospheres of the DTR N_2 and DTR CO_2 chars.

Table 4.11. Results of the fitting of Arrhenius parameters to the data from TGNI tests.

Reaction	DTR N_2 char		DTR CO_2 char		Reactivity ratio DTR N_2/ DTR CO_2
	E_a (kJ/mol)	$k_0 \cdot p_i^n$ (min^{-1} bar^{-1})	E_a (kJ/mol)	$k_0 \cdot p_i^n$ (min^{-1} bar^{-1})	
CO_2	234.5	$3.0 \cdot 10^8$	234.5	$2.0 \cdot 10^8$	2
air	146.5	$3.2 \cdot 10^9$	146.5	$4.5 \cdot 10^8$	7
Oxy 30	146.5	$4.5 \cdot 10^9$	146.5	$4.5 \cdot 10^8$	10

The pyrolysis atmosphere significantly affects the char formation (and soot-like samples). The rate of combustion, (oxy-)combustion and gasification of the DTR char prepared in CO_2 result to be low compared to char prepared in N_2, under *regime I* conditions (***path A+B***) .

The morphology of DTR N_2 and DTR CO_2, observed by SEM is similar, and the BET surface area is modest for both chars, the difference in reactivity between the two chars seems to correlate well with differences in the C-O functionalities which reside on their surface, as detected by XPS. The difference in reactivity may be correlated to the different extent of *thermal annealing* in CO_2. Arrhenius parameters are in agreement with results found by Salatino et al. [85] where thermal annealing mostly affected the pre-exponential factor rather than the activation energy.

.

4.3.2. Evolution of carbon structure in oxyfiring conditions

Under oxidizing atmosphere, coal particles do not experience only pyrolysis, but also the early stage of heterogenous combustion. Coal was fed to the DTR in O_2/CO_2 and O_2/N_2 atmospheres [81] in order to investigate the fate of coal in atmospheres typical of air and oxy-fuel combustion under *regime II* conditions, when pyrolysis, and the early stage of combustion and gasification potentially overlap, which correspond to ***path C*** in Fig.4.1.

Table 4.12 and 4.13 summarise the results of the main analyses on the chars collected during the different DTR experiments either of pyrolysis or (oxy-)combustion.
The values of M_i, f have been calculated according to eqs. 4.3-4. Pyrolysis was completed both in the DTR N_2 and DTR CO_2 experiments. The difference between the two chars in terms of ash content is small and suggests that char gasification in CO_2 environment was limited. A carbon conversion degree of less than 7% can in fact be attributed to gasification. Under oxidizing conditions, a significant extent of char conversion is instead attained, f reaching a value of 75% in the DTR oxy30 experiment. This strongly supports the idea that CO_2 contributes to higher carbon conversion degree. Notably in this set of (oxy-)combustion experiments, carbon conversion followed ***path C*** of Fig.4.1.

Table 4.12. Rate of char conversion from DTR experiment sand samples analyses.

Sample	**Atmosphere** (vol%)	***a*** [1,4] (wt%)	***M*** [2,4] (wt%)	***f*** (1)	**H** (wt%)	**O** [3] (wt%)
raw		4.8			5.1	12.3
DTR N_2	N_2	9.4	51		2.0	4.5
DTR CO_2	CO_2	10	55	0.07	0.8	4.9
DTR air	21 O_2/N_2	12	63	0.24	0.4	4.1
DTR oxy21	21 O_2/CO_2	17	75	0.49	0.3	13.2
DTR oxy30	30 O_2/CO_2	29	88	0.75	0.2	2.3

[1] dry basis; [2] dry and ash free basis; [3] calculated by difference; [4] taken by [81].

Table 3.13. DTR samples analyses.

Sample	N_2-BET[4] (m^2/g)	CO_2-DR-K (m^2/g)	He density (g/cm^3)
raw	2.3	153	1.37
DTR N_2	1.1	410	1.70
DTR CO_2	6	406	1.65
DTR air	62	306	1.93
DTR oxy21	78	260	n.d.
DTR oxy30	42	167	2.14

[1] dry basis; [2] dry and ash free basis; [3] calculated by difference; [4] taken by [81].

Notably in chars prepared in pure N_2 and CO_2 the ash content is around 9–10 wt%, which holds for a conversion of the coal *M* of approximately 50 wt%. This result suggests that volatile release in the DTR pyrolysis experiments exceeds the volatile content of the raw coal measured by proximate analysis by 10 wt% points. This result confirms that the residence time in the reactor was appropriate to bring the pyrolysis process to completion. The larger ash content in char samples collected from DTR experiments with air and oxy21 mixtures suggests the onset of char combustion. The extent of char burnoff is maximum in the char prepared with oxy30 which has in fact the highest ash content.
In Fig.4.17 the *O* and *H* contents and the surface areas have been plotted as a function of the char conversion degree *f*. It must be specified that the *H* content was measured directly by the CHN analyser, whereas the *O* content was estimated by difference. Moreover, the different conversion degrees *f* was attained in the DTR by changing the gas composition at fixed residence time, not vice-versa. However, the plot shows that the porous structure parameters and chemical composition of the chars change remarkably with conversion, whereas the differences between the chars prepared in N_2 and CO_2 are modest. As shown in Fig.4.17, the N_2 surface area of the merely pyrolyzed samples (DTR N_2 and DTR CO_2) is low, whereas the CO_2 surface area is already quite large (2.8 larger than that of the raw coal). The N_2-BET surface area, which can be attributed to mesopores, increases in the range of char conversion degree f = 0-0.5 and decreases afterwards as well as the oxygen content. The trend confirms the important activation of mesoporosity upon reaction with O_2 as a consequence of internal burning.

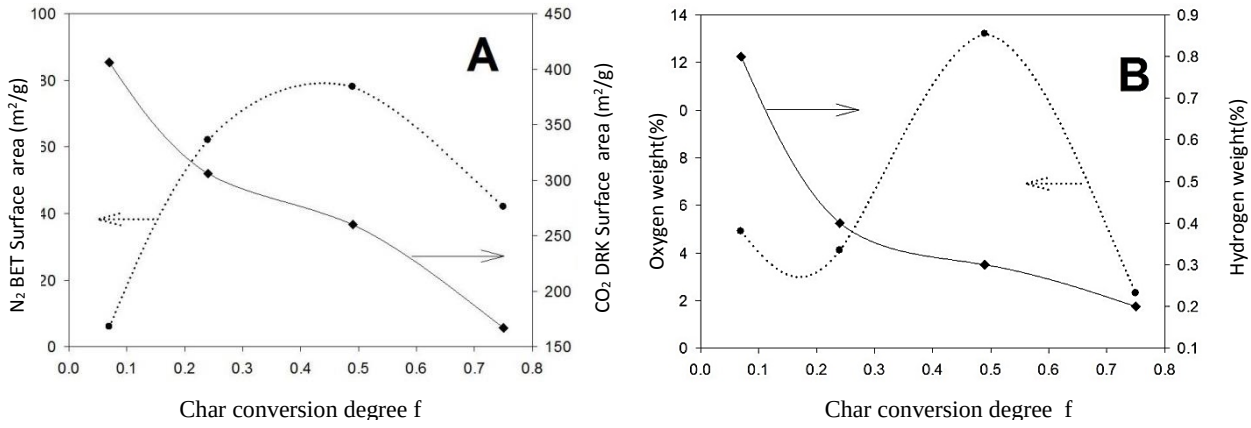

Fig.4.17 Surface areas (A), oxygen and hydrogen content (B) of the different DTR chars as a function of the char conversion degree attained in the DTR reactor (dotted: N_2 BET and hydrogen, drawn: CO_2 DR-K and oxygen).

In the DTR air and DTR oxy21/30 chars, where high char conversion degree is attained, large macropores show up, as a consequence of enlargement of mesopores and transition into the macropore class.

The CO_2 surface area which can be associated to microporosity decreases instead with char conversion. CO_2 surface areas have been calculated by the DR-K theory.

It can be observed that a monotonously decreasing trend with conversion is registered also for the hydrogen content of the chars. Moreover, it can be observed from Table 4.13, that the true char density, determined with helium buoyancy measurements, increases progressively upon pyrolysis and char conversion going from the value of 1370 kg/m³ measured for the raw coal to the value of 2100 kg/m³ measured for the DTR oxy30 char. The decrease of micropore volume and the increase of sheletal density was found to be paralleled by carbon burn off and deactivation by thermal annealing [13]. The structure of the chars can also be analyzed from the XRD spectra reported in Fig.4.18A. In the present chars, the (002) and (10) reflections are not very pronounced, suggesting little graphitic order for most of the samples. However, the char with the comparatively most intense (002) and (10) reflections is the one prepared in CO_2 atmosphere. In the DTR oxy21/30 chars, the (002) and (10) reflections become very shallow, while the peaks corresponding to inorganics are sharp, probably because of the high degree of carbon consumption and the large ash content. Further analysis of chars by XPS is presented in Fig.4.18B and 4.19A-B. The C1s spectra of all chars have been fitted with seven components, as exemplified in Fig.4.18B.

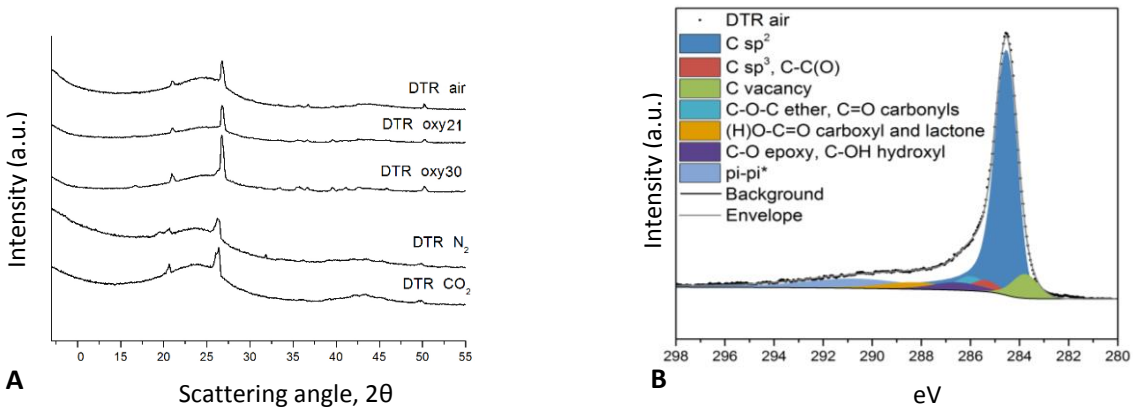

Fig. 4.18. A) XRD patterns of all collected DTR chars (T_w = 1573 K). B) Deconvolution of C1s signal of DTR air (T_w = 1573 K, air) exemplarily for all chars.

The fitting is based on the deconvolution suggested in *Chapter 2*. Fig.4.19 reports the relative quantities of main functional groups obtained from the fitting of the *C1s* spectra. Fig.4.19A discloses the functionalities related to the carbon fine structure of the chars. It can be observed that the sp^2 hybridized carbon component dominates in all samples. Along with carbon conversion, therefore moving from the DTR N_2 and DTR CO_2 to the DTR air, DTR oxy21 and DTR oxy30 chars, sp^2 hybridized carbon decreases, while the carbon vacancies increase. The component attributed to π-π* shake-up increases, a phenomenon which could be related with carbon densification. It can be observed that the increase of π-π* functionalities in XPS and the progressive loss of sp^2 hybridized carbon couple with the loss of microporosity and increase of helium density. Fig.4.19B focuses on carbon-oxygen complexes. It can be observed that the overall fraction of carbon-oxygen groups is significantly higher in all chars prepared in O_2 containing atmospheres compared to the chars prepared in N_2 and CO_2. It is quite interesting to note the differences between the samples which have been exposed to CO_2 rich atmospheres compared to samples which have been prepared in N_2 rich atmospheres as regards the nature and distribution of C-O complexes: carboxyl and lactone are in fact more abundant in the DTR CO_2 compared to the DTR N_2 char and in the DTR oxy21 compared to DTR air char. The idea that CO_2 is incorporated in the incipient char structure in the form of lactones is supported by computational studies based on quantum chemistry [197]. In DTR oxy30 the oxygen functionalities decrease probably because of the high degree of carbon consumption.

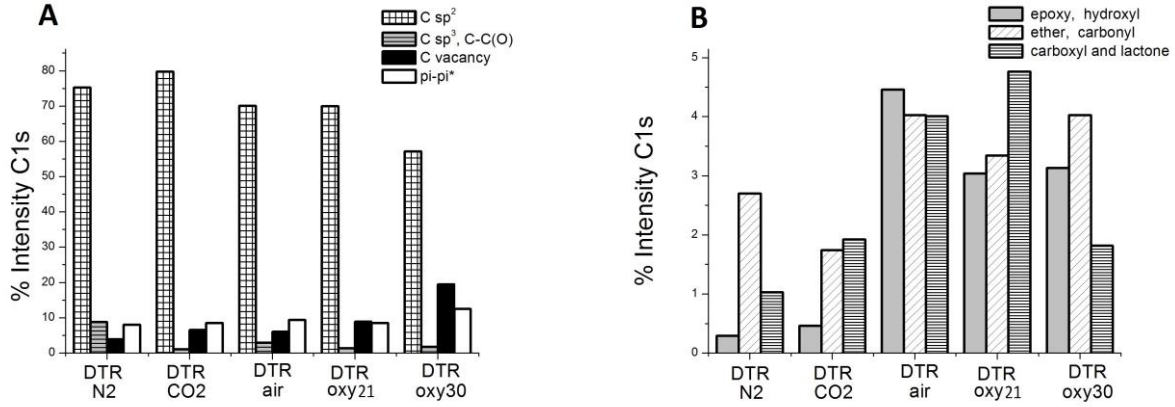

Fig.4.19. Fractions of functional groups in the DTR chars determined by deconvolution of C1s signal from XPS. A: Functionalities related to the carbon fine structure; B: Carbon-oxygen complexes. Components sum up to 100 %).

Altogether, the analyses suggest the existence of a link between mesoporosity, carbon-oxygen complexes on one side, microporosity, order of the carbon structure, aromatization and CO_2

gasification rate on the other. A key to explain differences in the structural modifications of chars in oxygen and carbon dioxide may be found in the local electronic properties of carbon materials [198-200]. Within this framework, the micropore walls can be identified with turbostratic lamellae and are regions with high density of delocalized π electrons, while mesopores can be identified with voidages between randomly oriented turbostratic domains. As such the finest pores are characterized by relatively low concentration of sites active towards O_2, on the contrary, edge carbon atoms and inorganic catalytic sites should lie preferentially on the surface of meso- and macropores and should be more reactive than micropores.

It can be observed that the increase of π-π* functionalities in XPS, the progressive loss of sp^2 hybridized carbon, the decrease of H content, coupled with the loss of microporosity and increase of helium density, typical of chars prepared under (oxy-) combustion condition in DTR, suggest an enhanced degree of char graphitization and higher extent of thermal annealing.

Without consideration of mass transfer limitation, is not possible to evaluate oxy-combustion rete under *regime II* conditions typical of ***path C.***

However, chemico-physical analysis shows that the presence of carbon dioxide in the early stages of (oxy)-combustion affected the quality of the newly formed chars in the DTR.

Analysis suggests that transformations/thermal annealing are more remarkable in the DTR oxy21/30 than DTR air. It seems that a larger extent of char conversion has occurred. A possible reason is the larger extent of heterogeneous reactions (combustion and gasification) in CO_2 rich atmospheres. It is quite interesting to note the differences between the samples which have been exposed to CO_2 rich atmospheres compared to samples which have been prepared in N_2 rich atmospheres as regards the nature and distribution of C-O complexes: carboxyl and lactone are in fact more abundant in the DTR CO_2 compared to the DTR N_2 char and in the DTR oxy21 compared to DTR air char. XPS analysis supports the results found of Borrego et al. in [120], suggesting that CO_2 could be involved in some cross-linking reactions during incipient char formation which would also reduce particle swelling.

4.4 Conclusions

Pyrolysis and char combustion have been investigated separately, by pyrolyzing coal in three different reactors with N_2 or CO_2 (***path A***) [82,192] and later on measuring the reactivity of the DTR chars (***path B***).

Substitution of N_2 with CO_2 during pyrolysis of coal in different test rigs produced different results. Microstructural properties and combustion reactivity of chars prepared in the fixed bed reactor (FixBR) are not affected by CO_2 vs. N_2 atmosphere. However, pyrolysis in CO_2 produces more aromatic tars than pyrolysis in N_2, with the formation of a soot-like particulate clogging the filter of the FixBR.

Heat treatment by itself seems to be insufficient to reduce severely the char reactivity, which in the DTR-N_2 char is still comparable with those of the FixBR. Instead, when pyrolysis is carried out with CO_2, char reactivity decreases severely and XPS and TPD analysis confirm the loss of the more labile C-O functionalities available on the char surface. The formation of soot-like is emphasized in the DTR-CO_2 experiments.

In FBR experiments, the temperature of pyrolysis was lower than the DTR by 100 K (1473 K vs. 1573 K) but the residence time was longer by two orders of magnitude. Under such long residence time, not only pyrolysis is complete, but also char annealing takes place. Apparently, the long residence time in the FBR, levels off the differences of structure and reactivity between FBR chars.

In DTR experiments, a much larger production of soot-like in CO_2 was documented [81]. What emerged is that such fine carbon particulate is mostly ash-free, suggesting that its formation occurs in the gas phase. As regards the different reactivity, soot-like turned out to be less reactive than the corresponding char, even though the carbonaceous network of soot-like and char as measured by Raman and XRD appeared similar. Both Char and soot-like samples produced in CO_2 show higher aromatic extension.

DTR chars have been analyzed separately by mean of combustion experiments in the TGA (under *regime I* condition) according to ***path A+ B***. The CO_2 chars resulted to be less reactive than the N_2 chars by one order of magnitude in combustion, oxy combustion and gasification TGA experiments. The difference in reactivity between the two chars seems to correlate well with differences in the C-O functionalities which reside on their surface, as detected by XPS.

Coal (oxy-) combustion experiments have been carried out in the DTR in air and oxy-atmospheres, without separating the pyrolysis and the char combustion stage according to ***path C***. Chemico-physical analysis shows that the presence of carbon dioxide in the early stages of (oxy)-combustion affected the quality of the newly formed chars in the DTR, suggesting an enhanced degree of char burn out and graphitization. A possible reason is the larger extent of heterogeneous reactions in CO_2 rich atmospheres, in contrast with the results found in TGA combustion experiments. XPS analysis supports the hypothesis that CO_2 could be involved in some cross-linking reactions enhanced by the formation of carboxyl and lacton functional groups during incipient char formation and combustion in CO_2-rich atmosphere.

Chapter 5

General conclusions

This Thesis project aimed at giving a contribution to further unravel selected aspects of the chemistry and physics of carbon combustion and gasification relevant to implementation of novel clean coal technologies for **C**arbon **C**apture and **S**torage (CCS)-ready conversion. Aspects that have been specifically scrutinized are: a) deeper understanding of the interaction between solid carbon and oxygen, with a focus on the role, chemical nature and transformations of surface oxides as intermediates of carbon combustion and gasification (***Chapter 3***); b) characterization of the chemical and physical nature of chars generated upon devolatilization of coal under oxyfiring conditions (i.e. atmospheres with excess oxygen and large CO_2 partial pressures) and its impact on reactivity in heterogeneous gasification reactions (***Chapter 4***).

The chemical nature of the carbon–oxygen complexes on the surface of solid carbons was investigated with reference to a char from medium-rank coal (South African). To characterize the thermal stability of functional groups upon oxidation at different temperatures, char samples have been oxidized in thermobalance a flux of air between 300 and 1000 K and analyzed using Temperature Programmed Desorption Technique. The chemical nature of carbon-oxygen functionalities has been clarified by means of high-resolution XPS measurements performed at the SuperESCA beamline of Elettra synchrotron radiation facility. *C1s* and *O1s* core-level spectra were acquired on the surface of the samples after oxidation under a flux of air between 500 and 1000 K. Deconvolution of the core-level spectra by curve fitting enabled to infer the chemical structure of the samples in terms of extension of sp^2 carbon hybridization, abundance of in-plane vacancies, extension of π conjugation and chemical nature of carbon-oxygen functionalities. Correlating thermoanalytical and structural (XPS) characterization, suggests the effect of temperature of oxidation on the nature of the carbon–oxygen complexes. In particular, deconvolution of the *O1s* spectra provides valuable clues on epoxidation as being the prevalent type of oxygen functionalization when oxidation is performed at low temperature (early stage of oxidation). TPD measurements show that the amount of surface oxides responsible of the desorption of CO-CO_2 increases, when expose to oxygen is

performed at temperature up to 700 K. At the same time, *O1s* spectra show a more pronounced increase in the number of ether and carbonyl bonds. This observation suggests that the rearrangement of the C–O bonds takes place during oxidation up to 700 K. The results are consistent with a mechanistic semi-lumped kinetic model based on four steps: formation of 'metastable' surface oxides by oxygen chemisorption, rearrangement of metastable oxides into stable complexes either by thermally activated rearrangement/isomerization or by complex-switch-over driven by molecular oxygen, desorption of surface oxides with release of CO and CO_2 [145]. Altogether TPD and XPS characterizations, suggest that the "metastable" oxides may prevailingly consist of epoxy functionalities, whereas the more stable oxides would be composed by ether and carbonyl moieties. At higher temperatures, and upon extensive oxidation (in partucular: T≈ 700 K, $f \approx 20$), "metastable" surface oxides (epoxy) evolve into more stable carbon-oxygen complexes (ether, carbonyl). When oxidation is performed at T ≥ 800 K, the desorption of functional groups has already happened, leaving a low amount of surface oxides (mainly epoxides). In addition, experimental results suggest that the interaction of the epoxy groups with the other surface oxides (ether, carbonyl) could explain the enhanced evolution of CO-CO_2 in TPDs when expose to oxygen is performed at temperature up to 700 K and $f \approx 20$. In particular, the ratio between carbonyl/epoxy and ether-hydroxyl/epoxy could promote the removal of C atoms from the C and back bone as results of CO/CO_2 evolution. Results are helpful not only in view of applications to stationary combustion or gasification of carbons, but also to shed light on the dynamical patterns of carbon chemisorption/desorption under alternating oxidizing conditions, relevant to "looping combustion" of carbon, as in the "Carboloop" concept proposed by the Naples group. In fact, thermally activated rearrangement/isomerization or complex-switch-over driven by molecular oxygen of surface oxides, are the very key points of the Carboloop process. Senneca and Salatino [145,169] have shown that the combined reactions yielding desorption of surface oxides in the temperature range 723–1723 K were overall exothermic, at odds with the endothermic behaviour that would be expected for the simple process of CO and CO_2 abstraction from oxidized carbon. This finding may be explained on the basis of XPS results of the present work that confirm rearrangement of surface oxides (epoxy) upon thermal treatments and, moreover, the importance of evolution of epoxy group into more stable surface oxides (by complex-switch-over driven by molecular oxygen) when oxidation is performed up to 700 K. Experimental results are encouraging as regards the viability of the Carboloop concept and are in substantial agreement with semiglobal reaction scheme that was assumed as the reference [145], and provide additional insight

into the role of the individual reaction steps. Further investigation will be directed to support and confirm these conclusion by means of experiments under dynamic conditions, to fully assess the potential of the CarboLoop concept with reference to other fuels or operating schemes, to address the issues associated with energy integration within the process.

Along a different path, it is recognized that coal combustion is significantly changed in CO_2-rich atmospleres as oxyfiring. The specific focus of the present study was the effect of devolatilization of coal particles in CO_2 enriched atmospheres on the properties and reactivity of the resulting char. Pyrolysis and char combustion have been investigated separately, by pyrolyzing coal in three different reactors with N_2 or CO_2 (***path A***) [82,192] and later on measuring the reactivity of the DTR chars (***path B***). Substitution of N_2 with CO_2 during pyrolysis of coal in different test rigs produced different results. It can be observed that when pyrolysis is carried out in the fixed bed reactor (FixBR) at 873 K, pyrolysis is hardly complete. Microstructural properties and combustion reactivity of FixBR chars are not affected by CO_2 vs. N_2 atmosphere. However, some differences are observed in the tar samples: pyrolysis in CO_2 produces more aromatic tars than pyrolysis in N_2. During experiments in CO_2 phenomena like clogging of the filter and formation of a soot-like particulate are reported. The pyrolysis degree is highest when pyrolysis is carried out in the DTR at 1573 K. Because of the very short residence times, the extent of annealing and char gasification is limited. Heat treatment by itself seems to be insufficient to reduce severely the char reactivity, which in the DTR-N_2 char is still comparable with those of the FixBR. A remarkable change is observed instead when pyrolysis is carried out with CO_2: in this case, char reactivity decreases severely and XPS and TPD analysis confirm the loss of the more labile C-O functionalities available on the char surface. The formation of soot-like is emphasized in the DTR-CO_2 experiments. In FBR experiments, the temperature of pyrolysis was lower than the DTR by 100 K (1473 K vs. 1573 K) but the residence time was longer by two orders of magnitude. Under such long residence time, not only pyrolysis is complete, but also char annealing takes place. In fact, the structure of the chars at XRD appears more graphitized, and the more labile C-O complexes/active sites available on the char surface are lost. The combustion reactivity is consistently lower than in the FixBR chars. It may be observed that the FBR-CO_2 char has comparable reactivity than the FBR-N_2. Apparently, the long residence time in the FBR, levels off the differences between N_2 and CO_2. Another interesting result is the formation of soot-like particles. The presence of soot-like material inside the tar has been observed already at the farly low temperatures of the FixBR experiments in CO_2. The tar itself was more aromatic and heavy than in

N_2 pyrolysis experiment, clogging the filters before gas analysis. In DTR experiments, a much larger production of soot-like in CO_2 was documented [81]. What emerged is that such fine carbon particulate is mostly ash-free, suggesting that its formation occurs in the gas phase. As regards the different reactivity, soot-like turned out to be less reactive than the corresponding char, even though the carbonaceous network of soot-like and char as measured by Raman and XRD appeared similar. Both Char and soot-like samples produced in CO_2 show higher aromatic extension. In FBR experiments, soot-like was not collected neither was tar. Nevertheless, the qualitative information emerging from SEM is that the particle amounts of soot-like presence is particularly relevant in the CO_2 experiments. DTR chars combustion experiments have been analyzed separately in the TGA (under *regime I* condition) according to ***path A+ B***. The CO_2 chars resulted to be less reactive than the N_2 chars by one order of magnitude in combustion, oxy combustion and gasification TGA experiments. The morphology of the two chars, observed by SEM is similar, and the BET surface area is modest for both chars, the difference in reactivity between the two chars seems to correlate well with differences in the C-O functionalities which reside on their surface, as detected by XPS. Coal (oxy-) combustion experiments have been carried out in the DTR in air and oxy-atmospheres, without separating the pyrolysis and the char combustion stage according to ***path C***. Chemico-physical analysis shows that the presence of carbon dioxide in the early stages of (oxy)-combustion affected the quality of the newly formed chars in the DTR. It can be observed that the increase of π-π^* functionalities in XPS, the progressive loss of sp^2 hybridized carbon, the decreasing of H content, couple with the loss of microporosity and increase of helium density, suggest an enhanced degree of char burn out and graphitization. A possible reason is the larger extent of heterogeneous reactions in CO_2 rich atmospheres, in contrast with the results found in TGA combustion experiments. In fact, the char produced in CO_2 was found to be less reactive in (oxy-) combustion than char produced in N_2 in (air) combustion. XPS analysis supports the hypothesis that CO_2 could be involved in some cross-linking reactions enhanced by the formation of carboxyl and lacton functional groups during incipient char formation and combustion in CO_2-rich atmosphere. Without consideration of mass transfer limitation, it is not possible to evaluate oxy-combustion rate under *regime II* conditions typical of pulverized coal-fired boilers, a feature that requires that experiments be carried out under realistic conditions. Further work is required to elucidate annealing, fragmentation, swelling and shrinking/densification phenomena in CO_2 rich atmospheres relevant to oxy-combustion.

Appendix I

Elettra synchrotron lightsource

Elettra is a third generation storage ring that has been in operation since October 1993. The synchrotron facility is located in Basovizza, on the outskirts of Trieste (Italy), very close to the Slovenian border.

Synchrotron radiation is produced when electrons travelling at relativistic speeds are deflected in magnetic fields. A storage ring is a special type of synchrotron in which the kinetic energy of the particles is kept constant. Electrons circulating in the storage ring at nearly the speed of light provide high-intensity, ultra-bright radiation from the infrared to hard x-rays range when passing through different magnetic devices such as undulators, wigglers and bending magnets.

The Elettra storage ring is made up of four types of magnets: bending magnets that deflect the circulating electron beam into a closed circular path, quadrupoles that focus the beam, sextupoles that compensate chromatic and non-linear effects and steerer magnets that perform small adjustments to the circular trajectory. The arrangement of magnets forms a lattice of magnetic confinement elements. The ring is made up of twelve identical groups of magnets forming a ring roughly 260 m in circumference. What makes it a third-generation synchrotron is the presence along the magnets lattice of the so called insertion devices; these are the principal sources of high brightness photons and are composed of arrays of magnetic poles that force the circulating electrons along serpentine trajectories. Insertion devices are permanent magnets which can produce linear or circular polarised light. The wavelength of the light is tuneable by changing the magnetic field acting on the electron beam by varying the distance between the top and bottom magnet arrays. One of these insertion devices is used for injecting electrons into the storage ring; while the others power beams that propagate through beamlines to reach experimental stations where an array of different analytical and processing techniques (such as for example **S**mall **A**ngle **X**-ray **S**cattering SAXS, X-Ray Diffraction XRD, X-Ray Fluorescence, Synchrotron Infrared Source for Spectroscopy and Imaging SISSI, High resolution core-level photoemission spectroscopy (HR-XPS**))** is available. The resulting light, ten billion times brighter than that supplied by conventional sources, enables scientists to conduct advanced research experiments in the fields of solid state physical-chemistry, biology, life sciences, environmental science, medicine.

Elettra synchrotron operates routinely at two different electron energies: 2.0 GeV for enhanced extended ultraviolet performance and spectroscopic applications, and 2.4 GeV for enhanced x-ray emission and diffraction applications. The ring provides the beamlines with photons in the range from a few to several tens of KeV with spectral brightness of up to 10^{19} photons/s/mm^2/mrad^2/0.1%bw, where the unit of measurements for brilliance takes into account: the number of photons produced per second, the angular divergence of the photons, the cross-sectional area of the beam and the the photons falling within a bandwidth (bw) of 0.1% of the central wavelength or frequency. The following tables, taken from the Elettra research centre website (www.elettra.trieste.it), sums up the main operating parameters and features of the storage ring.

Elettra storage ring parameters.

Beam energy [GeV]			2	2.4
Storage ring circumference [m]		259.2		
Beam height in experimental area [m]		1.3		
Number of achromats		12		
Length of Insertion Device (ID) straight sections [m]		6(4.8 utilizabile per ID's)		
Number of straight sections of use for ID's		11		
Number of bending magnet source points		12		
Beam revolution frequency [MHz]		1.157		
Number of circulating electron bunches	1 - 432			
Time between bunches [ns]	864 - 2			
Tunes: horizontal/vertical	14.3/8.2			
Natural emittance [nm-rad]		7	9.7	
Energy lost per turn without ID's [keV]		255.7	533	
Maximum energy lost per turn with ID's [keV] (all)		315	618.5	
Critical energy [keV]		3.2	5.5	
Bending magnet field [T]		1.2	1.45	
Geometrical emittance coupling %	£ 1%			
Spurious dispersion (at the centre of IDs): horizontal (rms max/min) [cm]	6/2.			
Spurious dispersion (at the centre of IDs): vertical (rms max/min) [cm]	2/0.5			
Injected current [mA]		320	150	
Machine dominated by the Touschek effect				
Energy spread (rms) %		0.08	0.12	
Lifetime [h] (natural) **Lifetime [h] (with 3rd harmonic cavity)**		8.5 27	32 32	
Bunch length (1 σ) [mm]		5.4	7	
Beam dimensions (1 σ)				
ID source point - horizontal/vertical [μm]		241/15	283/16	
Bending magnet source point - horizontal/vertical [μm]		139/28	197/30	
Beam divergence (1 σ)				
ID source point - horizontal/vertical [μrad]		29/6.	35/8.	
Bending magnet source point - horizontal/vertical [μrad]		263/9	370/13	

SuperESCA beamline

SuperESCA is the first beamline operating at the Elettra synchrotron facility since 1994. It exploits the full capabilities of high resolution core-level photoemission spectroscopy (HR-XPS) by combining high resolution feature with the high flux of linearly polarised photons in the 90 to 1500 eV energy range. Thus, it allows in depth investigations on the electronic and structural properties of a variety of samples that ranges between single crystals, thin films as well as new nanostructured materials. For these intents, the light produced by the insertion device at the storage ring is collected, monochromatized and brought to the experimental station following a prefoucusing-monochromator-refocusing scheme. The radiation coming from the insertion device is pre-focused into the monochromator entrance slit by a vertically oriented cylindrical mirror. The dispersed light coming out from the monochromator exit slit is finally refocused by an ellipsoidal mirror on the sample in the experimental chamber.

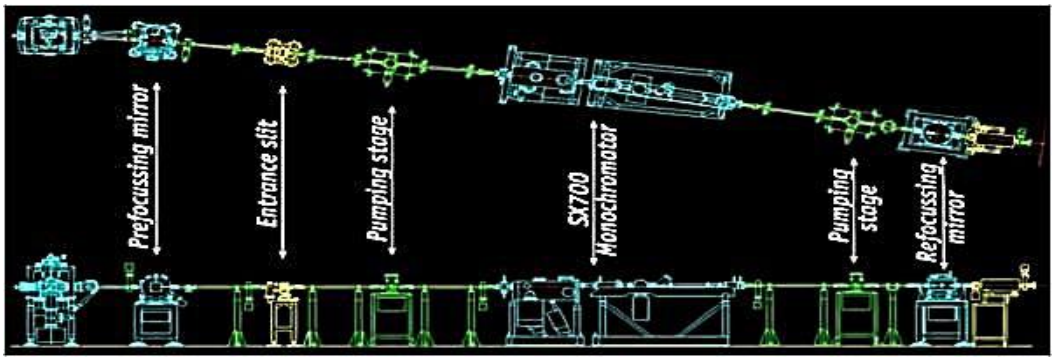

Layout of the superESCA beamline showing the focusing mirrors, the entrance slit and monochromator.

By modulating the gap between the two magnets of the insertion device the photon energy can be varied in the range 90-1500 or 130-1800 eV when the Elettra storage ring works at 2.0 or 2.4 GeV, respectively. The insertion device is characterized by a maximum brilliance of 4.36×10^{18} photons/s/mm^2/mrad^2/0.1%bw/100 mA. The monochromator is of the SX700 type, and consists of a 1200 l/mm plane grating. The tables below report the main features of the beamline insertion device and monochromator

Parameters of the SuperESCA insertion device.

source:	Linear Planar Undulator (LPU) from Kyma s.r.l. divided in 2 sections
period:	46 mm
number of periods:	98
polarisation:	linear horizontal
minimum gap:	13.5 mm
energy range:	90 - 1800 eV
peak brilliance:	~ 4 x 10^{18} ph/s/100 mA/0.1% BW/mm2/mrad^2 [1)]

Parameters of the SuperESCA monochromator.

optics:	Fix focus PGM (SX700) with plane mirror, plane grating and focusing ellipsoidal mirror
groove density:	1200 lines/mm
energy range:	85 - 1800 eV
exit slit dimension:	5 - 100 μm
energy resolution (E/ΔE) :	~ 10^4 @ 400 eV; ~ 5 x 10^3 @ 900 eV
beam size:	100 x (exit slit dimension) μm^2
photon flux:	~ 10^{12} photon/s @ 400 eV [1)]

The SuperESCA experimental station consists of two Ultra High Vacuum (UHV) chambers (base pressure 8×10^{-11} mbar) separated by a gate valve: a sample preparation chamber, and the main chamber, where the sample is allocated during spectra acquisition. The main chamber is equipped with a 150 mm hemispherical electron energy analyser with variable entrance slit. After loading of the sample in the main chamber and prior to analysis, alignment with the X-ray beam and analyser is accomplished by means of a sample manipulator. The manipulator is a liquid He cryostat with xyz translations and one rotational axes (θ). All the manipulator movements are manually controlled. When in the main chamber, the sample can be heated by electron bombardment and, using a PID system, its temperature can be stabilized in the range between 15 and 1500 K.

C 1s and O 1s core-level XPS spectra, curve fitting results

South African Char C 1s core-level

		C sp^2		*C sp^3, C-C(O)*		*C vacancy*	
Sample	**%f**	**Intensity(a.u.)**	**BE(eV)**	**Intensity(a.u.)**	**BE(eV)**	**Intensity(a.u.)**	**BE(eV)**
573 K Air	0.5	2167.22	284.54	2508.19	284.98	52.87	283.94
723 K Air	24	3464.14	284.42	691.73	284.99	414.77	283.85
723 K Air	63	3022.02	284.35	689.24	284.91	505.36	283.75
773 K Air	67	3149.35	284.42	497.79	285.01	331.71	283.74
1073 K Air	13	3499.51	284.49	526.52	285.01	277.68	283.84

		C-O-C ether, C=O carbonyl		*C-O epoxy, C-OH hydroxyl*		*(H)O-C=O carboxyl, lactol*	
Sample	**%f**	**Intensity(a.u.)**	**BE(eV)**	**Intensity(a.u.)**	**BE(eV)**	**Intensity(a.u.)**	**BE(eV)**
573 K Air	0.5	552.16	285.46	319.06	286.26		
723 K Air	24	251.63	285.68	516.45	286.21	331.24	288.27
723 K Air	63	318.36	285.64	404.01	286.24	320.28	288.25
773 K Air	67	111.35	285.52	717.07	286.08	347.11	288.33
1073 K Air	13	365.58	285.36	454.26	286.23	197.81	288.42

			C sp^2	*C sp^3, C-C(O)*	*C vacancy*	*C-O-C ether C=O carbonyl*	*C-O epoxy, C-OH hydroxyl*	*(H)O-C=O carboxyl, lactol*
Sample	**Γ_L(eV)**	**α**	**Γ_G(eV)**	**Γ_G(eV)**	**Γ_G(eV)**	**Γ_G(eV)**	**Γ_G(eV)**	**Γ_G(eV)**
573 K Air	0.18	0.08	0.75	0.75	0.71	0.98	1.35	
723 K Air	0.18	0.08	0.74	0.75	0.72	0.98	1.36	1.98
723 K Air	0.18	0.08	0.75	0.75	0.71	0.99	1.35	1.98
773 K Air	0.18	0.08	0.75	0.75	0.71	0.99	1.35	1.96
1073 K Air	0.18	0.08	0.75	0.74	0.72	0.99	1.37	1.98

	C sp²		*C sp³, C-C(O)*		*C vacancy*	
Sample	**Intensity(a.u.)**	**BE(eV)**	**Intensity(a.u.)**	**BE(eV)**	**Intensity(a.u.)**	**BE(eV)**
1° Oxidation	2167.22	284.54	2508.19	284.98	52.87	283.94
1° Desorption	2588.19	284.49	1917.98	284.96	116.06	283.95
2° Oxidation	2683.13	284.47	1778.04	284.96	125.14	283.82
3° Oxidation	2716.21	284.46	1468.22	284.97	117.85	283.77
1° Desorption	2725.84	284.43	817.44	284.95	169.43	283.79

	C-O-C ether, C=O carbonyl		*C-O epoxy, C-OH hydroxyl*	
Sample	**Intensity(a.u.)**	**BE(eV)**	**Intensity(a.u.)**	**BE(eV)**
1° Oxidation	552.16	285.46	319.06	286.26
1° Desorption	554.96	285.45	196.97	286.25
2° Oxidation	469.05	285.41	215.41	286.23
3° Oxidation	420.04	285.42	200.37	286.25
1° Desorption	219.57	285.54	179.52	286.24

			C sp²	*C sp³, C-C(O)*	*C vacancy*	*C-O-C ether C=O carbonyl*	*C-O epoxy, C-OH hydroxyl*
Sample	**Γ_L(eV)**	**α**	**Γ_G(eV)**	**Γ_G(eV)**	**Γ_G(eV)**	**Γ_G(eV)**	**Γ_G(eV)**
1° Ox	0.18	0.08	0.75	0.75	0.71	0.98	1.35
1° Des	0.18	0.08	0.75	0.75	0.71	0.99	1.38
2° Ox	0.18	0.08	0.75	0.75	0.71	0.98	1.35
3° Ox	0.18	0.08	0.75	0.75	0.71	0.98	1.35
3° Des	0.18	0.08	0.75	0.75	0.71	0.98	1.35

South African Char *O 1s* core-level

		C-O-C ether, C-OH hydroxyl		*C-O epoxy*		*C=O carbonyl,carboxyl, lactol*	
Sample	**%f**	**Intensity(a.u.)**	**BE(eV)**	**Intensity(a.u.)**	**BE(eV)**	**Intensity(a.u.)**	**BE(eV)**
573 K Air	0.5	816.89	532.28	439.31	533.28	103.89	530.65
723 K Air	24	957.53	532.12	1362.45	533.44	989.33	530.99
723 K Air	63	1484.12	531.99	1519.87	533.45	903.08	530.97
773 K Air	67	1131.93	531.99	1494.34	533.45	997.49	530.99
1073 K Air	13	1240.44	532.29	863.45	533.51	575.57	530.95

				H_2O			
Sample	**%f**	**Intensity(a.u.)**	**BE(eV)**	**Intensity(a.u.)**	**BE(eV)**	**Intensity(a.u.)**	**BE(eV)**
573 K Air	0.5	102.52	534.98				
723 K Air	24	71.14	535.49	54.44	537.22		
723 K Air	63	95.39	535.55	32.29	537.15		
773 K Air	67	228.12	535.51	180.79	537.18	170.74	539.05
1073 K Air	13	102.54	534.98				

			ether hydroxyl	*epoxy,*	*carbonyl, carboxyl,lactol*		***H_2O***	
Sample	**Γ_L(eV)**	**α**	**Γ_G(eV)**	**Γ_G(eV)**	**Γ_G(eV)**	**Γ_G(eV)**	**Γ_G(eV)**	**Γ_G(eV)**
573 K Air	0.18	0.08	1.91	1.87	1.91	1.81		
723 K Air	0.18	0.08	1.95	1.60	1.89	1.99	1.89	
723 K Air	0.18	0.08	1.95	1.61	1.89	1.99	1.84	
773 K Air	0.18	0.08	1.95	1.61	1.89	1.99	1.88	2.01
1073 K Air	0.18	0.08	1.95	1.61	1.89	1.81		

	C-O-C ether, C-OH hydroxyl		*C-O epoxy*		*C=O carbonyl, carboxyl, lactol*		*H_2O*	
Sample	**Intensity(a.u.)**	**BE(eV)**	**Intensity(a.u.)**	**BE(eV)**	**Intensity(a.u.)**	**BE(eV)**	**Intensity(a.u.)**	**BE(eV)**
1° Oxidation	816.89	532.28	439.31	533.28	103.89	530.65		
1° Desorption	642.32	532.22	351.63	533.43	153.67	530.74		
2° Oxidation	766.33	532.24	447.86	533.43	144.7	530.76		
3° Oxidation	766.68	532.21	446.67	533.47	179.15	530.68	59.53	536.62
1° Desorption	633.73	532.23	421.86	533.49	148.92	530.73		

			ether hydroxyl	*epoxy,*	*carbonyl, carboxyl,lactol*	*H_2O*
Sample	**Γ_L(eV)**	**α**	**Γ_G(eV)**	**Γ_G(eV)**	**Γ_G(eV)**	**Γ_G(eV)**
1° Oxidation	0.18	0.08	1.91	1.87	1.93	
1° Desorption	0.18	0.08	1.91	1.81	1.98	
2° Oxidation	0.18	0.08	1.91	1.89	1.83	
3° Oxidation	0.18	0.08	1.91	1.87	1.89	1.61
1° Desorption	0.18	0.08	1.94	1.83	1.90	

Appendix II

Fluidized bed reactor

The test rig used for the experiments [82] is located at RWTH University in Aachen, Germany. The experimental activities have been carried out by the Group of Professor Kneer. The reactor system consists of three major components: a gas feeding system with mass flow controllers, the actual small-scale fluidized bed reactor and a Fourier transform infrared (FT-IR) spectrometer for product gas analysis. The reactor is designed to implement the concept of a well-stirred reactor approximating uniform distributions of the thermodynamic state variables as well as of reacting species. Small batches of the sample are supplied to the fluidized bed while simultaneously analyzing the pyrolysis products in the exhaust gas. The FBR, shown in Fig.I-1(a-b). consists of two coaxial ceramic pipes mounted in a stainless steel reactor head. The fluidizing gas is fed in through the reactor head and flows downwards through the annular gap between the two pipes to the bottom of the reactor.

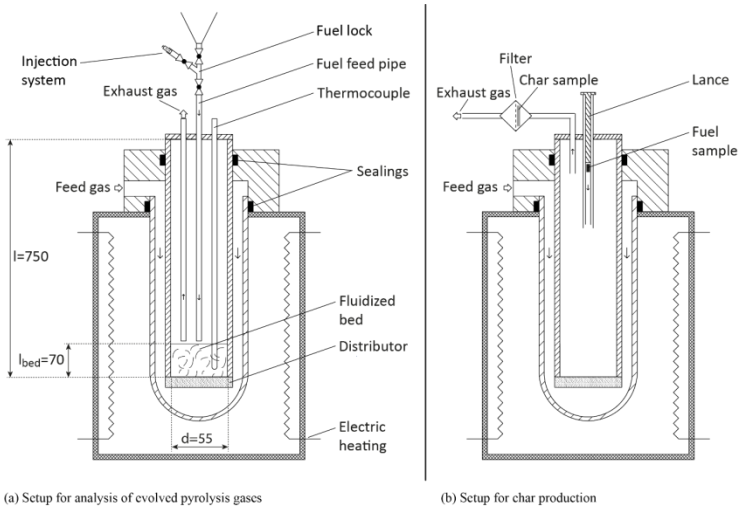

Fig.I-1(a-b). Experimental setups of the fluidized bed reactor.

The gas enters the inner reactor pipe (d_i = 55 mm) through a porous distributor plate made from sintered silica glass and fluidizes the bed. The distributor plate with a typical pore size between 40 and 100 µm creates a homogeneous inflow and is impermeable for the bed particles consisting of Al_2O_3, which are sieved to a mode of 115 µm ($d_{10/50/90}$ = 57/104/141 µm). The bed height is approx. 30 mm in non-fluidized state and increases to approx. 70 mm under typical flowing conditions. The feed gas flow for the present experiments is 0.833 l/min and consists of N_2 or CO_2. All ceramic parts of the reactor are located in an electrically heated furnace, which was operated at 1473 K. The bed

temperature is measured separately by a type S thermocouple placed in a ceramic shielding 50 mm above the distributor plate inside the fluidized bed. It does not deviate significantly from the oven temperature. On basis of all boundary conditions, the maximum particle heating rate is estimated to be in the range $1\text{-}2\cdot10^4$ K/s assuming a Chemical Percolation Devolatilization (CPD) model [201,202].

Small amounts of fuel within the range (15.0 ± 0.5) mg are introduced into the reactor via a lock and a vertical ceramic fuel feed pipe. To avoid particle sticking to the feed pipe walls and to enforce consistent conditions for each experiment, the pipe is flushed with 10 ml of feed gas taken from the reactor within 0.5 s during injection. The released product gases are captured just above the bed and flow through a sampling line and a filter into the gas cell of the FT-IR spectrometer. The whole sampling system is heated to 453 K to prevent water condensation. The utilized *GASMET DX-2000* FT-IR spectrometer has a maximum scan frequency of 0.56 Hz.

Pyrolysis gas yields are calculated in two steps. At first, a regression analysis is undertaken to evaluate the species concentration from each measured spectrum resulting in a concentration profile over time for each analyzed species. Afterwards the specific gas yields y_i of each species are calculated (eq. I.1):

$$y_i = \frac{\rho_{N2}}{m_{fuel}} \cdot \frac{M_i}{M_{N2}} \cdot \int_{t\,start}^{t\,end} \dot{V}_{N2}(t) \cdot c_i(t)\,dt \qquad \text{(I.1)}$$

where $c_i(t)$ is the volumetric concentration, V_{N2} is the feed gas volume flow (STP) and ρ_{N2} its density (STP), M_{N2} and M_i are the molar masses of nitrogen and the species, m_{fuel} is the delivered fuel mass, t_{start} and t_{end} are the start and end time of the experiment. The FT-IR spectrometer is calibrated for a large number of IR-active gas components like CO_2, CO, H_2O, different hydrocarbons (CH_4, C_2H_2, C_2H_4, C_3H_6 and higher) as well as nitrogen compounds and sulfur species. Non IR-active gases like H_2 or N_2 stay undetected.

For the production of char in amounts sufficient for further analyses, the experimental setup was slightly changed as it can be seen in Fig.I-1(b). The small ceramic pipes for fuel supply, exhaust gas and thermocouple shielding were removed and replaced by a fuel feed system for larger batches of particles. The construction consists of a metal pipe ending just below the reactor head and a lance inside this pipe. Deviating from the described setup before, the bed of aluminum oxide particles was removed to avoid mixing between the bed and char particles in the product. Reactor temperature was

solely adjusted by means of wall temperature. In the char production process, raw coal batches of approx. 0.2 g were introduced with the lance and then fluidized for about 10 s with a volume flow of 50 l/h. Afterwards the volume flow was increased to more than 600 l/h to switch from fluidized bed regime to pneumatic conveying and blow out the char particles. Char particles were separated from the gas flow with a filter system and cooled down to ambient temperature. Particle agglomerates larger than 180 µm were sieved out afterwards. Tar samples could not be collected, since the resulting amounts were too small. The char yield was calculated by the ash tracer method, according to eq.I2:

$$Char\ Yield_{dry} = \left(\frac{a_{coal}}{a_{sample}}\right)_{dry} \qquad \text{(I.2)}$$

where a_i determines the ash content of the dry coal and the pyrolyzed sample, respectively as measured by proximate analysis.

Drop tube reactor

The drop tube reactor used for the experiments [80-82,119,192] is located at Ruhr University in Bochum, Germany.The experimental activities have been carried out by the Group of Professor Scherer.The laminar drop tube reactor (Fig.I.2) is designed for short residence times (below 150 ms), comparable to devolatilization time scales of pf boilers. The test rig has five main parts: the coal particle feeder, the hot gas supply, the reactor tube, the sampling system and the gas analyzer.

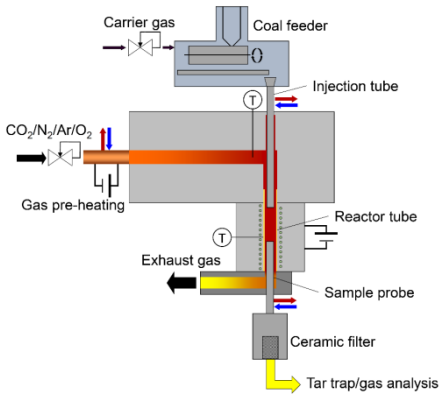

Fig.I-2. Schematics of the drop tube reactor.

The particle feeding system consists of a particle silo, a metering screw, a vibrating conveyor and a water-cooled injection tube. It is designed to transport the particles to the reaction zone without preterm exposure to heat or reaction atmosphere. A microwave-based plasma source is used to heat

the gases (N_2, CO_2) to a pre-selected temperature. The volume flow rate (process and feed gas flow) was set to 50 l/min by mass flow controllers in all experiments. Feed gas (2% of total flow) is either CO_2 or N_2 corresponding to the process gas.

The reactor tube is a 320 mm long electrically heated Al_2O_3 pipe (d_i = 50 mm). The wall temperature was set to 1573 K. Due to the thermal conditions, particles are heated up rapidly by radiation and convection with maximum heating rates in the order of 10^4-10^5 K/s. A movable cooled sampling probe can be positioned at different distances from the particle inlet. A heated ceramic filter (570 K) separates solids whereas tar condenses inside a heated glass tube (370 K). Gas concentrations are measured on-line by FT-IR spectroscopy (*ThermoFisher Antaris IGS USB*), calibrated for a large range of IR-active species.

Both, particle residence times and heating rates, were determined CFD-aided [81] and resulting residence times for N_2 were found to be 120 ms and 130 ms for CO_2, respectively: a time sufficient to complete pyrolysis but short compared to the timescale of heterogeneous char gasification. Maximum heating rates found were $2.9 \cdot 10^4$ K/s (N_2) and $3.5 \cdot 10^4$ K/s (CO_2). Final particle temperature was 1504 K (N_2), and 1557 K (CO_2), respectively.

Note that the probe cross section is smaller than the cross section of the reactor tube (350 vs. 1960 mm²). This also implies that not all of the particles fed by the injection tube will end up in the sampling probe and thus a mass balance cannot be given. The ash content measured was therefore used to calculate the char yield according to eq. I.2. The gas yield was determined by integration of the gas concentrations measured by FT-IR spectroscopy throughout the experiment. The tar yield could be estimated by difference.

Bibliography

[1] S. Potgieter-Vermaak, N. Maledi, N. Wagner, J.H.P. Van Heerden, R. Van Grieken, J.H. Potgieter. 'Raman spectroscopy for the analysis of coal: a review'. *Journal of Raman Spectroscopy* **42**, 123-129 (2011).

[2] C. Baird, M. Cann. *Environmental Chemistry 5th Edition*. W. H. Freeman (2012).

[3] G.B. Skripchenko. 'Methodology for Studying Molecular and Supramolecular Structures of Coals and Carbonaceous Materials'. *Solid Fuel Chemistry* **43**, 333–340 (2009).

[4] A. Marzec. 'Macromolecular and molecular model of coal structure'. *Fuel Processing Technology* **14**, 39–46 (1986).

[5] F.G. Emmerich. 'Evolution with heat treatment of crystallinity in carbons'. *Carbon* **33**, 1709–1715 (1995).

[6] O. Senneca, F. Scala, R. Chirone, P. Salatino. 'Relevance of structure, fragmentation and reactivity of coal to combustion and oxy-combustion'. *Fuel* **201**, 65-80 (2017).

[7] J.F. Stubington, T.M. Linjewile, *Fuel* **68**,155–160 (1989).

[8] E.K. Campbell, J.F. Davidson. *Institute of Fuel Symposium Series 1: Fluidized Bed Combustion*, 1975, A2.1-A2.9.

[9] O. Senneca, P. Salatino. 'Loss of gasification reactivity toward O_2 and CO_2 upon heat treatment of carbons'. *Proceedings of the Combustion Institute* **29**, 485–493 (2002).

[10] J.G. Bailey, A. Tate, F.K. Diessel, T.F. Wall. 'A char morphology system with applications to coal combustion'. *Fuel* **69** (2), 225-239 (1990).

[11] J.M. Ranish, P. L. Jr. Walker. *Carbon* **31**:135 (1993).

[12] R.H. Hurt, J.M. Calo. 'Semi-global intrinsic kinetics for char combustion modelling'. *Combust. Flame* **125**, 1138-1149 (2001).

[13] P. Salatino, O. Senneca, S. Masi. 'Gasification of a coal char by oxygen and carbon dioxide'. *Carbon* **36**, 443–452 (1998).

[14] Z. Du, A.F. Sarofim, J.P. Longwell. 'Kinetic Measurement and Modeling of Carbon Oxidation'. *Energy & Fuels* **5**, 214-221 (1991).

[15] H. Wang, B.Z. Dlugogorski, E.M. Kennedy. 'Analysis of the mechanism of the low-temperature oxidation of coal'. *Combustion and Flame* **134**, 107–117 (2003).

[16] S.W. Dack, M.D. Hobday, T. D. Smith, J.R. Pilbrow. 'Free radical involvement in the oxidation of Victorian brown coal'. *Fuel* **62**, 1510-1512 (1983).

[17] R.E. Jones, D.T.A. Townend. 'Mechanism of the oxidation of coal'. *Nature* **155**, 424-425 (1945).

[18] P.D. Swann, D.G. Evans. 'Low-temperature oxidation of brown coal. 3. Reaction with molecular oxygen at temperatures close to ambient'. *Fuel* **58**, 276-280 (1979).

[19] J.S. Gethner. 'Thermal and oxidation chemistry of coal at low temperatures'. *Fuel* **64**, 1443 (1985).

[20] C.A. Rhoads, J.T. Senftle, M.M. Coleman, A. Davis, P.C. Painter. 'Further studies of coal oxidation'. *Fuel* **62**, 1387-1392 (1983).

[21] D.L. Perry, A. Grint. 'Application of XPS to coal characterization'. *Fuel* **62**, 1024-1033 (1983).

[22] H. Wang, B.Z. Dlugogorski, E.M. Kennedy. 'Coal oxidation at low temperatures: oxygen consumption, oxidation products, reaction mechanism and kinetic modelling'. *Progress in Energy and Combustion Science* **29**, 487–513 (2003).

[23] Q. Zhuang, T. Kyotani, A. Tomita. 'Dynamics of Surface Oxygen Complexes during Carbon Gasification with Oxygen'. *Energy & Fuels* **9**, 630-634 (1995).

[24] A.E. Lear, T.C. Brown, B.S. Haynes. 'Formation of metastable oxide complexes during the oxidation of carbons at low temperatures'. *Twenty-Third Symposium (International) on Combustion/The Combustion Institute* **23**, 1191–1197 (1991).

[25] B.S. Haynes. 'A turnover model for carbon reactivity I. Development'. *Combustion and Flame* **126**,1421–1432 (2001).

[26] L.R. Radovic. 'Active Sites in Graphene and the Mechanism of CO_2 Formation in Carbon Oxidation'. *J. Am. Chem. Soc.* **131**, 17166–17175 (2009).

[27] R. Larciprete, S. Fabris, T. Sun, P. Lacovig, A. Baraldi, S. Lizzit. 'Dual Path Mechanism in the Thermal Reduction of Graphene Oxide'. *J. Am. Chem. Soc.* **133**, 17315–17321 (2011).

[28] R. Larciprete, P. Lacovig, S. Gardonio, A. Baraldi, S. Lizzit. 'Atomic Oxygen on Graphite: Chemical Characterization and Thermal Reduction'. *J. Phys. Chem.* **116**, 9900−9908 (2012).

[29] A. Bagri, C. Mattevi, M. Acik, Y.J. Chabal, M. Chhowalla, V.B. Shenoy. 'Structural evolution during the reduction of chemically derived graphene oxide'. *Nature Chemistry* **2**, 581–587 (2010).

[30] A. Sanchez, F. Mondragon. 'Role of the Epoxy Group in the Heterogeneous CO_2 Evolution in Carbon Oxidation Reactions'. *J. Phys. Chem. C.* **111** (2), 612–617 (2007).

[31] Z. Pan, R.T. Yang. 'Strongly bonded oxygen in graphite: detection by high-temperature TPD and characterization'. *Ind. Eng. Chem. Res.* **31**, 2675-2680 (1992).

[32] A. Incze, A. Pasturel, C. Chatillon. 'First-principles study of the atomic oxygen adsorption on the (0001) graphite surface and dissolution'. *Appl. Surf. Sci.* **177**(4), 226-229 (2001).

[33] A. Incze, A. Pasturel, P. Peyla. 'Mechanical properties of graphite oxides: Ab initio simulations and continuum theory'. *Phys. Re*V. *B.* **70**, 212103 (2004).

[34] N. Chen, R. Yang. 'Ab initio molecular orbital calculation on graphite: Selection of molecular system and model chemistry'. *Carbon* **36**, 1061-1070 (1998).

[35] S.G. Chen, R.T. Yang, F. Kapteijn, J.A. Moulijn. 'A new surface oxygen complex on carbon: toward a unified mechanism for carbon gasification reactions'. *Ind. Eng.Chem. Res.* **32**, 2835- 2840(1993).

[36] W. Cai et al. 'Synthesis and solid-state NMR structural characterization of ^{13}C-labeled graphite oxide'. *Science* **321**, 1815–1817 (2008).
[37] P.J. Hall, J.M. Calo. 'Secondary interactions upon thermal desorption of surface oxides from coal chars'. *Energy Fuels* **3**, 370-376 (1989).
[38] Q.L. Zhuang, T. Kyotani, A. Tomita. 'DRIFT and TK/TPD Analyses of Surface Oxygen Complexes Formed during Carbon Gasification'. *Energy Fuels* **8**, 714-718 (1994).
[39] Q. Zhuang, T. Kyotani, A. Tomita. 'Dynamics of Surface Oxygen Complexes during Carbon Gasification with Oxygen'. *Energy Fuels* **9**, 630-634 (1995).
[40] C. Wong, R.T. Yang, B.L. Halpern. *J. Chem. Phys* **78**, 3325- (1983).
[41] L.R. Radovic, H. Jiang, A. Lizzio. 'A transient kinetics study of char gasification in carbon dioxide and oxygen'. *Energy Fuels* **5**, 68-74 (1991).
[42] D. Mawhinney, J. Yates. 'FTIR study of the oxidation of amorphous carbon by ozone at 300 K Direct COOH formation'. *Carbon* **39**, 1167-1173 (2001).
[43] B.M. Lynch, L.I. Lancaster, J.A. MacPhee. 'Detection of carbonyl functionality of oxidized, vacuum-dried coals by photoacoustic infrared Fourier-transform (PAIFT) spectroscopy: correlations with added oxygen and with plastic properties'. *Energy Fuels* **2**, 13-17 (1988).
[44] S.R. Kelemen, H. Freund. 'XPS characterization of glassy-carbon surfaces oxidized by O_2, CO_2, and HNO_3'. *Energy Fuels* **2**, 111-118 (1988).
[45] H. He, T. Riedl, A. Lerf, J. Klinowski. 'Solid-State NMR Studies of the Structure of Graphite Oxide'. *J. Phys. Chem.* **100**, 19954-19958 (1996).
[46] S. Haydar, C. Moreno-Castilla, M. Ferro-Garcìa, F. Carrasco-Marìn, J. Rivera-Utrilla, A. Perrard, J. Joly. 'Regularities in the temperature-programmed desorption spectra of CO2 and CO from activated carbons'. *Carbon* **38**, 1297- 1308 (2000).
[47] P.E. Fanning, M.A. Vannice. 'A DRIFTS study of the formation of surface groups on carbon by oxidation'. *Carbon* **31**, 721-730 (1993).
[48] D. Gozzi, G. Guzzardi, A. Salleo. *Solid State Ionics* **83**,177 (1996).
[59] T. Grzybek, K. Kreiner. *Langmuir* **13**, 909 (1997).
[50] C. Hontoria-Lucas, A.J. Lopez-Peinado, J.d.D. Lopez-Gonzalez, M.L. Rojas-Cervantes, R.M. Martın-Aranda. 'Study of oxygen-containing groups in a series of graphite oxides: Physical and chemical characterization'. *Carbon* **33**, 1585-1592 (1995).
[51] B. Marchon, W.T. Tysoe, J. Carraza, H. Heinemann, G.A. Somorjai. 'Reactive and kinetic properties of carbon monoxide and carbon dioxide on a graphite surface'. *J. Phys. Chem.* **92**, 5744-5749 (1988).
[52] M. Mentaer, S. J. Ergun. *Bull. - US. Bur. Mines* 664 (1973).
[53] P. Salatino, O. Senneca. 'Preliminary Assessment of a Concept of Looping Combustion of Carbon'. *Ind. Eng. Chem. Res.* **48**, 102–109 (2009).
[54] A. Montoya, T. Truong, F. Mondragon, T.N. Truong. 'CO Desorption from Oxygen Species on Carbonaceous Surface: 1. Effects of the Local Structure of the Active Site and the Surface Coverage'. *J. Phys. Chem. A* **105** (27), 6757–6764 (2001).
[55] J.F. Espinal, A. Montoya, F. Mondragon, T.N. Truong. 'A DFT Study of Interaction of Carbon Monoxide with Carbonaceous Materials'. *J. Phys. Chem. B* **108** (3), 1003–1008 (2004).
[56] J.M. Beer. 'High efficiency electric power generation: The environmental role'. *Prog. Energy Combust. Sci.* **33**, 107-134 (2007).
[57] T.F. Wall. 'Combustion processes for carbon capture'. *Proc. Comb.Inst.* **31**, 31-37 (2007).
[58] L. Chen, S.Z. Yong, A.F. Ghoniem. 'Oxy-fuel combustion of pulverized coal: characterization, fundamentals, stabilization and CFD modeling'. *Prog. Energy Combust. Sci*. **38**, 156–214 (2012).
[59] M. Wang, A. Lawal, P. Stephenson, J. Sidders, C. Ramshaw. Post-combustion CO_2 capture with chemical absorption: a state-of-the-art review. *Chemical Engineering Research and Design* **89**, 1609-1624 (2011).
[60] J. Blamey, E.J. Anthony, J. Wang, PS. Fennell. 'The calcium looping cycle for largescale CO_2 capture'. *Progress in Energy and Combustion Science* **36**, 260-279 (2010).
[61] R. Thiruvenkatachari, S. Su, H. An, X.X. Yu. 'Post combustion CO_2 capture by carbon fibre monolithic adsorbents'. *Progress in Energy and Combustion Science* **35**,438-455 (2009).
[62] T.C. Merkel, H. Lin, X. Wei, R. Baker. 'Power plant post-combustion carbon dioxide capture: an opportunity for membranes'. *Journal of Membrane Science* **359**,126-139 (2010).
[63] A. Lyngfelt, B. Leckner, T. Mattisson. 'A fluidized-bed combustion process with inherent CO_2 separation: application of chemical-looping combustion'. *Chem. Eng. Sci.* **56**, 3101-1113 (2001).
[64] H. Jin, M. Ishida. 'A new type of coal gas fueled chemical-looping combustion'. *Fuel* **83**, 2411-2417 (2004).
[65] T.J. Thomas, L.S. Fan, P. Gupta, L.G. Velazquez Varga. 'Combustion Looping Using Composite Oxygen Carriers'. US Patent, US2005/0175533 A1, (2005).
[66] T. Mattisson, F. Garcia-Labiano, B. Kronberger, A. Lyngfelt, J. Adanez, H. Hofbauer. 'Chemical-looping combustion using syngas as fuel'. *Int. J. Greenhouse Gas Control* **1**, 158-169 (2007).
[67] E. Johansson, A. Lyngfelt, T. Mattisson, F. Johnsson. 'Gas leakage measurements in a cold model of an interconnected fluidized bed for chemical-looping combustion'. *Powder Technol*. **134**, 210-217 (2003).
[68] R.K. Lyon, J.A. Cole. 'Unmixed combustion: an alternative to fire'. *Combust. Flame* **121**, 249-261 (2000).
[69] J.S. Dennis, S.A. Scott, A.N. Hayhurst. 'In situ gasification of coal using steam with chemical looping: a technique for isolating CO_2 from burning a solid fuel'. *J. Energy Inst.* **79**, 187-190 (2006).
[70] H. Leion, T. Mattisson, A. Lyngfelt. 'The use of petroleum coke as fuel in chemical-looping combustion'. *Fuel* **86**, 1947-1958 (2007).

[71] J. Wang, E.J Anthony. 'Clean combustion of solid fuels'. *Appl. Energy* **85**, 73-79 (2008).
[72] P. Salatino, O. Senneca. Int. Patent application WO2010/026259A2 (2010).
[73] B.P. Spigarelli, S.K. Kawatra. 'Opportunities and challenges in carbon dioxide capture'. *Journal of CO_2 Utilization* **1**, 69-87 (2013).
[74] F.L. Horn, M. Steinberg. 'Control of carbon dioxide emissions from a power plant (and use in enhanced oil recovery)'. *Fuel* **61**, 415-422 (1982).
[75] M. Steinberg. 'History of CO_2 greenhouse gas mitigation technologies'. *Energy Conversion and Management* **33**, 311-315 (1992).
[76] B. Abraham, J. Asbury, E. Lynch, A. Teotia. 'Coal-oxygen process provides carbon dioxide for enhanced recovery'. *Oil Gas Journal* **80**, 68-70 (1982).
[77] A.R. Abele, G.S. Kindt, W.D. Clark, R. Payne, S.L. Chen. 'An experimental program to test the feasibility of obtaining normal performance from combustors using oxygen and recycled gas instead of air'. Argonne National Lab Report ANL/ CNSV-TM-204; (1988).
[78] C.S. Wang, G.F Berry, K.C. Chang, A.M. Wolsky. 'Combustion of pulverized coal using waste carbon dioxide and oxygen'. *Combustion and Flame* **72**, 301-310 (1988).
[79] R. Payne, S.L. Chen, A.M. Wolsky, W.F. Richter. 'CO_2 recovery via coal combustion in mixtures of oxygen and recycled flue gas'. *Combustion Science and Technology* **67**,1-16 (1989).
[80] S. Heuer, O. Senneca, A. Wütscher, H. Düdder, M. Schiemann, M. Muhler, et al. 'Effects of oxy-fuel conditions on the products of pyrolysis in a drop tube reactor'. *Fuel Process. Technol.* **150**,41–49 (2016).
[81] S. Heuer, M. Schiemann, V. Scherer. 'Determination of devolatilization kinetics ininert and CO_2-enriched atmospheres in a plug flow reactor'. *32nd Pittsburgh Coal Conf., Pittsburgh, PA*, (2015).
[82] S. Pielsticker, S. Heuer, O. Senneca, F. Cerciello, P. Salatino, L. Cortese, B. Gövert, O. Hatzfeld, M. Schiemann, V. Scherer, R. Kneer. 'Comparison of pyrolysis test rigs for oxy-fuel conditions'. *Fuel Processing Technology* **156**,461-472 (2017).
[83] J. Nagle, R.F. Strickland-Constable, Proc. of Fifth Conf. Carbon: Macmillan (1962).
[84] Van Heek K.H., Mühlen H.J., in Fundamental Issues in Control of Carbon Gasification Reactivity, (Edited by J. Lahaye and P. Ehrburger), Kluwer Academic, Dordrecht (1991).
[85] P. Salatino, O. Senneca, L. Tognotti. La Chimica e l'Industria (1999).
[86] O. Senneca, P. Salatino, S. Masi. Proc. Comb. Inst. (2004).
[87] M.B. Toftegaard, J. Brix, P.A. Jensen, P. Glarborg, A.D. Jensen. 'Oxy-fuel combustion ofsolid fuels'. *Prog. Energy Combust. Sci.* **36**, 581–625 (2010).
[88] T. Wall, Y. Liu, C. Spero, L. Elliott, S. Khare, R. Rathnam, et al. 'An overview on oxy fuel coal combustion-state of the art research and technology development'. *Chem. Eng.Res. Des.* **87**, 1003–1016 (2009).
[89] B.J.P. Buhre, L.K. Elliott, C.D. Sheng, R.P. Gupta, T.F. Wall. 'Oxy-fuel combustion technology for coal-fired power generation'. *Prog. Energy Combust. Sci.* **31**, 283–307 (2005).
[90] C. Yin, J. Yan. 'Oxy-fuel combustion of pulverized fuels: combustion fundamentals and modeling'. *Appl. Energy* **162**,742–762 (2016).
[91] R. Stanger, T. Wall, R. Spörl, M. Paneru, S. Grathwohl, M. Weidmann, et al. 'Oxyfuel combustion for CO_2 capture in power plants'. *Int. J. Greenhouse Gas Control*. **40**,55–125 (2015).
[92] M. Schiemann, V. Scherer, S. Wirtz. 'Optical coal particle temperature measurement under oxy-fuel conditions: measurement methodology and initial results'. *Chem. Eng. Technol*. **32**, 2000–2004 (2009).
[93] C. Wang, X. Zhang, Y. Liu, D. Che. 'Pyrolysis and combustion characteristics of coals in oxyfuel combustion'. *Appl. Energy* **97**, 264–273 (2012).
[94] P.R. Solomon, M.A. Serio, E.M. Suuberg. 'Coal pyrolysis: experiments, kinetic rates and mechanisms'. *Prog. Energy Combust. Sci.* **18**, 133–220 (1992).
[95] R.C. Borah, P. Ghosh, P.G. Rao. 'A review on devolatilization of coal in fluidized bed'. *Int. J. Energy Res.* **35**, 929–963 (2011).
[96] J. Yu, J. Lucas, T. Wall. 'Formation of the structure of chars during devolatilization of pulverized coal and its thermoproperties: a review'. *Prog. Energy Combust. Sci.* **33**,135–170 (2011).
[97] J. Chen, X. Fan, B. Jiang, L. Mu, P. Yao, H. Yin, et al. 'Pyrolysis of oil-plant wastes in a TGA and a fixed-bed reactor: thermochemical behaviors, kinetics, and products characterization'. *Bioresour. Technol.* **192**, 592–602 (2015).
[98] T. Aysu. 'Catalytic pyrolysis of Alcea pallida stems in a fixed-bed reactor for production of liquid bio-fuels'. *Bioresour. Technol.* **191**, 253–262 (2011).
[99] T. Aysu, M. M. Küçük. 'Biomass pyrolysis in a fixed-bed reactor: effects of pyrolysis parameters on product yields and characterization of products'. *Energy* **64**, 1002–1025 (2014).
[100] X. Wang, Z. Hu, S. Deng, Y. Wang, H. Tan. 'Kinetics investigation on the combustion of biochar in O_2/CO_2 atmosphere'. *Environ. Prog. Sustain. Energy* **34**, 923–932 (2015).
[101] J. Gibbins-Matham, R. Kandiyoti. 'Coal pyrolysis yields from fast and slow heating in a wire-mesh apparatus with a gas sweep'. *Energy Fuel* **2**, 505–511 (1988).
[102] A.R.F. Drummond, I.W. Drummond. 'Pyrolysis of sugar cane bagasse in a wire-mesh reactor'. *Ind. Eng. Chem. Res.* **35**,1263–1268 (1996).
[103] E.M. Suuberg, W.a. Peters, J.B. Howard. 'Product composition and kinetics of lignite pyrolysis'. *Ind. Eng. Chem. Process. Des. Dev.* **17**, 37–46 (1978).
[104] E. Hoekstra, W.P.M. Van Swaaij, S.R.A. Kersten, K.J.A. Hogendoorn. 'Fast pyrolysis in a novel wire-mesh reactor: decomposition of pine wood and model compounds'. *Chem. Eng. J.* **187**,172–184 (2012).

[105] J. Yu, C. Yao, X. Zeng, S. Geng, L. Dong, Y. Wang, et al. 'Biomass pyrolysis in a microfluidized bed reactor: characterization and kinetics'. *Chem. Eng. J.* **168**,839–847 (2011).
[106] B. Gövert, S. Pielsticker, N. Vorobiev, S. Heuer, O. Hatzfeld, R. Kneer, et al. 'Examination of pyrolysis and char burnout in oxyfuel atmosphere using plug flow and well stirred reactor'. *18th IFRF Members Conf. Flex. Clean Fuel Convers. Ind*., (2015).
[107] R. Lemaire, C. Bruhier, D. Menage, E. Therssen, P. Seers. 'Study of the high heating rate devolatilization of a pulverized bituminous coal under oxygen-containing atmospheres'. J. *Anal. Appl. Pyrolysis* **114**, 22–31 (2015).
[108] M. Schiemann, S. Haarmann, S. Wirtz, V. Scherer, M. Ehmann, C. Kuhr. 'Combustion characterisation of fuels for power plants: from laboratory experiments to boiler furnace simulation'. *VGB PowerTech* **3**, 33–40 (2016).
[109] A.H. Tchapda, S.V. Pisupati. 'Characterization of an entrained flow reactor for pyrolysis of coal and biomass at higher temperatures'. *Fuel* **156**, 254–266 (2016).
[110] E. Aylón, A. Fernández-Colino, M.V. Navarro, R. Murillor, T. García, A.M. Mastral. 'Waste tire pyrolysis: comparison between fixed bed reactor and moving bed reactor'. *Ind. Eng. Chem. Res.* **47**, 4029–4033 (2008).
[111] A.G. Collot, Y. Zhuo, D. Dugwell, R. Kandiyoti. 'Co-pyrolysis and co-gasification of coal and biomass in bench-scale fixed-bed and fluidised bed reactors'. Fuel **78**, 667–679, (1999).
[112] A. Trubetskaya, P.A. Jensen, A.D. Jensen, A.D. Garcia Llamas, K. Umeki, P. Glarborg. 'Effect of fast pyrolysis conditions on biomass solid residues at high temperatures'. *Fuel Process. Technol*. **143,** 118–129 (2016).
[113] M. Guerrero, M.P. Ruiz, M.U. Alzueta, R. Bilbao, A. Millera. 'Pyrolysis of eucalyptus at different heating rates: studies of char characterization and oxidative reactivity'. *J. Anal. Appl. Pyrolysis* **74**, 307–314 (2005).
[114] P. Wang. 'Thermal behavior of coal and biomass blends in inert and oxidizing gaseous environments'. *Int. J. Clean Coal Energy* **1**, 35–42 (2015).
[115] S. Su, Y. Song, Y. Wang, T. Li, S. Hu, J. Xiang, et al. 'Effects of CO_2 and heating rate on the characteristics of chars prepared in CO_2 and N_2 atmospheres'. *Fuel* **142**, 243–249 (2015).
[116] C. Bu, B. Leckner, X. Chen, D. Pallarès, D. Liu, A. Gómez-Barea, 'Devolatilization of a single fuel particle in a fluidized bed under oxy-combustion conditions. Part A: experimental results'. *Combust. Flame* **162**,797–808, (2015).
[117] M.V. Gil, J. Riaza, L. Álvarez, C. Pevida, F. Rubiera. 'Biomass devolatilization at high temperature under N_2 and CO_2: char morphology and reactivity'. *Energy* **91**,655–662, (2015).
[118] R.K. Rathnam, L.K. Elliott, T.F. Wall, Y. Liu, B. Moghtaderi. 'Differences in reactivity of pulverised coal in air (O_2/N_2) and oxy-fuel (O_2/CO_2) conditions'. *Fuel Process.Technol*. **90**,797–802 (2009).
[119] O. Senneca, S. Heuer, M. Schiemann, V. Scherer, C. Russo, A. Ciajolo, et al. 'Effects of CO_2 on submicronic carbon particulateformed in the early stages of oxy-combustion'. *Combust. Flame* **172**, 302-308 (2016).
[120] A.G. Borrego, D. Alvarez. 'Comparison of Chars Obtained under Oxy-Fuel and Conventional Pulverized Coal Combustion Atmospheres'. *Energy & Fuels* 21, 3171-3179 (2007).
[121] L. Zhang, S. Kajitani, S. Umemoto, S. Wang, D. Quyn, Y. Song. 'Changes in nascent char structure during the gasification of low-rank coals in CO_2'. *Fuel* **158**, 711–718 (2015).
[122] S. Su, Y. Song, Y. Wang, T. Li, S. Hu, J. Xiang, C.Z. Li. 'Effects of CO_2 and heating rate on the characteristics of chars prepared in CO_2 and N_2 atmospheres'. *Fuel* **142**, 243–249 (2015).
[123] P.A. Bejarano, Y.A. Levendis. 'Single-coal-particle combustion in O_2/N_2 and O_2/CO_2 environments'. *Combust. Flame* **153**, 270–287 (2008).
[124] J.J Saastamoinen, M.J. Aho, J.P. Hämäläinen, R. Hernberg, T. Joutsenoja. 'Pressurized Pulverized Fuel Combustion in Different Concentrations of Oxygen and Carbon Dioxide'. *Energy & Fuels* **10**, 121–133 (1996).
[125] F. Scala, R. Chirone. 'Combustion of Single Coal Char Particles under Fluidized Bed Oxyfiring Conditions'. *Ind. Eng. Chem. Res*. **49**,11029–11036(2010).
[126] O. Senneca, L. Cortese. 'Kinetics of coal oxy-combustion by means of different experimental techniques'. *Fuel* **102**, 751-759 (2012).
[127] Q. Li, C. Zhao, X. Chen, W. Wu, Y. Li. 'Comparison of pulverized coal combustion in air and in O_2/CO_2 mixtures by thermo-gravimetric analysis'. *J. Anal. Appl. Pyrolysis.* **85**, 521–528 (2009).
[128] H. Xin, C. Wang, E. Louw, D. Wang, J.P. Mathews. 'Atomistic simulation of coal char isothermal oxy-fuel combustion: Char reactivity and behavior'. *Fuel* **182**, 935-943 (2016).
[129] H. Hertz. 'Ueber den Einfluss des ultravioletten Lichtes auf die electrische Entladung'. Annalen der Physik **31** (1887).
[130] A. Einstein.Concerning a Heuristic Point of View Toward the Emission and Transformation of Ligh'. Annalen der Physik 17 (1905).
[131] Juan A Colón Santana 'Quantitative Core Level Photoelectron Spectroscopy'. Morgan & Claypool Publishers 2015.
[132] R.L. Vander Wal, V. M. Bryg, M.D. Hays. 'XPS Analysis of Combustion Aerosols for Chemical Composition, Surface Chemistry, and Carbon Chemical State'. *Anal. Chem.* **83**, 1924-1930 (2011).
[133] F. Atamny, J. Blöcker, A. Dübotzky, H. Kurt, O. Timpe, G. Loose, W. Mahdi, R. Schlögl. 'Surface chemistry of carbon: activation of molecular oxygen'. *Molecular Physics* **76**, 851-886 (1992).
[134] R. Schlögl, H.P. Boehm. 'Influence of crystalline perfection and surface species on the X-ray photoelectron spectra of natural and synthetic graphites'. *Carbon* **21**, 345–358 (1983).
[135] A. Barinov, O.B. Malcioglu, S. Fabris, T. Sun, L. Gregoratti, M. Dalmiglio, M. Kiskinova. 'Initial Stages of Oxidation on Graphitic Surfaces: Photoemission Study and Density Functional Theory Calculations'. *J. Phys. Chem.* **113**, 9009-9013 (2009).
[136] T. Szabó, O. Berkesi, P. Forgó, K. Josepovits, Y. Sanakis, D. Petridis, I. Dékány. 'Evolution of Surface Functional Groups in a Series of Progressively Oxidized Graphite Oxides'. *Chem. Mater.* **18**, 2740-2749 (2006).

[137] W. Xia, J. Yang, C. Liang. 'Investigation of changes in surface properties of bituminous coal during natural weathering processes by XPS and SEM'. *Applied Surface Science* **293**, 293–298 (2014).
[138] B. Gonga, P.J. Pigramb, R.N. Lamba. 'Surface studies of low-temperature oxidation of bituminous coal vitrain bands using XPS and SIMS'. *Fuel* **77**, 1081-1087 (1998).
[139] T. Grzybek, R. Pietrzak, H. Wachowska. 'X-ray photoelectron spectroscopy study of oxidized coals with different sulphur content'. *Fuel Processing Technology* **1**, 77 – 78 (2002).
[140] J. Díaz, G. Paolicelli, S. Ferrer, F. Comin. 'Separation of the sp^3 and sp^2 components in the C1s photoemission spectra of amorphous carbon films'. *Physical Review* **54**, 8064 (1996).
[141] Y. Yamada, H. Yasuda, K. Murota, M. Nakamura, T. Sodesawa, S. Sato. 'Analysis of heat-treated graphite oxide by X-ray photoelectron spectroscopy'. *J. Mater. Sci.* **48**, 8171–8198 (2013).
[142] W. Zhang, V. Carravetta, Z. Li, Y. Luo, J. Yang. ''Oxidation States of Graphene: Insights from Computational Spectroscopy'. *Journal of Chemical Physics* **131**, 244505 (2009).
[143] S. Kim, S. Zhou, Y. Hu, M. Acik, Y. Chabal, C. Berger, W. de Heer, A. Bongiorno, E. Riedo. 'Room-temperature metastability of multilayer graphene oxide films'. *Nature Materials* **11**, 544 (2012).
[144] G. Levi, O. Senneca, M. Causà, P. Salatino, P. Lacovig, S. Lizzit. 'Probing the chemical nature of surface oxides during coal char oxidation by high-resolution XPS'. *Carbon* **90,** 181–196 (2015).
[145] G. Levi, M. Causà, P. Lacovig, P. Salatino, O. Senneca. 'Mechanism and thermochemistry of coal char oxidation and desorption of surface oxides'. *Energy Fuels* **31** (3), 2308–2316 (2017).
[146] A. Holme, K. J. Børve, L. J. Sæthre, T. D. Thomas. 'Accuracy of Calculated Chemical Shifts in Carbon 1s Ionization Energies from Single-Reference ab Initio Methods and Density Functional Theory'. *J. Chem. Theory Comput.* **7**, 4104–4114 (2011).
[147] M. Giesbers, A.T.M. Marcelis, H. Zuilhof. 'Simulation of XPS C1s Spectra of Organic Monolayers by Quantum Chemical Methods'. Langmuir **29**, 4782−4788 (2013).
[148] J.J. Joyce, M. Del Giudice, J.H. Weaver. 'Quantitative analysis of synchrotron radiation photoemission core level data'. *Journal of Electron Spectroscopy and Related Phenomena* **49**, 31-45 (1989).
[149] S. Doniach, M. Šunjić. 'Many-electron singularity in X-ray photoemission and X-ray line spectra from metals'. *Journal of Physics C: Solid State Physics* **3**, 285-291 (1970).
[150] D.W. Lynch, C.G. Olson. *Photoemission Studies of High-Temperature Superconductors*. Cambridge University Press (2005).
[151] T.T.P. Cheung. 'X-ray photoemission of polynuclear aromatic carbon'. *J. Appl. Phys.* **55**, 1388 (1984).
[152] T.T.P. Cheung. 'X-ray photoemission of carbon: Lineshape analysis and application to studies of coals'. *Journal of Applied Physics* **53**, 6857-6862 (1982)
[153] R. Haerle, E. Riedo, A. Pasquarello, A. Baldereschi. 'sp^2/sp^3 hybridization ratio in amorphous carbon from C 1s core-level shifts: X-ray photoelectron spectroscopy and first-principles calculation'. *Physical Review* **65**, (2001).
[154] M.V. Gil, D. Casal, C. Pevida, J.J. Pis, F. Rubiera. 'Thermal behaviour and kinetics of coal/biomass blends during co-combustion'. *Bioresource Technology* 101,5601-5608 (2010).
[155] S. Vyazovkin, C.A.Wight,'Model-free and model-fitting approaches to kinetic analysis of isothermal and non isothermal data' *Thermochimica Acta* **340**, 53-68 (1999).
[156] C. Branca, C. Di Blasi,'Global intrinsic kinetics of wood oxidation'. *Fuel* **83**, 81-87 (2004).
[157] J.J. Pis, G. de la Puente, E. Fuente, A. Morán, F. Rubiera. 'A study of the self-heating of fresh and oxidized coals by differential thermal analysis' *Thermochim. Acta* 279, 93-101(1996).
[158] F. Rubiera, A. Morán, O. Martínez, E. Fuente, J.J. Pis.'Influence of biological desulphurisation on coal combustion performance'. *Fuel Process. Technol*., **52** ,165-173 (1997).
[159] F. Rubiera, A. Arenillas, E. Fuente, N. Miles, J.J. Pis. 'Effect of the grinding behaviour of coal blends on coal utilisation for combustion'. *Powder Technol*., **105**, 351-356 (1999).
[160] F. Rubiera, A. Arenillas, B. Arias, J.J. Pis. 'Modification of combustion behaviour and NO emissions by coal blending'. *Fuel Process. Technol*., **77–78**, 111-117 (2002).
[161] C. Branca, A. Iannace, C. Di Blasi. 'Devolatilization and Combustion Kinetics of Quercus cerris Bark'. *Energy & Fuels* **21**,1078–84 (2007).
[162] S. Vyazovkin. What is meant by the term 'variable activation energy' when applied in the kinetics analyses of solid state decompositions (crystolysis reactions)?", *Thermochimica Acta*. **397**,269-271 (2003).
[163]S. Vyazovkin, C. A. Wight. 'Isothermal and non-isothermal kinetics of thermally stimulated reactions of solids' *International Reviews in Physical Chemistry* 17**,** 407-433 (1998).
[164] J.W. Cumming, J. McLaughlin 'The thermogravimetric behaviour of coal'.*Thermochimica Acta* **57**, 253-272 (1982).
[165] N.V. Russell, T.J. Beeley, C.-K. Man, J.R. Gibbins, J. Williamson. 'Development of TG measurements of intrinsic char combustion reactivity for industrial and research purposes'.*Fuel Processing Technology* **57**, 113-130 (1998)
[166] I.M.K. Ismail, P.L. Walker. 'DSC and TGA measurements of O_2 interaction with coal chars'. *Fuel* **68** (11), 1456–1460 (1989).
[167] T.J. Frankcombe, S.K. Bhatia, S.C. Smith. 'Ab initio modelling of basal plane oxidation of graphenes and implications for modelling char combustion'. *Carbon* **40**, 2341–2349 (2002).
[168] K. Sendt, B.S. Haynes. 'Density functional study of the reaction of O_2 with a single site on the zigzag edge of graphene'. *Proc. Combust. Inst.* **33**(2), 1851–1858 (2011).
[169] O. Senneca, P. Salatino, L. Cortese. 'Assessment of the thermochemistry of oxygen chemisorption and surface oxide desorption during looping combustion of coal char'. *Proc. Comb. Inst.* **34**, 2787–2793 (2013).
[170] O. Senneca, P. Salatino, R. Sorrenti. 'Beneficiation of coal fly ashes by oxygen chemisorption'. *Experimental Thermal and Fluid Science* **43**, 76-81 (2012).

[171] Y. Gao, I. Kulaots, X. Chen, R. Aggarwal, A. Mehta, E.M. Suuberg, R.H. Hurt. 'Ozonation for the chemical modification of carbon surfaces in fly ash'. *Fuel* **80** (5), 765–768 (2001).
[172] L. Lua, V. Sahajwalla, C. Kong, D. Harris. 'Quantitative X-ray diffraction analysis and its application to various coals'. *Carbon* **39**, 1821–183 (2001).
[173] IEA Report.'Coal in the Energy Supply of India. International EnergyAgency'. Coal IndustryAdvisory Board. India (2002).
[174] CR. Ward. 'Analysis and significance of mineral matterin coal seams'. *International Journal of Coal Geology* **50**, 135-138 (2002).
[175] H. Takagi, K. Maruyama, N. Yoshizova, Y. Yamada, Y. Sato. 'XRD analysis of carbon stacking structure in coal during heat treatment'. *Fuel* 83 (2007).
[176] K.S. Binoy, R. K. Boruah, P. K. Gogoi. 'A X-ray diffraction analysis on graphene layers of Assam coal'. *J.Chem.Sci*. **121**, 103-106 (2009).
[177] S. Ergun, VH. Tiensuu. 'Interpretation of the intensities of X-rays scattered by coals'. *Fuel* **38**, 64–78 (1959).
[178] TF. Yen, JG. Erdman, SS. Pollack. 'Investigation of the structure of petroleum asphaltenes by X-ray diffraction'. *Anal Chem* **33**,1587–94 (1961).
[179] M. Cloke, A. Gilfillan, E. Lester. 'The characterization of coals and density separated coal fractions using FTIR and manual and automated petrographic analysis'. *Fuel* **76**, 1289-1296 (1997).
[180] A. Gilfillan, E. Lester, M. Cloke, C. Snape. 'The structure and reactivity of density separated coal fractions'. *Fuel* **78**, 1639-1644 (1999).
[181] B. Manoj, Ponni Narayanan. 'Study of Changes to the Organic Functional Groups of a High Volatile Bituminous Coal during Organic Acid Treatment Process by FTIR Spectroscopy'. *Journal of Minerals and Materials Characterization and Engineering* **1**, 39-43 (2013).
[182] A. C. Ferrari, D. M. Basko. 'Raman spectroscopy as a versatile tool for studying the properties of graphene'. *Nature Nanotechnology* **8**, 235-246 (2013).
[183] C. Castiglioni, C. Mapelli, F. Negri, G. Zerbi. 'Origin of the D line in the Raman spectrum of graphite: A study based on Raman frequencies and intensities of polycyclic aromatic hydrocarbon molecules'. *J Chem Phys* (2001).
[184] A. Sadezky, H. Muckenhuber, H. Grothe, R. Niessner, U. Pöschl. 'Raman microspectroscopy of soot and related carbonaceous materials: Spectral analysis and structural information'. *Carbon* **43**, 1731-1742 (2005).
[185] L. Jeffrey, Sobolik, K. Douglas Ludlow, L. Hessevick. 'Parametric sensitivity comparison of the BET and Dubinin-Radushkevich models for determining char surface area by CO_2 adsorption'. *Fuel* **71** ,1195-1202 (1992).
[186] S. Brunauer, P.H. Emmett, E. Teller, 'Adsorption of Gases in Multimolecular Layers', *J. Am. Chem. Soc.* **60**, 309–319 (1938).
[187] M. Mahnke, HJ. Mögel. 'Fractal analysis of physical adsorption on material surfaces'. *Colloid Surf A* **216**, 215–218 (2003).
[188] J. Garrido, A. Linares-Solano, JM. Martin-Martinez, M. Molina-Sabio, F. Rodriguez-Reinoso, R. Terregrosa. 'Use of N_2 vs. CO_2 in the characterization of activated carbons'. *Langmuir* **3**,76–81(1987).
[189] M.M. Dubinin, L.V. Radushkevich, 'The Equation of the Characteristic Curve of Activated Charcoal', *Proc. Acad. Sci. URSS*. **55**, 327–329 (1947) .
[190] D. A. Shirley. 'High-Resolution X-Ray Photoemission Spectrum of the Valence Bands of Gold'. *Physical Review* **5**, 4709 (1972).
[191] C. J. Cramer. *Essentials of Computational Chemistry*. John Wiley & Sons, Second Edition (2004).
[192] B. Apicella, O. Senneca, C. Russo, S. Heuer, L. Cortese, F. Cerciello, et al., 'Characterization of carbonaceous particulate (soot and char) produced from fast pyrolysis of coal in inert and CO_2 rich atmospheres', *Fuel*. 118-123 (2016).
[193] M.G. Kaganer, 'New method for determining the specific surface area of adsorbents and other finely divided substances', *Russ. J. Phys. Chem*. **33**, 352-356.
[194] S.K. Bhatia, D.D. Perlmutter, 'A random pore model for fluid-solid reactions: I. Isothermal, kinetic control', *AIChE J*. **26** , 379-386 (1980).
[195] O. Senneca,'Kinetics of pyrolysis, combustion and gasification of three biomass fuels'. *Fuel Process. Technol*. **88** 87–97 (2007).
[196] Y. Yuan, S. Li, G. Li, N. Wu, Q. Yao. The transition of heterogeneous-homogeneous ignitions of dispersed coal particle streams. Combust Flame 161, 2458-68 (2014).
[197] K.-J. Lee, S.-J. Kim, 'Theoretical Investigation of CO_2 Adsorption on Graphene', *Bull. Korean Chem. Soc*. **34** 3022–3026 (2013).
[198] S. Mrozowski, 'Electric Resistivity of Polycrystalline Graphite and Carbons', Phys. Rev. **77** 838–838 (1950).
[199] I.L. Spain, 'The electronic transport properties of graphite, carbons, and related materials', *Chem. Phys. Carbon* **16**, 119–129 (1981).
[200] F.Atamny, J. Blöcker, A. Dübotzky, H. Kurt, O. Timpe, G. Loose, W. Mahdi, R. Schlögl, 'Surface chemistry of carbon: activation of molecular oxygen', *Mol. Phys*. **76,** 851–886 (1992).
[201] D.M. Grant, R.J. Pugmire, T.H. Fletcher, A.R. Kerstein, 'Chemical model of coal devolatilization using percolation lattice statistics', Energy & Fuels. **3**, 175-186 (1989).
[202] C. Hasse, 'Models for Coal Kinetics', *Ref. Modul. Chem. Mol. Sci. Chem. Eng*. 1-18 (2015).